12-1996

Influence of Tip Clearance on the Flowfield in a Compressor Cascade with a Moving Endwall

Richard J. McMullan

AFIT/GAE/ENY/96D-5

THESIS

INFLUENCE OF TIP CLEARANCE ON THE FLOWFIELD IN A COMPRESSOR CASCADE WITH A MOVING ENDWALL

Richard J. McMullan
Captain, USAF

AFIT/GAE/ENY/96D-5

Disclaimer Statement

The views expressed in this thesis are those of the author and do not reflect the official policy or position of the US Air Force, Department of Defense, or the US Government.

AFIT/GAE/ENY/96D-5

INFLUENCE OF TIP CLEARANCE ON THE FLOWFIELD IN A COMPRESSOR CASCADE WITH A MOVING ENDWALL

THESIS

Presented to the Faculty of the Graduate School of Engineering

of the Air Force Institute of Technology

Air University

In Partial Fulfillment of the

Requirements for the Degree of

Master of Science in Aeronautical Engineering

Richard J. McMullan

Captain, USAF

December 1996

Acknowledgments

This thesis is the final product of a great deal of time, effort and energy. I would have never been able to finish this research thesis without the help and encouragement of many people. I would like to take this opportunity to thank several people.

I would like to thank Dr. Paul I. King for the guidance he provided in the completion of this project. His advice and insight on the details of experimental research helped me stay focused on the objectives of the study. I would also like to thank the members of my committee Dr. Rodney D. Bowersox and Dr. Philip S. Beran for the time and effort they gave to helping me write a concise report of my research.

The AFIT laboratory technicians Mr. Jay Anderson, Mr. Andrew Pitts, Mr. Charles McNeely, Mr. Daniel Rioux and Mr. Mark Deriso were very helpful. Their assistance in trouble-shooting all the problems associated with experimental work enabled the completion of this thesis on time.

I would also like to thank all my friends who provided me with encouragement and support through this difficult process. A special thanks is sent to Julie Spohrer, Allison Yu, Heather Hughes, Steve Ray, Franklin Swayne and Scott and Susan Barber for the extra special things you all did for me.

Finally, I thank God for the His faithfulness. He provided me with the necessary strength I needed to complete this thesis. Praise be to God.

Richard J. McMullan

Table of Contents

List of Figures

List of Tables

List of Symbols

Symbol	
AFIT	Air Force Institute of Technology
AR	blade aspect ratio
ASME	American Society of Mechanical Engineers
DF	diffusion factor
MS	Microsoft
NEAT	New England Affiliated Technologies
PSI	Pressure Systems Inc.
SSE	sum squared error
A	hot-wire/film calibration constant
B	hot-wire/film calibration constant
C	hot-wire/film calibration constant
C_x	axial velocity (m/s)
Nu	Nusselt number
P_{local}	local total pressure (Pa)
P_{t1}	inlet total pressure (Pa)
R	universal gas constant (J/kg K)
Re	Reynolds number
Re_c	Reynolds number based on chord
T	static temperature of fluid about hot-wire/film (K)

T_{amb}	ambient temperature (K)
T_r	Eckert reference temperature (K)
T_{static}	static temperature (K)
T_{total}	total temperature (K)
U	endwall rotor speed relative to blade tip (m/s)
V	fluid flow velocity (m/s)
V_1	air inlet velocity (m/s)
V_2	air outlet velocity (m/s)
V_{eff}	effective velocity (m/s)
V_{local}	local velocity (m/s)
a	point of maximum camber
b	temperature loading factor
c	blade chord (in or cm)
d_s	diameter of hot-wire/film sensor (in or cm)
h	blade span (in or cm)
i	incidence angle (degrees)
k	cooling ratio
$\dot{m}_{center}$	mass flow rate in the center region (kg/s)
$\dot{m}_{local}$	local mass flow rate (kg/s)
$\dot{m}_{root}$	mass flow rate in the root region (kg/s)
$\dot{m}_{tip}$	mass flow rate in the tip region (kg/s)

rpm	revolutions per minute
p_{static}	static pressure (Pa)
p/s	pressure surface
s	blade pitch (in or cm)
s/s	suction surface
t	blade tip clearance (in or cm)
u	axial component of velocity (m/s)
v	pitchwise component of velocity (m/s)
w	spanwise component of velocity (m/s)
x	axial coordinate
y	pitchwise coordinate
z	spanwise coordinate
ΔA	incremental area (m^2)
ΔP_{local}	difference between local total pressure and inlet total pressure (Pa)
Δy	incremental spanwise distance (in or cm)
Δz	incremental pitchwise distance (in or cm)
α	angle between the hot-wire/film sensor axis and fluid velocity (degrees)
α_1	air inlet angle (degrees)
α_1'	blade inlet angle (degrees)
α_2	air outlet angle (degrees)
α_2'	blade outlet angle (degrees)

ε	deflection angle (degrees)
ϕ	flow coefficient (C_x/U)
ζ	stagger angle (degrees)
δ	deviation angle (degrees), incremental change in ϖ
γ	ratio of specific heats
μ	viscosity ($N\ s/m^2$)
ρ	density (kg/m^3)
θ	blade camber angle (degrees)
$\bar{\varpi}$	mass averaged total pressure loss coefficient
$\bar{\varpi}_{center}$	mass averaged total pressure loss coefficient for the center region
$\bar{\varpi}_{local}$	mass averaged local total pressure loss coefficient
$\bar{\varpi}_{passage}$	mass averaged total pressure loss coefficient for the passage
$\bar{\varpi}_{region}$	mass averaged total pressure loss coefficient for a region
$\bar{\varpi}_{root}$	mass averaged total pressure loss coefficient for the root region
$\bar{\varpi}_{tip}$	mass averaged total pressure loss coefficient for the tip region

Abstract

The effects of changing the blade tip clearances on the velocity and pressure flowfields within a compressor cascade were investigated in this experimental thesis. All moving endwall flowfield measurements were taken at a constant flow coefficient of 0.5 and tip clearances of 0.5, 1.0 and 2.0 percent chord. Hot-wire/film probes were used to determine the three-dimensional velocity vector components in various transverse planes - one upstream of the leading edges of the blades, three within the blade cascade and one downstream of the trailing edges of the blades. The transverse velocity vector plots showed a scraping of the tip leakage vortex from the suction surface of one blade across the blade pitch to the pressure surface of the adjacent blade. A total pressure rake placed downstream of the trailing edges of the blades measured the pressure flowfield at the exit of the cascade. The mass-averaged values of total pressure loss coefficient decreased for reduced gaps. Finally, the tests performed on a crenulated blade geometry at a tip clearance of 0.01 chord showed a 15.5% reduction in the total pressure losses as compared to the straight blade geometry.

INFLUENCE OF TIP CLEARANCE ON THE FLOWFIELD IN A COMPRESSOR CASCADE WITH A MOVING ENDWALL

I. Introduction

Background

Methods to improve the performance of axial compressors within aircraft gas turbine engines is an important research field. The aerodynamic losses associated with the interaction between the annulus wall boundary layer and the tip leakage flow across the blade tip clearance cause reductions in aircraft performance and efficiency. In order to decrease the losses near the annulus wall, the structure of the flowfield in this region must first be investigated and characterized. Then, the research efforts can focus on blade and casing improvements to reduce the tip region losses of an axial compressor.

Linear compressor cascade wind tunnels have been important research tools in the reduction of aerodynamic losses. A recent modification (Peter, 1995) to a linear cascade to provide a moving endwall now gives the ability to test different blade designs and tip clearances between the blades and the annulus wall without dismantling a compressor rotor stage.

Summary of Previous Research

Both linear compressor cascades and rotating compressor rigs have been used to determine the flow characteristics found in the blade tip region of a compressor. The flow characteristics formed from the interaction between the linear cascade stationary endwall boundary layer and the tip leakage flow across the blade tip gap have been identified and investigated. Kang and Hirsch (1993a, 1993b), Storer (1989) and Kunz et al. (1993) have all performed studies in this blade gap region to determine the effect blade tip clearance has on the velocity and pressure flowfields throughout a blade passage. The problem with these studies is that the results do not account for the effects of relative endwall movement found within an axial compressor.

To model the effects of the rotation of the blades, several studies were conducted on rotating compressor rigs. The flowfield structure characterized by the scraping of the tip leakage vortex across the blade pitch to the pressure surface of a blade has been investigated by Pandya and Lakshminarayana (1983), Lakshminarayana et al. (1985), Hah (1986) and Stauter (1993). The results gathered from studies on these rotating compressor rigs provide information on the velocity vector flowfields and total pressure losses inside an axial compressor.

In order to study the effects of relative motion between the blades and the annulus wall of the rotating compressor rigs, Peter (1995) designed and implemented a moving endwall system modification to the Air Force Institute of Technology (AFIT) linear compressor cascade. Peter investigated the total pressure losses in the wake region of the cascade at various moving endwall rotor speeds and tip clearances. The flow coefficients

(axial flow velocity through the cascade divided by the outer surface velocity of the moving endwall) investigated ranged from 1.66 to 20. These large values of flow coefficient (ϕ) were chosen to model stator flow coefficients at the hub and the larger start-up and idle values in the rotor.

Peter (1995) determined that pressure losses associated with tip clearance and endwall motion were confined to the region near the blade tips. His results showed decreases in the mass averaged total pressure loss coefficient for decreases in tip clearance from 2.4% to 0.33% chord. The pressure loss coefficient also decreased as the flow coefficient was reduced.

Objectives

The objectives of this investigation were to determine the flow features within a linear compressor cascade with a moving endwall and investigate how changes in tip clearance and blade geometry affect the flow features. The flow features investigated in this experimental study were the tip leakage and secondary flow vortices in the region near the blade tips and moving endwall, the flow structure outside this blade tip region, the turning of the flow by the cascade and the pressure losses at the exit of the cascade. Tip clearances of 2.0%, 1.0% and 0.5% chord were used to determine how changes in gap size affect the presence and movement of the vortices within the blade passage and the magnitude of the pressure losses in the exit plane of the cascade. A straight trailing edge blade geometry and a crenulated trailing edge blade geometry were investigated. Earlier studies on crenulated blades by Spacy (1993) and Costello (1993) have shown evidence of

improvements in wake mixing and total pressure losses when compared to straight edged blades. This study will determine the validity of this result for a linear cascade with a moving endwall.

The flow coefficient investigated in this experimental study was 0.5 because normal operating design point flow coefficients for an axial compressor rotor are 0.3 to 0.7. The flowfield features determined for this flow coefficient of 0.5 will represent the characteristics of the flow through an axial compressor rotor during normal operating conditions. Although Peter (1995) showed that the total pressure losses decreased with decreases in flow coefficient, the total pressure losses for $\phi = 0.5$ are expected to be larger than those measured by Peter. In order to achieve this flow coefficient, the flow Reynolds number was decreased to 9.72×10^4. Horlock (1973) showed that Reynolds numbers less than 1×10^5 increase the total pressure losses.

Limitations

Normal operating Reynolds numbers for linear cascade flows are approximately 2.0×10^5. In order to achieve the flow coefficient of 0.5 used in this study, the Reynolds number for the flow based on chord was 9.72×10^4 which corresponds to an axial flow velocity of 38.3 m/s. This flow Reynolds number was limited by a wind tunnel inlet harmonic squeal at velocities between 39 m/s and 58 m/s, and the maximum operating range of 2500 rpm for the motor driving the moving endwall.

Details of the flow structure of the tip leakage vortex were not captured by the total pressure measurements. The tube spacing for the total pressure rake is 0.15 in

(0.381 cm), and this spacing limits only one measurement along the spanwise width of the tip leakage vortex. The total pressure losses associated with the vortices for each tip clearance showed the proper trend that losses decrease with decreases in gap size.

The hot-wire probe support diameter of 0.1 in (0.254 cm) limited the proximity of velocity measurements to 0.1 in from both the stationary and moving walls. The traverse control system mounted to the test section limits the proximity of the velocity measurements near the blade surfaces. Since the cascade blades are not instrumented with static pressure taps, the blade surface pressure distributions are not investigated. The effects of rotor curvature, considered minimal inside the main passage, are discussed in Chapter II.

A description of the flow structure associated with blade tip clearances and moving endwall effects are presented in Chapter II. The experimental apparatus used in this experimental study is explained in Chapter III, and the procedures used in calibration, data acquisition and data reduction processes for this thesis are presented in Chapter IV. Finally, discussions of the results found and the conclusions drawn are presented in Chapters V and VI, respectively.

II. Description of Flowfield

General Description of a Compressor Cascade

Compressor cascades are used to model the relative flowfield in axial flow compressors. A linear cascade is composed of identical blades arranged in a row. The blades are equally spaced along the blade row, and the trailing edges of the blades are aligned parallel to each other. The purpose of the blades is to change the pressure and direction of the inlet fluid flow.

The description of a linear cascade is usually specified by the geometry of the blades and the flow conditions through the blades (Cohen et al.,1987:188). Figure 2.1 shows the nomenclature used to define a linear cascade. The blade geometry is defined by the blade chord (c), the pitch (s), the blade thickness distribution, the blade stagger angle, the blade inlet angle (α_1') and the blade outlet angle (α_2'). Other geometric features of the blade are the blade span (h), the blade chamber angle (θ) and the blade aspect ratio (AR). The blade camber angle is defined as the difference between the inlet blade angle and the outlet blade angle. The aspect ratio is the blade span divided by the blade chord. Flow conditions in the cascade are defined by the air inlet velocity (V_1) and angle (α_1), the air outlet velocity (V_2) and angle (α_2), the deflection angle (ε), the incidence angle (i) and the deviation angle (δ). The deflection angle is the difference between the air inlet angle and the air outlet angle; the incidence angle is the difference between the air inlet angle and the blade inlet angle; and the deviation angle is the difference between the air outlet angle and the blade outlet angle.

Linear Cascade with Moving Endwall Flow Features

The flowfield in an axial compressor rotor near the blade tip region is complex and not well understood. Many researchers have experimentally investigated this three-dimensional viscous flow, which is dependent on the clearance between the blade tips and the annulus wall, and determined that large tip clearances are detrimental to both the efficiency and stability of axial flow compressors (Storer and Cumpsty, 1991:252; Inoue et al., 1985:3). Therefore, more research on the flow characteristics of this region is needed.

The flowfield in a linear compressor cascade with a moving endwall is illustrated in Figure 2.2. The flow characteristics shown in this figure are secondary flow vortices, a tip leakage flow vortex and a vortex formed near the stationary wall. These characteristics are the principal sources of aerodynamic losses.

In Figure 2.2, the near tip secondary flow vortices are caused by the flow of low energy fluid from the pressure surface of blade 5 towards the suction surface of blade 4 within the blade passage (Storer, 1989:250). Near the stationary root wall, the secondary flow vortices are located on the suction surfaces of the blades. These vortices cause separation of the flow along the suction surface and create large pressure losses in the blade passage near the suction surface of the blade (Lakshminarayana, 1985b:17). For small tip clearances and/or no endwall movement, a secondary vortex below the tip leakage vortex is formed. The addition of endwall motion causes the two vortices to be scraped across the blade pitch towards the pressure surface of blade 5 by the viscous forces in the moving endwall boundary layer. As discussed later, for large tip clearances the secondary vortex is weakened and virtually disappears. Secondary flow vortices near

the tip overturn the flow in a compressor cascade, opposite to that caused by the tip leakage vortex.

Tip leakage flow through the tip clearance between the blades and the moving endwall is a result of the pressure gradient between the pressure and suction surfaces of the blade in the tip region. The size of the clearance gap and the viscous effects of the moving endwall and blade boundary layers determine the amount of tip leakage flow (Lakshminarayana, 1985b:2). The roll-up of the tip leakage flow to form a tip leakage vortex occurs at the leading edge suction surface of the blade near the moving endwall. As the flow through the passage moves downstream, the spiral flow caused by the vortex moves away from the moving endwall up to the blade trailing edge and then remains at a constant radial location downstream of the trailing edge of the blades. This vortical flow is characterized by high total pressure loss, low static pressure, low axial velocity, underturning of the flow and strong rotation or vorticity (Kang and Hirsch, 1993a:439). In contrast to the secondary flow vortex, the tip leakage vortex reduces the separation along the suction surface of the blade and thus reduces the greater losses generally associated with the flow separation (Storer, 1989:250).

As the tip clearance is increased, the location of the core of the tip leakage vortex moves in the spanwise direction away from the moving endwall and in a pitchwise direction away from the suction surface (Storer and Cumpsty, 1991:258; Kang and Hirsch, 1993b:448). The increase in gap size also tends to increase the size and circulation of the tip clearance vortex and diminish the size and strength of the secondary flow vortex in the tip region. These changes in the characteristics of the flow decrease the losses caused by

secondary flow vortex but increase the losses associated with the tip clearance vortex structure.

In Figure 2.2, the scraping of the tip clearance vortex across the passage from the suction side of blade 4 to the pressure side of blade 5 and away from the moving endwall is caused by the relative motion between the blades and the moving endwall (Hah, 1986:20). The reasons for the development of this scraping vortex are the increased mass flow through the tip clearance from the movement of the rotor and the viscous dragging effect of the moving endwall boundary layer. The scraping vortex induces radial inward flow near the tip along the pressure surface of the blade (Lakshimarayana et al., 1985:5).

In Figure 2.2, the flow structure of the vortex on the pressure surface of blade 4 is caused by the interaction of the tip leakage vortex from the suction surface of blade 3 with two separate boundary layers in this region. The boundary layer from the stationary half wall above the rotor is dragged by the viscous forces of the rotor boundary layer towards the pressure surface of blade 4. The interaction of these boundary layers tends to increase the intensity and roll-up of this vortex.

Secondary Flow Characteristics

The blade boundary layer is caused by the no-slip condition on the flow over the blade surfaces. A thin boundary layer is created near the trailing edge on the pressure surface due to the presence of a favorable pressure gradient. However, the adverse pressure gradient on the suction surface creates a thicker boundary layer. Flow separation is possible on the suction surface of the blade due to the large adverse pressure gradients.

The size of the boundary layer is also dependent on the flow turbulence upstream of the blade.

The moving endwall boundary layer is created by the no-slip condition of the flow along the surface of the annulus wall. The thickness of the boundary layer is a function of the flow conditions of inlet Reynolds number and inlet turbulence intensity. The axial distance along the moving endwall also determines the boundary layer thickness. A thick boundary layer tends to block the tip clearance which reduces the tip clearance flow (Kunz et al., 1993:463). This blockage causes an increase in aerodynamic losses in the tip region.

According to Kang and Hirsch (1993a:438), two more vortices are present in the flowfield of an axial compressor cascade. From their flow visualization experiments, a weak horseshoe vortex in front of the blade leading edge was detected for small tip clearances. They also noticed a tip separation vortex in the blade gap from the separation of the flow on the end surface of the blade tip.

Experimental Methods for Studying Tip Clearance Effects

Linear axial compressor cascades and actual axial compressor rotor stages are used to investigate the flow characteristics of the tip region for a compressor. Linear cascade facilities are normally used to model the two-dimensional effects of the flowfield, and actual compressor rigs are used to model the more difficult three-dimensional effects. Another difference is in the flow direction for each experimental model. The flow direction for the cascade facility is uniform, but the flow direction for the compressor rig is

varying as the annulus wall is approached (Kang and Hirsch, 1993b:450). Although experimental cascade data is not an exact representation of the flowfield, moving endwall experimental methods have been applied to linear compressor cascade facilities to better represent the three-dimensional effects that occur in an actual axial compressor.

Axial compressor rigs can provide quantitative along with qualitative results on the flowfield effects due to tip clearance. However, a problem with rotating compressor rigs is the difficulty in providing the instrumentation needed to study the entire flowfield range within a rotating blade passage. In spite of this difficulty, the compressor rig at Pennsylvania State University has provided useful experimental data on the flowfield in the tip region for axial compressor flow coefficients near 0.5 (Pandya and Lakshminarayana, 1983:2).

The experimental methods for modeling a moving endwall for a compressor cascade facility have included the use of a moving belt and a large rotating aluminum disk. The major problem with the moving belt experiments was the inability to achieve flow coefficients near the range expected in axial compressors without the belt flopping (Herzig, 1954). The experimental method of using of a large rotating disk to represent the actual flowfield near the annulus wall of a compressor provided results that were consistent with those found in rotating compressor rigs (Peter, 1995:6-1). However, the flow coefficients investigated were not representative of normal operating coefficients found in an actual compressor rotor stage.

Total Pressure Loss Coefficient for Quantifying Experimental Data

As previously presented by Peter (1995:2-5 to 2-7), a common indicator of cascade performance is the mass averaged total pressure loss coefficient (ϖ). This loss coefficient can be calculated for local points at the exit of the cascade or entire blade passages. The local values of ϖ are defined as

$$\varpi_{local} = \frac{\Delta P_{local}}{\frac{1}{2} \cdot \rho \cdot V_1^2} \tag{1}$$

where the total pressure value in the numerator is found by taking the difference between the local total pressure (P_{local}) measured with the pressure rake and the inlet total pressure (P_{t1}) measured with a Pitot tube upstream of the blades.

$$\Delta P_{local} = P_{t1} - P_{local} \tag{2}$$

The local mass flow rate for each point is defined as

$$\dot{m}_{local} = \rho \cdot V_{local} \cdot \Delta A \tag{3}$$

where the incremental area associated with each local point is the product of the spanwise data spacing and the pitchwise data spacing, $\Delta A = \Delta z \Delta y$.

The density of the flow is calculated from the ideal gas law

$$\rho = \frac{p_{static}}{R \cdot T_{static}} \tag{4}$$

where the static pressure was measured from the average of the static pressure ports located along the tunnel wall in the wake region of the blades. The universal gas constant (R) has a value of 287 J/kg K for air. The static temperature is calculated from the isentropic relations for a known value of total temperature (T_{total}) by

$$T_{static} = T_{total} \cdot \left(\frac{p_{static}}{P_{local}} \right)^{\frac{\gamma - 1}{\gamma}} \tag{5}$$

where the ratio of specific heats (γ) is taken to be 1.4 for air.

The local velocity at each data point is determined from the definition of total temperature.

$$V_{local} = \sqrt{2 \cdot \frac{\gamma \cdot R}{\gamma - 1} (T_{total} - T_{static})} \tag{6}$$

Finally, the mass averaged total pressure loss coefficient for each blade passage is defined as

$$\varpi_{passage} = \frac{\sum_{j,k}\left(\varpi_{local} \cdot \dot{m}_{local}\right)}{\sum_{j,k}\dot{m}_{local}} \tag{7}$$

where j represents the number of steps in the y direction and k represents the number of steps in the z direction.

III. Experimental Apparatus

The experimental research for this thesis was conducted in the AFIT Cascade Wind Tunnel Facility located in Building 640, Room 143 at the Air Force Institute of Technology. The experimental apparatus of this facility consists of five major components. These components are the air supply system, the diffuser/stilling chamber, the cascade test section, the moving endwall rotor and the data acquisition system. A description of each component is provided below.

Air Supply System and Diffuser/Stilling Chamber

Figure 3.1 shows a schematic of the air supply system and diffuser/stilling chamber for the cascade facility. The air supply system for the research facility consists of a 30 kW centrifugal blower, induced laboratory air flow through the inlet to the blower and high pressure supplemental air feed which together provide a mass flow rate of approximately 1.6 kg/s. For this experimental study, only the supplemental air supply with the induced lab air was used in order to keep the flow coefficients within the normal axial compressor operating range. The compressed high pressure air is supplied by the building's air compressors. The mass flow rate for this air supply ranges from 0.0 to 1.0 kg/s and is controlled by a flow rate control valve on the air supply line.

In the stilling chamber, the air from the supplemental supply system is diffused to approximately 3 m/s. The stilling chamber has layers of screens, filters and honeycomb meshes to filter and straighten the flow exiting the chamber through a rectangular ASME

long radius bellmouth nozzle. The chamber also contains a large styrofoam plug covered with foam rubber which prevents the noise of the air supply system from traveling into the cascade test section. A more detailed description on the air supply system and diffuser/stilling chamber is presented by Allison (1982).

Test Section and Moving Endwall System

Figure 3.2 shows a schematic of the AFIT compressor cascade inlet duct (throat) and test section. Since the flow through the throat is parallel to the walls, the inlet air angle for this research was equal to the throat angle of 31 degrees. The test section is constructed of 6061-T6 aluminum and contains eight cascade blades which are equally spaced along the pitchwise height. The interior dimensions of the test section are a pitchwise height between upper and lower walls of 9 in (22.86 cm), a spanwise width of 2 in (5.08 cm) and a length along the axial direction of the flow from the throat to the exit of 12 in (30.48 cm). The test section also contains static pressure wall taps for determining the static pressure in the wake region of the blades and adjustable upper and lower tailboards for balancing the static pressure of the flow at the exit of the cascade.

The cantilever mounted blades are enclosed at the tip by either a stationary or moving endwall. The 2.18 in (5.55 cm) wide full stationary aluminum endwall mounts behind the throat section along the axial length of the test section to enclose the blades. It provides a constant tip clearance gap for all blades of 0.008 chord. For the moving endwall system, the full stationary endwall is replaced by an endwall rotor and two aluminum half walls. Figure 3.3 shows both endwall configurations for the test section.

The rotor can be moved in the spanwise direction of the test section to set the clearance gap. The clearance gap to chord ratios investigated in this research were 0.02, 0.01 and 0.005. To limit the leakage flow between the machined half walls and the rotor, the half walls are adjusted to maintain a 0.025 in (0.0635 cm) gap between the walls and the outer surface of the rotor.

To accurately represent the moving wall effects of an actual compressor rotor, the edges of the moving endwall rotor extended from 0.25 in (0.635 cm) upstream of the blades to 0.25 in. downstream of the blades. The installation of the rotor produced a gap between the throat wall and the upstream edge of the rotor of 0.05 in (0.127 cm) and between the downstream edge of the rotor and the Plexiglas wall of 0.1 in (0.254 cm). These gaps provide space for the maximum wobble in the rotor near its natural frequency. To limit the leakage flow through these gaps, a Teflon scraper and tape were used as gap seals.

Figure 3.4 shows the cross-sectional view of the test section at the trailing edge of the blades. The radial line-of-symmetry for the rotor deviates from the primary passage centerline by 0.05 in (0.127 cm). The curvature of the rotor produces a small variation of 0.0038 in (0.0096 cm) in the size of the tip clearance gaps between blades 4 and 5.

The compressor blades mounted in the test section were NACA 64-A905 blades. The profile of the blades is shown in Figure 3.5, and the coordinates of the pressure surface, suction surface and mean camber line for the blade cross section are listed in Table 3.1. The x value refers to the distance from the leading edge along the blade chord,

and the y value refers to the perpendicular distance from the blade chord. The cascade specifications for the arrangement of the blades in the test section are listed in Table 3.2.

Table 3.1. Blade Surface Coordinates and Mean Camber Line

Suction Surface x (cm)	Suction Surface y (cm)	Pressure Surface x (cm)	Pressure Surface y (cm)	Mean Camber y (cm)
3.751	0.000	3.751	0.000	0.000
3.677	0.015	3.675	0.007	0.011
3.527	0.046	3.524	0.021	0.033
3.303	0.089	3.373	0.035	0.062
3.193	0.111	3.184	0.052	0.081
3.008	0.152	2.994	0.069	0.110
2.709	0.214	2.693	0.099	0.156
2.410	0.269	2.392	0.127	0.198
2.108	0.315	2.093	0.149	0.232
1.803	0.342	1.798	0.160	0.251
1.498	0.345	1.503	0.158	0.251
1.308	0.336	1.318	0.151	0.244
1.118	0.320	1.133	0.142	0.231
0.929	0.297	0.947	0.129	0.213
0.740	0.267	0.761	0.113	0.190
0.551	0.228	0.575	0.092	0.160
0.362	0.179	0.388	0.065	0.122
0.287	0.157	0.313	0.053	0.105
0.212	0.131	0.238	0.040	0.086
0.138	0.101	0.162	0.026	0.063
0.065	0.063	0.086	0.010	0.037
0.029	0.040	0.047	0.002	0.021
0.012	0.025	0.026	-0.002	0.011
0.000	0.008	0.008	-0.003	0.003
0.000	0.000	0.000	0.000	0.000

Table 3.2. Cascade Specifications

Specification	Symbol	Value
Blade Span	h	1.988 in (5.05 cm)
Blade Chord	c	1.50 in (3.81 cm)
Blade Spacing	s	1.0 in (2.54 cm)
Blade Camber Angle	θ	30.51 deg
Blade Inlet Angle	α_1'	26.51 deg
Blade Outlet Angle	α_2'	-4.00 deg
Diffusion Factor	DF	0.332
Point of Maximum Camber	a	0.5 chord
Stagger Angle	ζ	7.50 deg
Air Inlet Angle	α_1	31.0 deg
Average Air Outlet Angle	α_2	3.05 deg
Average Deviation Angle	δ	7.05 deg
Incidence Angle	i	4.49 deg
Average Deflection Angle	ε	27.95 deg
Inlet Velocity	V_1	38.3 m/s
Outlet Velocity	V_2	35.7 m/s

A more detailed discussion on the design and implementation of the moving endwall rotor and compressor cascade blades is presented by Peter (1995).

Data Acquisition System

The data acquisition system for the AFIT cascade facility consists of a central computer, a pressure measurement subsystem, a velocity and temperature measurement subsystem, a temperature measurement subsystem and a probe traverse control subsystem. Figure 3.6 shows the interaction between the different components of the data acquisition system.

Central Computer. The central computer for the data acquisition system is a Zenith Z433 D+ computer with a 33 MHz 486 DX processor chip. The acquisition software employed on this computer was written in MS QuickBasic 4.5. This software package contains several module programs which share common library modules for both data acquisition and reduction. A complete listing of the software is given in Appendix A.

Pressure Measurement Subsystem. The pressure measurement subsystem consists of a Pressure Systems Inc. Model 8400 Pressure Scanner, three 32 port pressure transducer blocks, a CEC Model 2500 Digital Barometer and a five-tube total pressure rake. The pressure scanner and transducer blocks were used to determine total and static pressure differentials from ambient pressure at different locations throughout the cascade test section. The digital barometer measured the ambient pressure in the laboratory for each data acquisition point.

The pressure scanner has an operating scanning rate of 20 kHz. For each pressure measurement, it samples each of the 96 transducer ports 11 times and calculates the arithmetic mean of the 11 values. The pressure scanner contains an internal certified standard transducer which is used for calibration.

The 96 individual transducers within the three transducer blocks measure differential pressures from ambient conditions. Each block also contains a plunger-operated valve to shift the block between calibration mode and acquisition mode. The ports of the transducer blocks are connected to static wall pressure taps in the throat and wake regions, a Pitot tube in the throat region and a total pressure rake in the wake region.

The five-tube total pressure rake was designed to measure the total pressure variations in the wake of the blades with less than 3.5 % area blockage of the passage. The tubing dimensions of the pressure rake are an inside diameter of 0.1016 cm and an outside diameter of 0.147 cm. The tubes are equally spaced such that the distance between centers of adjacent tubes is 0.381 cm.

Velocity and Temperature Measurement Subsystem. The velocity and temperature measurement subsystem consists of a TSI Model IFA 100 Intelligent Flow Analyzer, a TSI Model IFA 200 System Multichannel Digitizer, TSI hot-wire/film probes and a thermocouple.

The IFA 100 was used to acquire velocities from the hot-wire/film probes and temperatures from the thermocouple. Two Model 150 Constant Temperature Anemometer Modules were used to measure the voltages from the probes, and a Model 140 Temperature Module was used to measure the voltage from the thermocouple. In order to use the maximum range of the digitizer, the signal acquired by the IFA 100 was conditioned using three Model 157 Signal Conditioners. For this experimental study, the gain was set to 3.0, the offset was set to 2, and the low pass filter was set to 5 kHz.

The IFA 200 scanned and digitized the voltages from the signal conditioners in the IFA 100 with three Model 252 Digitizers. For this experimental study, the IFA 200 acquired the velocity and temperature voltages at a sample rate of 10 kHz.

Hot-wire and hot-film probes were used to acquire the components of the three-dimensional velocity vector in the cascade flowfield. Since the x-configuration probes can only measure two components of the velocity vector, the probe support was rotated 90

degrees to measure the third component. Explanation of this measurement process is given later on page 4-9. Model 1241-10 and Model 1241-20 x-configuration hot-film probes and Model 1241-T1.5 x-configuration hot-wire probes were used. The different models were employed because several probes were broken during this research.

The thermocouple used in this subsystem measured the total temperature of the flow through the probe calibrator. The thermocouple is an Omega T-type copper-constantan thermocouple.

Temperature Measurement Subsystem. The temperature measurement subsystem consists of a Hewlett-Packard Model 3455A Digital Voltmeter, a Hewlett-Packard Model 3495A Scanner and two Omega T-type copper-constantan thermocouples. This subsystem measured the ambient temperature of the laboratory and the total temperature of the cascade tunnel.

Probe Traverse Control Subsystem. The probe traverse control subsystem was used to accurately position the hot-wire/film probes and the total pressure rake. The axes coordinate system for the cascade test section is shown in Figure 3.7. The y axis is in the pitchwise direction of the cascade, and the z axis is in the spanwise direction. The coordinate inputs for these axes are controlled by two New England Affiliated Technologies Model 310 Programmable Motion Controllers and two Oriental Motor Company Stepper Motors. The positioning of the probes and rake along the x axis was performed manually using a hand crank and a digital encoder readout. The x location was held constant for each individual run. With the hot-wire/film probes and the total pressure rake positioned accurately by the traverse control system, velocity and total pressure data

were collected. Chapter IV will explain the procedures used to collect and reduce the data.

IV. Experimental Procedure

X-Configuration Hot-Wire/Film Calibration

Overview. Hot-wire anemometry was the method used to determine the three components of the total velocity vectors through the linear cascade arrangement. Hot-wire anemometry determines the velocity and direction of a fluid flow by measuring the energy dissipated by each heated wire in the x-configuration when placed in the flow. The two ways of determining this dissipation of energy are the constant temperature method or constant current method. This experimental study incorporated a constant temperature hot-wire method. The procedure for this method is to pass a current through the wire and measure the voltage required to keep the temperature of the hot-wire constant. From the values of the voltage, the velocity of the fluid flow is calculated. With the x-configuration hot-wires, the voltages required to keep each wire at a constant temperature independently of each other are measured. Therefore, the velocities measured by each wire are determined, and the magnitude and direction of the total two-dimensional vector can be calculated if the angle between the wires is known. Implementation of the operating principles of hot-wires and the development of the governing equations used in the tunnel software were accomplished by DeCook (1991:86 to 101).

As previously mentioned, this study used both hot-wire and hot-film probes in the acquisition of experimental velocities and flow angles. The main difference between the two types of sensors is that the hot-film is a quartz cylinder covered by a conductive film rather than a wire.

Governing Equations. The following equations were developed by DeCook (1991) and implemented into the calibration and data reduction software used in this experimental study. The equations are presented here for reference.

The magnitude of the fluid velocity measured by each hot-wire/film sensor of a probe was determined from the wire Reynolds number, starting with:

$$\mathrm{Re} = \frac{\rho \cdot V_{eff} \cdot d_s}{\mu} \tag{8}$$

where V_{eff} is the effective velocity over each sensor and d_s is the diameter of each sensor. The effective velocity is the vector sum of the component of velocity normal to the sensor axis and a fraction of the velocity parallel to the sensor axis. This relationship between effective velocity and fluid flow velocity is assumed to be:

$$V_{eff} = V\sqrt{\sin^2 \alpha + k^2 \cos^2 \alpha} \tag{9}$$

where k denotes the cooling ratio and α is the angle between the sensor axis and the fluid velocity. The cooling ratio is found in the velocity and angle calibration procedure described later in this chapter.

The Reynolds number as defined above is found from the following equation

$$Nu\left(\frac{T_r}{T}\right)^b = A + B\sqrt{Re} + C \cdot Re \tag{10}$$

where the constants A, B, C and the temperature loading factor, b, are determined in the temperature calibration procedure described later. The derivation of the equations listed above are discussed in detail by DeCook (1991).

Calibration Procedure. The procedure for calibrating the x-configuration hot-wire/film probes consists of two parts - the velocity and angle calibration and, secondly, the temperature calibration. The purpose of the first part, velocity and angle calibration, is to determine the cooling ratio, k, and initial values of A, B and C for each sensor of the probe; the purpose of the second part, temperature calibration, is to update the constants A, B and C and determine the temperature loading factor, b, for each sensor.

The velocity and angle calibration involves two separate steps. The first step was to determine the initial values of A, B and C by performing an 11 point unidirectional calibration at a constant temperature with velocities spanning the anticipated range in the cascade passage, in this case 20 m/s to 70 m/s. The second step determines k with an 11 point angle calibration at a constant temperature and velocity with angles spanning the anticipated range in the cascade. The anticipated range of the flow angles for all velocity measurements except the u-v measurements at the x/c = -0.0667 and 0.25 planes was -10 degrees to 10 degrees. Since the flow angles were large and negative for these u-v measurements, the angle calibration range for these values was -32 degrees to -12 degrees. In the first part of the reduction software, the temperature loading factor, b, was set to

zero and temporary values of the constants A, B and C were calculated. In the second phase, the velocities and angles of the flow calculated with these initial calibration coefficients were compared to the velocities and angles measured by the calibrator. A sum squared error (SSE) equation was computed with b set to zero.

$$SSE = \sum_{j=1}^{n} \left(Nu_j \left(\frac{T_{rj}}{T_j} \right)^b - \left(A + B\sqrt{Re} + C \cdot Re \right) \right)^2 \tag{11}$$

The value of k producing the lowest SSE for the angle calibration was chosen. The typical values of k for this experimental study ranged from 0.025 to 0.360 depending on the hot-wire/film being used.

With the cooling ratio of each sensor of the probe determined, the temperature calibration was performed to determine the updated values of the constants A, B, C and b for each sensor. This temperature calibration was accomplished by taking several velocity measurements at a constant zero angle setting while the total temperature of the calibration flow was varied within a 3°C range. The total temperature was held constant while the velocity of the flow was increased from 20 m/s to 70 m/s. After the velocity of the flow reached 70 m/s, the flow temperature was increased by 3°C and the held constant at this higher value as the flow velocity was decreased from 70 m/s to 20 m/s. The range of temperatures used in the calibration were based on the variation expected in the air supply. Equation (11) was used again to determine the value of b for each sensor that produced the smallest SSE. The typical values of b for this study varied from -0.250 to 0.300 depending on the hot-wire/film being used.

Calibration Verification. With the values of the calibration coefficients determined, the calibration of the hot-wire/film probe was checked by comparing the velocities and angles measured by the probe to those known from the calibrator. Measurements were performed at different temperatures, velocities and angles within the calibration range to determine the accuracy of the probe. The results of the calibration verification process showed that the probes were accurate within $\pm$ 0.5 m/s and $\pm$ 0.25 degrees within the calibration temperature range. A detailed outline of the calibration procedure is presented in Appendix B.

Pressure System Calibration

The PSI 8400 pressure scanner was initialized and calibrated each day prior to the data acquisition of the pressures located in the cascade flowfield. The calibration procedure was automated and took less than 3 minutes to accomplish. The calibration process consisted of five point calibrations ranging from -1.0 psid to 1.0 psid for two of the transducer blocks and -5.0 psid to 5.0 psid for the third transducer block. Throughout the day, a quick "re-zeroing" of the calibration for each transducer block was performed to account for minor shifts in the calibration due to temperature changes in the laboratory. Details of the calibration and data acquisition procedures of the PSI pressure scanner are provided in the PSI 8400 Pressure Scanner User's Manual (1993).

Data Acquisition

System Preparation. Prior to the data collection in the cascade, the cascade wind tunnel air supply system was turned on to preheat the test section to the operating temperature, normally in the range of 19-24°C. At the same time, the aluminum rotor was operated at the required RPM to allow it to reach a constant temperature. This warm-up procedure usually required at least 1-1/2 hours.

Temperature variations in the aluminum rotor during operation have an effect on the size of the clearance gap between the blade tips and the endwall rotor. Therefore, the temperature of the rotor was monitored consistently and variations from the pre-heated steady state value did not exceed 1°C. To counter the tendency of the rotor's temperature to increase as the laboratory heated up from the extended facility operation, the laboratory was cooled by an air conditioning system or outside air.

Once the test section and stilling chamber were at a steady state operational temperature and the temperature of the rotor was steady, the entire system was turned off to measure and set the clearance gap. After spin-down, approximately 2 minutes, the size of the clearance gap was measured with the use of feeler gauges. It was noted that the rotor temperature did not drop by more than 1°C during spin-down and measurement. Any adjustments to the rotor-blade gap were made with the rotor positioning mechanism. With the gap set, the entire system was immediately turned back on to reduce any cooling effects from system shutdown. This gap measuring process was performed at start-up each day and any time the temperature of the rotor varied by more than 1°C. A more

detailed explanation on the temperature dependence of the clearance gap is provided by Peter (1995:4-1 to 4-4).

Tailboard Balancing. After system preparation was accomplished, the upper and lower tailboards shown in Figure 3.2 were balanced using the screw adjusters. The reasons behind balancing the tailboards were to adjust the cascade exit pressure to the ambient pressure and to ensure a uniform pressure distribution across the blade exit plane. Using a bank of four water manometers, each tailboard was adjusted so that the static pressure along each board was equal to the ambient pressure. Then matched pairs of ports from the tailboards were compared against each other using the opposing ports of the manometers. For this experimental study, the tailboards were balanced within an average of 0.50 in water, or 0.018 psig.

Total Inlet and Static Pressure Collection. The data acquisition of all total and static pressures in the wind tunnel cascade were made by the PSI 8400 pressure scanner. The raw data received from the PSI scanner had units of differential pressure (psid). Since the reference pressure that the transducer blocks used was ambient pressure, the differential pressure measurements were added to the ambient pressure measured by the digital barometer to determine the absolute pressure measurements.

The inlet total pressure of the cascade was measured by a Pitot tube inserted through the bottom wall in the throat section. The nine inlet and selected nine exit static pressures of the cascade were the arithmetically averaged.

Temperature Collection. The total temperature of the stilling chamber and the ambient temperature were measured by the temperature measurement subsystem at each

data collection point. The raw data read by the computer was in voltages. The data reduction software translated the voltages into temperatures.

Hot-Wire/Film Probe Alignment. The hot-wire/film probe was centered in the spanwise direction between the root wall and the Plexiglas cover, and the z coordinate of this location was set to zero. In order to measure velocities nearer to the endwall rotor, the probe support sleeve was shortened to allow a larger range of motion along the spanwise direction. Using the original support sleeve along the length of the probe holder, the range of travel along the z axis was -0.78 in (-1.98 cm) to 0.78 in. Therefore, the closest tip region measurement location was 0.22 in (0.56 cm) from the moving endwall. The spanwise range of motion for the new probe holder arrangement was -0.9 in (-0.29 cm) to 0.9 in. This range of motion is the maximum possible for the x-configuration hot-wire/film probes because the radius of the probe is 0.1 in. (0.254 cm).

With the airflow turned on, the probe was centered in the pitchwise direction between the trailing edges of the fourth and the fifth blades in the cascade, counting from the top of the cascade down. This location was set as y = 0.0. Figure 3.4 illustrates this location. The testing window for the velocity measurements along the y axis was from -1.0 in (2.54 cm) to 1.0 in. This window covered the primary blade passage between blades 4 and 5, the half blade passage above blade 4 and the half blade passage below blade 5. This pitchwise range was chosen because it covers the region of rotor interaction with the airflow through the cascade.

The pitchwise and spanwise movements of the probe were controlled by the stepper motors and NEAT 310 controllers. The precision of these devices is $\pm$ 0.0005 in (0.0013 cm).

Hot-Wire/Film Data Collection. The data acquisition process for the hot-wire anemometry was automated. Velocity data for this experimental study was taken at five y-z planes in the flowfield of the cascade. The x locations of each plane measured from the leading edge of the blades based on the chord are -0.0667, 0.25, 0.5, 0.75 and 1.0667. At each data collection point, 100 samples of hot-wire/film voltages were taken at a rate of 10 kHz. The arithmetic average of the 100 samples as well as the rms value for each sensor voltage was recorded. For each y-z plane in the flowfield, two separate data collections were performed on each point. First, the u and w components of velocity for a x location were collected with the hot-wire/film probe sensors aligned parallel to the x-z plane. After the probe support was rotated 90 degrees counter-clockwise, the second data collection of the u and v components of velocity for the x location were found with the probe sensors aligned parallel to the x-y plane. To ensure repeatability of the flowfield for the two separate measurements, the two values of u for each point in the y-z plane were compared with each other. If the difference between the two u values was less than the hot-wire/film probe accuracy of 0.5 m/s, the two test runs were considered valid.

Two separate grid spacings were used for the data acquisition of the velocity flowfield with hot-wire anemometry. The spanwise (Δz) and pitchwise (Δy) spacings for the fine grid in the tip region of the flow was 0.02 in (0.0508 cm), and the coarse grid spacings in the center of the blade span was 0.1 in (0.254 cm). The fine grid spacing near

the endwall was needed to properly represent the flow characteristics of the tip region. A detailed outline of the hot-wire/film data collection method is presented in Appendix C.

Total Pressure Rake Alignment and Data Collection. The total pressure rake was centered in the spanwise and pitchwise directions identical to the method used for the hot-wire/film probes. The pressure rake was also aligned parallel to the trailing edges of the blades. The pressure measurements for the total pressure rake were taken at an x location 123% chord downstream of the leading edge of the blades. This position is aligned with the first row of exit static pressure wall ports. All pressure rake test runs were automated and involved a pitchwise transverse of the rake in the testing window. A detailed discussion of the total pressure rake positioning and data collection is presented by Peter (1995:4-8,A-1 to A-2).

Data Reduction

Hot-Wire/Film Data Reduction. The first part of the data reduction process was to convert the raw voltages from the hot-wire/film and thermocouples into velocities and temperatures for each flowfield location. The conversion software for hot-wire/film data uses the inverse form of Equations (8-10) covered earlier. A detailed explanation of this data reduction for hot-wire anemometry is presented by DeCook (1991:93-95). The second part of the data reduction process was to combine the reduced u, v and w components of velocity for each y-z plane into one file. The data was cut and pasted in Microsoft Excel to prepare the proper file format for use with Tecplot. The velocity data is presented in vector plots provided by Tecplot.

Total Pressure Rake Data Reduction. The data reduction software for the pressure rake returned values of T_{amb}, T_{tank}, P_{t1}, p_{static} and ΔP_{local}. The equations outlined in Chapter II were used in Microsoft Excel to calculate the local mass averaged total pressure loss coefficient and the local mass flow rate for each data point. For the calculation of the local mass flow rate, the ΔA from Equation (3) was determined by the product of the pitchwise step size of 0.033 in (0.0838 cm) and pressure rake tube spacing of 0.15 in (0.381 cm).

The values of all local pressure loss coefficients and mass flow rates were used to calculate the mass averaged pressure loss coefficient and mass flow of each region. For the total pressure measurements, the tip region, center region and root region were defined as z = 0.15 to 0.919 in, z = -0.15 to 0.15 in and z = -0.919 to -0.15 in, respectively. The mass averaged total pressure loss coefficient for each region is calculated by

$$\varpi_{region} = \frac{\sum\left(\varpi_{local} \cdot \dot{m}_{local}\right)_{region}}{\dot{m}_{tip} + \dot{m}_{center} + \dot{m}_{root}} \tag{12}$$

A simple addition of the regional values determines the mass averaged value of the total pressure loss coefficient for the testing window. Along with the results regional and overall pressure loss coefficient, contour plots of local pressure loss coefficient are presented in the results.

Error Analysis

Equipment and Instrumentation Accuracies. The equipment accuracies for the pressure transducers, digital barometer and thermocouples were supplied by the manufacturer. The instrumentation accuracies for the hot-wire/film velocity and angle calculations were determined during the calibration process. Table 4.1 summarizes the component accuracies.

Table 4.1. Component Accuracies

Component	Accuracy
Pressure Transducers	0.0005 psid
Digital Barometer	0.005 psia
Thermocouples	0.3°C
Hot-wire/film Velocity	0.5 m/s
Hot-wire/film Angles	0.25 degrees

Estimated Error for the Pressure Loss Coefficient. The error in ϖ due to the accuracies of the equipment and instrumentation was found from the relation

$$ERROR = \frac{\varpi + \delta}{\varpi} - 1 \tag{13}$$

where δ represents the effect of changing the measured values individually to account for their accuracy. For this calculation of error analysis, the error associated with each

measurement is assumed to occur in the same direction for each point of the summation (Spacy, 1993:127). The calculation of the estimated error due to equipment and instrumentation accuracies was 1.3%. The errors in the calculation of ϖ due to the thermal and centrifugal effects of the rotor on tip clearance size were found by Peter (1995:4-3 to 4-7) to be 2% and 1%, respectively. Therefore, the total estimated error in the calculation of ϖ is the sum of the three error individual error estimates which is 4.3%.

V. Results and Discussion

Introduction

The velocity and pressure flowfields measured in this experimental study are presented below. The three-dimensional velocity vector components for the flowfield were measured with hot-wire/film probes. The measurements were taken at one transverse plane upstream of the blade cascade, three planes within the blade cascade and one plane downstream of the blades. The velocity flowfield data is illustrated with vector plots of the components of velocity normalized by the inlet axial velocity at five y-z planes and three x-y planes in the cascade. The five y-z planes investigated were located at axial distances based on chord of -0.0667, 0.25, 0.5, 0.75 and 1.0667 with x = 0.0 at the leading edges of the blades. The three x-y planes investigated were located at z = 0.9 in (2.29 cm), 0.7 in (1.78 cm) and 0.0. From the velocity vector plots of the hot-wire anemometry results, the location and movement of the tip leakage vortex for changes in tip clearance were determined.

Total pressure measurements were taken by the total pressure rake. The pressure flowfield data is presented by mass averaged total pressure loss contours in the wake region of the cascade at a location 23% chord downstream of the trailing edges of the blades. The contours were investigated to determine the effect tip clearance has on the losses in a compressor cascade with a moving endwall.

Velocity Flowfield for the Stationary Flat Endwall

The velocity flowfield for the stationary flat endwall was investigated to determine the tip region flow characteristics associated with this endwall, the inlet flow conditions to the cascade and the periodicity of the flowfield. The velocity vector profiles for the stationary endwall case established a baseline from which comparisons were made. The stationary endwall shown in Figure 3.3 has a blade tip clearance of 0.012 in (0.030 cm). The freestream axial velocity (C_x) for the flat wall case was 78 m/s which corresponded a Reynolds number based on chord of 1.91×10^5. For this case, only three y-z planes of x/c = -0.0667, 0.5 and 1.0667 were investigated.

The velocity vector plots shown in Figures 5.1a and b represent the measured transverse velocity components (v and w) in the wake region at x/c = 1.0667. Figure 5.1b is an enlargement of the fine grid tip region flowfield presented in Figure 5.1a. The trailing edges of blades 4 and 5 are located at y = 0.5 in and -0.5 in, respectively. In the tip region between blades 4 and 5, the presence of two counter-rotating vortices was identified. The tip leakage vortex is located near the suction surface of the fourth blade at y = 0.44 in and shows a counter-clockwise rotation. (For this and all other vector plots presented here, the pressure surface is above blade, the suction surface is below the blade, and the magnitude of the normalized velocity vector is given to the right of the graph.) A larger secondary flow vortex located at y = 0.2 in has a clockwise rotation from the interaction between the tip leakage vortex and the secondary passage flow towards the suction surface. A similar tip leakage vortex and secondary flow vortices were seen by Kang and Hirsch (1993a:440) and Storer (1989:250).

In Figures 5.1a and b, the passage below blade 5 also contains a tip leakage vortex and a secondary flow vortex with similar transverse flow characteristics. The pressure surfaces of both blades 4 and 5 show transverse flows from the pressure sides of the blades towards the blade tips. This spanwise flow towards the tip clearance indicates tip leakage flow. The two flow similarities between the different blade passages is a good indicator of the periodicity of the flowfield for the stationary wall case. Another indicator of the periodicity of the flow is the similar character of vorticity of the flow in each blade passage at the root wall.

The transverse velocity profile at the midchord (x/c = 0.5) is shown in Figures 5.2a and b. Both figures show the position and thickness of the blades at the midchord of the cascade. The clockwise rotation of the flow in the tip region shows the presence of a secondary flow vortex between the pressure side of blade 5 and the suction side of blade 4. The positive v component of the transverse velocity along the suction surfaces near the endwall tends to indicate the rolling up of the tip leakage flow into a vortex. The limitation of the travel of the hot-wire/film probes prevents the presentation of the core of the vortex. That the location of the tip leakage vortex is nearer to the endwall at the midchord than in the wake is expected since tip leakage vortices tend to move away from the endwall as they move downstream (Kang and Hirsch, 1993a:439).

Figure 5.3 shows the transverse flowfield measured upstream of the blades at x/c = -0.0667. This velocity vector profile shows that the extent of the flowfield measured by the hot-wire/film probes immediately upstream of the cascade is essentially two-

dimensional. The w component of velocity is negligible for the stationary endwall case at this axial location.

The streamwise velocity vector plots for the baseline case at z = 0.9 in, 0.7 in and 0.0 in are shown in Figures 5.4, 5.5 and 5.6, respectively. In the entrance plane the average inlet flow angle across the span was slightly low, 28.5 degrees, due to a faulty angle calibration. Downstream planes used a corrected angle calibration. (All other test cases investigated in this study showed an inlet flow angle of approximately 31.0 degrees.) At the midchord of the cascade in Figure 5.4, the decrease in the u component of velocity near the suction surface shows the pitchwise location of the tip leakage vortex because a decrease in axial velocity is a flow characteristic of a tip leakage vortex (Kang and Hirsch, 1993a:439). The wake region of Figure 5.4 also shows a definite decrease in axial velocity for the tip leakage vortices near the suction surfaces. The inflow toward the blade suction surface at the midchord illustrates the effect which can reduce flow separation along suction surface of the blade. Figure 5.4 also shows the underturning of the cascade flow by the tip leakage vortices near the suction surfaces of the blades and the overturning of the flow by the secondary flow vortices beneath the tip leakage vortices.

In Figure 5.5, the local decrease in the axial velocity near the suction surfaces of the blades illustrates the presence of the tip leakage vortex in the wake region. However, the flowfield at the midchord provides no evidence of the vortex. The reason for this difference is that the tip leakage vortex core is located nearer to the endwall at the midchord plane.

The streamwise flowfield at the spanwise center of the cascade ($z = 0.0$) is shown in Figure 5.6. In contrast to the wake profile of Figure 5.5 which showed the location of the tip leakage vortex, the main flow characteristic of Figure 5.6 is the uniform velocity distribution in the wake region for each blade passage. Therefore, the complex flow structure near the endwall region has no noticeable effect on the structure of the flow at the spanwise center of the blade passage.

In summary, the flowfield in the tip region for the stationary endwall with $t/c = 0.008$ was characterized by a tip leakage vortex along the suction surface of the blade and a secondary flow vortex located between the tip leakage vortex and the adjacent blade pressure surface. This tip leakage vortex moves away from the endwall in the streamwise direction. The inlet flow angle to the blade cascade was 28.5 degrees, and the effect of tip clearance on the flowfield near the center of the blade span was negligible. Finally, the flowfield for this test arrangement demonstrated good periodicity.

Velocity Flowfield for Moving Endwall Rotor

The velocity flowfield for the moving endwall rotor was investigated to determine the effects of tip clearance on the flowfield with special emphasis on the characteristics of the flow near the moving endwall. All moving endwall cases were investigated at a flow coefficient (ϕ) of 0.5 which is within the normal operating range for an axial compressor. The three blade tip clearances based on chord investigated in this experimental study were 0.02, 0.01 and 0.005.

Reynolds Number Influence. Two flows with different axial inlet velocities and corresponding Reynolds numbers based on chord (Re_c) were investigated to determine the influence of Re_c on the velocity flowfield. For t/c = 0.02, the transverse velocity vectors in the wake region were studied to determine the influence. With a constant ϕ of 0.5, the two values of C_x were chosen to be 34.15 m/s corresponding to a rotor speed of 1500 rpm and $Re_c = 8.68 \times 10^4$ and 38.3 m/s corresponding to a rotor speed of 1700 rpm and $Re_c = 9.72 \times 10^4$. The limitations on the choice of these two Reynolds numbers was discussed in Chapter I.

Figures 5.7a and b show the transverse velocity flowfield for $Re_c = 8.68 \times 10^4$, and Figures 5.8a and b show the flowfield corresponding to $Re_c = 9.72 \times 10^4$. Both sets of figures show similar wake characteristics of scraped tip leakage vortices next to the pressure surfaces of the blades in the tip region and secondary corner flow vortices near the suction surfaces in the root region. Therefore, the Reynolds number influence on the flowfield characteristics was considered minimal, and all future experimental cases were tested at the larger $Re_c = 9.72 \times 10^4$.

Tip Clearance Based on Chord of 2.0%. The transverse velocity vectors in the wake region (x/c = 1.0667) for t/c = 0.02 are shown in Figures 5.8a and b. The tip region flowfield contains a counter-clockwise rotating tip leakage vortex above the pressure surfaces of each blade. The vortex above the pressure surface of blade 4 (y = 0.5 in) has a different flow structure than the tip leakage vortex in between blades 4 and 5. The differences in the flow structure of the vortex above the fourth blade are caused by the interaction of the tip leakage vortex with two separate boundary layers in this region as

discussed earlier in Chapter II. Since the tip leakage vortex in the blade passage between the fourth and fifth blades is more representative of flow in an actual compressor than the vortex along the pressure surface of the fourth blade, the focus for the remainder of this chapter will be on the primary passage flowfield between the blades.

The tip leakage vortex for the primary blade passage is shown in Figure 5.8b. This tip leakage vortex has moved from the stationary wall location along the suction surface across the blade passage to the pressure surface of the other blade. This scraping effect of the tip leakage vortex is caused by the increased mass flow through the gap with rotor motion and the viscous dragging forces of the rotor boundary layer (Kunz et al., 1993:464). The tip leakage vortex extends along the passage from y = -0.46 in to 0.32 in with the center of the vortex located at approximately y = -0.08 in. This moving endwall case with t/c = 0.02 shows no evidence of a secondary flow vortex along the endwall between the pressure surface of blade 5 and the suction surface of blade 4 as was seen in the stationary wall case. The wake flowfield from z = -0.9 in to 0.6 in exhibits a similar behavior to the wake flowfield for the stationary baseline.

The transverse velocity vectors for x/c = 0.75 and t/c = 0.02 are shown in Figures 5.9a and b. The flowfield outside the tip region shows little transverse motion near z = 0.0. Figure 5.9b shows the counter-clockwise rotation of a tip leakage vortex from y = -0.24 in to 0.4 in with the center of rotation for the vortex approximately located at y = 0.16 in. The locations of the tip leakage vortex in Figures 5.8b and 5.9b show a downward shift of the vortex center towards the pressure surface of blade 5. This

downward motion is attributed to the viscous forces in the boundary layer of the moving endwall and the presence of tip leakage flow.

Figures 5.10a and b show the transverse flowfield for x/c = 0.5 and t/c = 0.02. At this midchord location, the presence of the tip leakage vortex is not evident from the figures. Therefore, the tip leakage vortex must be near the moving endwall outside the testing window. However, the formation of secondary flow corner vortices near the suction surfaces of the blades is evident along the root wall for this test case. At the quarter chord (x/c = 0.25), Figure 5.11 shows similar skewing of the transverse vectors in the tip region as seen in Figures 5.10a and b for the midchord location. This small amount of vorticity was caused by the viscous forces in the rotor boundary layer.

Figure 5.12 illustrates the near two-dimensionality of the flowfield upstream (x/c = -0.0667) of the blades. However, the transverse vectors near the pressure surfaces of the blades and the moving endwall do have a spanwise component (w) of the velocity. This spanwise velocity component was not noticed for the stationary wall baseline case. The spanwise component is attributed to the rotor motion.

Figures 5.13 and 5.14 show the streamwise velocity vectors near the moving endwall at z = 0.9 in and 0.7 in, respectively. The inlet flow angle into the cascade for each x-y plane was approximately 31.0 degrees. A local decrease in axial velocity near and moving away from the suction surface of blade 4 is illustrated in Figure 5.13 at the quarter chord. This decrease suggests the roll-up of the tip leakage flow into a tip leakage vortex. At locations downstream of the quarter chord, the decrease in velocity spans most of the primary passage. This result is expected because the tip leakage vortex seen in

Figures 5.8b and 5.9b covers almost 70% of the primary passage pitch near the moving endwall. The velocity vectors in the wake region indicate the underturning of the flow by the tip leakage vortex. The effects of the tip leakage vortex are not seen in Figure 5.14 since the tip leakage vortex is centered at z = 0.84 in. The streamwise flowfield at the spanwise center of the passage is shown in Figure 5.15. This flowfield shows no effects of the complex flow characteristics of the tip region as emphasized earlier in the discussion of the stationary endwall baseline.

In summary, the three-dimensional flowfield in the tip region for the moving endwall with t/c = 2% had different flow characteristics than the stationary wall baseline flowfield. For the moving wall case, the tip leakage formed on the suction surface of blade 4 has been scraped down the pitchwise direction of the primary passage towards the pressure surface of blade 5. Along with the translation of this vortex, its tight core noticed for the stationary wall case has been spread out over 70% of the blade pitch with the addition of the boundary layer effects of a moving endwall. However, the addition of the moving endwall rotor did not change the structure of the flowfield away form the tip region of the blade passage.

Tip Clearance Based on Chord of 1.0%. The transverse velocity vectors for the flowfield in the wake region with t/c = 0.01 are shown in Figures 5.16a and b. The discussion of the tip region flowfield for this tip clearance will focus on the primary passage for the reasons stated earlier in this chapter. Like the case with t/c = 0.02, the tip region flowfield is characterized by a scraping vortex near the pressure surface of blade 5. Figure 5.16b shows the location and structure of this tip leakage vortex. The core of the

vortex is located at y = -0.18 in, and the vortex structure is spread out in the pitchwise direction to cover approximately 60% of the blade pitch near the moving endwall. The location of the scraped tip leakage vortex core in Figure 5.16b at z = 0.86 and y = -0.18 in is closer to the endwall and pressure surface of blade 5 than the vortex core for t/c = 0.02 in Figure 5.8b located at z = 0.84 in and y = -0.08 in. This variation in the location of the tip leakage vortex with changes in tip clearance was also determined by Inoue et al. (1985:4). The flowfield outside the tip region of the blade passage as shown in Figure 5.16a is similar to that of the 2% tip clearance case. For this reason, only the flowfield in left half of the blade passage near the tip region was investigated for the other four y-z planes at t/c = 1%.

The transverse flowfield near the tip region for x/c = 0.75 and t/c = 0.01 is shown in Figures 5.17a and b. The location of the vortex at the three-quarters chord is closer to the moving endwall and the suction surface of blade 4 than its position in the wake region. At x/c = 0.75, the vortex structure is spread out from y = -0.2 in to 0.4 in with the location of the vortex core at 0.06 in. Therefore, an inward spanwise movement away from the moving wall and a downward pitchwise movement towards blade 5 are associated with the streamwise progression of the tip leakage vortex. This result was also noticed for the tip clearance case of 2%. In Figures 5.16b and 5.17b, no evidence of secondary flow in the tip region from the pressure surface of blade 5 to the suction surface of blade 4 was found.

The plots of transverse velocity vectors in the midchord plane for t/c = 0.01 are shown in Figures 5.18a and b. Like the 2% clearance plots of Figures 5.10a and b, no

evidence of the tip leakage vortex is illustrated in Figures 5.18a and b. However, Figures 5.18a and b show some skewing of the velocity vectors near the moving endwall. This vorticity in the tip region is caused by the dragging effect of the viscous forces in the moving endwall boundary layer. Figures 5.19 and 5.20 also show some skewing of the transverse velocity vectors along the blade surfaces for t/c = 1%, but this flowfield is essentially two-dimensional in the testing window measured by the hot-wire/film probe. The skewing of the velocity vectors near the moving endwall was also shown in the 2% chord tip clearance case.

The streamwise flowfield for the tip region near the moving rotor at z = 0.9 in is illustrated in Figure 5.21. The inlet flow angle for this moving endwall case was measured as approximately 31 degrees. Like the 2% clearance case, a local decrease in axial velocity at the quarter chord tends to indicate the pitchwise location of the tip leakage vortex. However, this location for t/c = 0.01 is closer to the center of the passage than was seen in Figure 5.13 for t/c = 0.02. In Figure 5.21, the spreading of the region of low axial flow velocity downstream of the quarter chord is illustrated. The underturning of the flow in the cascade by the tip leakage vortex is illustrated by the velocity vectors in the wake region. In Figures 5.22 and 5.23, the streamwise velocity vectors for the x-y planes at z = 0.7 in and z = 0.0 show nearly uniform wakes for the primary blade passage. The effects of the complex tip region flowfield are not noticed in the flows of Figures 5.22 and 5.23. The reduction in axial velocity behind blade 4 in Figure 5.22 is due to the vortex above the pressure side of the blade.

In summary, three-dimensional flowfield in the tip region for the moving endwall with t/c = 1% had the same qualitative characteristics as the flowfield for t/c = 2%. However, the scraped tip leakage vortex at each y-z plane in the cascade for the 1% tip clearance case was located closer to the moving endwall and the pressure surface of blade 5. A smaller and tighter core vortex was also illustrated in the 1% tip clearance case. This fact indicates less diffusion of the vortex core for t/c = 0.01. The change in tip clearance did not alter the structure of the flowfield away from the tip region of the blade passage.

Tip Clearance Based on Chord of 0.5%. The transverse velocity vectors in the wake region of the cascade flowfield are illustrated in Figures 5.24a and b. The flowfield outside the tip region for t/c = 0.005 has the same characteristics as the other tip clearance flows investigated. Secondary corner vortices were formed along the suction surface of the blades near the root wall for all the tip clearance cases. In the tip region flowfield of the primary passage shown in Figure 5.24b, the position of the scraped tip leakage vortex has changed from the position determined in the previous analysis for t/c = 0.01. Although the vortex occupies the same pitchwise location in the blade passage, its vortex core has moved towards the moving endwall for t/c = 0.005. The spanwise width of the testing window for the hot-wire/film probes was only able to capture half of the tip leakage vortex flow structure.

At x/c = 0.75, the scraped tip leakage vortex shown in Figures 5.25a and b has moved towards the suction surface when compared with the vortex in Figure 5.24b. This movement from the suction surface of blade 4 to the pressure surface of blade 5 was also

found for the tip clearance cases of 2% and 1%. The core of the vortex in Figure 5.25b is located at y = 0.06 in and centered on the left side of the testing window. The influence of a secondary flow vortex in the tip region of Figures 5.25a and b is shown by the clockwise rotation of the flow outside the tip leakage vortex. This secondary flow vortex motion is also illustrated at the midchord in Figures 5.26a and b.

The transverse flowfield at x/c = 0.25 for a tip clearance of 0.5% is illustrated in Figure 5.27. Like the previous tip clearance cases, some vorticity is present in the tip region flowfield, but the flow closely resembles two-dimensional flow within the testing window. This nearly complete two-dimensional characteristic flow is illustrated in Figure 5.28 at x = -0.0667 for t/c = 0.005.

The streamwise velocity vectors for the tip region flowfield at z = 0.9 in for this gap size are illustrated in Figure 5.29. The measured inlet flow angle is approximately 31 degrees which agrees with the values determined with 1% and 2% tip clearances. The velocity vectors above the fourth blade at x/c = -0.0667 show the influence of the stationary half wall and moving endwall boundary layers on the flow within this blade passage. In contrast to the other cases of t/c = 2.0% and 1.0%, a local decrease in axial velocity near the suction surface at the quarter chord is not seen because the location of the tip leakage vortex is closer to the moving endwall for this tip clearance of 0.5%. However, the local decreases in axial flow across the velocity profiles at x/c = 0.75 and 1.0667 indicate the presence of the scraped tip leakage vortex. The underturning of the cascade flow by the tip leakage vortex is again illustrated by the velocity vectors in the wake region. The streamwise velocity profiles for t/c = 0.5% of Figures 5.30 and 5.31 at

z = 0.7 in and 0.0, respectively, are uniform in wake region in the primary blade passage. These profiles indicate an independence of the flowfield at these locations from the influences of the complex tip region flow characteristics.

In summary, the flow characteristics of the cascade flowfield for t/c = 0.5% were similar to those determined at the tip clearances of 1% and 2%. All three flowfields outside the tip region showed little change in character with changes in tip clearance. However, the scraped tip leakage vortex was found to move closer to the moving endwall rotor and pressure surface of blade 5 with a reduction in tip clearance size. At small tip clearances ($t/c \leq 1\%$), the influence of secondary flow vortex into the tip region was seen. Therefore, the size of the tip clearance gap has an effect on the location and size of the tip leakage vortex and the presence of secondary flow within a blade passage.

Velocity Flowfield Analysis of Crenulated Blade Design

An experimental investigation of the flowfield for crenulated trailing edge blades was performed at the flow coefficient of 0.5. The purpose of crenulated blades is to improve the wake mixing and decrease the overall passage losses. Several experiments at AFIT have been conducted to determine a crenulated blade geometry that optimizes the purpose of the blades (DeCook, 1991; Costello, 1993; Spacy, 1993). The crenulated blade design used for this study was developed by Spacy (1993) and modified by Peter (1995:5-15). Figure 5.32 shows the crenulation geometry for this blade. A tip clearance based on chord of 1% was used for this investigation.

The transverse velocity vectors in the wake region (x/c = 1.0667) of the crenulated blades are shown in Figures 5.33a and b. The crenulated blade wake region is characterized by vortical mixing of the pressure side and suction side flows along the trailing edges of the blades than in Figures 5.16a and b for the straight blades at t/c = 0.01. This increased activity in the wakes of the blades is expected since the purpose of the crenulations is to improve wake mixing. Secondary flow corner vortices near the suction surface of the blade and along the root wall are illustrated in Figure 5.33a. However, the wake mixing caused by the crenulations in the blades has decreased the size of these vortices from those shown in Figure 5.16a. Therefore, the aerodynamic losses associated with a large corner vortex were reduced with the application of crenulations in the blade geometry.

For the tip region shown in Figure 5.33b, the tip leakage vortex scraped from the suction surface of blade 4 towards the pressure surface of blade 5 is located in a position very similar to the straight edge vortex in Figure 5.16b. However, the intensity of the vortex determined from the magnitude of its transverse vectors is considerably less for the crenulated blade than for the straight edge blade. A reduction in the intensity of the scraping tip leakage vortex due to wake mixing will also reduce the losses in the passage. The location of the first crenulation in the blades with respect to the moving endwall is between z = 0.625 in and 0.875 in. This crenulation is located within the tip region flowfield.

The upstream effects of the crenulations in the blades are shown in Figures 5.34a and b for x/c = 0.75. The transverse flowfield vectors in the tip region show the pitchwise

location of the scraped tip leakage vortex between y = -0.28 in and 0.32 in. The introduction of crenulated blades into the flowfield has caused the vortex core to move closer to the moving endwall. Again, the intensity of the crenulated vortex is less than the one determined previously for the straight blades. As shown in Figures 5.35a and b for the crenulated blade and in Figures 5.18a and b for the straight edge blade, the differences in the transverse flowfields for each type of blade at x/c = 0.5 are minor.

Figure 5.36 shows the streamwise velocity vectors for the flowfield of the crenulated blades at z = 0.9 in. The evidence of a tip leakage vortex near the three quarters chord location is shown by the decrease in axial velocity across the blade pitch of the primary passage. However, the intensity of this vortex has reduced in the wake region. The increase in axial velocity from the x/c = 0.75 location to the x/c = 1.0667 location is an indication of this reduction in tip leakage vortex intensity from the mixing of the flowfield in the wake region. Figures 5.37 and 5.38 for the spanwise locations of z = 0.7 in and 0.0, respectively, show near uniform velocity profiles in the wake region of the crenulated blades. The reduction in axial velocity behind blade 4 in Figure 5.37 is due to the vortex above the pressure side of the blade.

In summary, the crenulated blades increased the mixing of the flowfields in the wake region. The wake mixing caused by the crenulated blades reduced the intensity of the tip leakage vortex and secondary corner vortex within the blade passage. This reduction in intensity will decrease the aerodynamic losses associated with these two types of vortices.

Total Pressure Losses for Moving Endwall

A total pressure rake was used to collect data for the calculation of the losses in total pressure across the linear cascade. The data was taken at a cascade flow coefficient of 0.5 and a Reynolds number based on chord of 9.72×10^4. Contour plots of local mass averaged total pressure loss coefficient were produced for the straight blade cases with t/c = 0.02, 0.01 and 0.005 and for the crenulated blade case with t/c = 0.01.

Local Total Pressure Loss Coefficient Contour Plots. The contour plot of ϖ for the tip clearance case of 2% chord is shown in Figure 5.39. The location of the cores of the secondary flow corner vortices near the suction surface and root wall corners are well defined by the contours of total pressure loss. The largest total pressure losses are associated with the vortex located above the pressure surface of blade 4. In the center span of the blade passage, the only losses present are those caused by the blade wakes. The tip region flowfield of the primary blade passage shows high loss regions associated with the moving endwall boundary layer. This endwall boundary layer covers the entire blade pitch which was expected from the results of Peter (1995) on the progression of boundary growth along the pitch with decreasing ϕ. However, the presence of the scraped tip leakage vortex is not evident in Figure 5.39. The limitation of the tube spacing for the total pressure rake has already been discussed in Chapter I. The largest ϖ contour found in the testing window had a magnitude of 0.800 and a location near the tip of blade 4.

Figure 5.40 shows the contours of ϖ for the tip clearance case of 1% chord. The characteristics of this contour plot are similar to those in Figure 5.39. Again, well-defined loss contours show the location of secondary corner vortices, blade wakes, the non-

representative vortex and the moving endwall boundary layer. However, largest ϖ contour found near the tip of blade 4 was 0.725

Figure 5.41 shows the contours of ϖ for the tip clearance case of 0.5% chord. The character of this contour plot is similar to that of the previous two contour plots. However, the locations of the secondary corner vortices have moved toward the center of the blade span. The largest ϖ contour for this tip clearance found near the tip of blade 4 was also 0.725.

The contour plot of ϖ for the crenulated blades with t/c = 0.01 is shown in Figure 5.42. The loss contours for this test case have a different character than those for the straight edge blades discussed earlier. The largest loss coefficient associated with the secondary flow corner vortices is 0.500 which is a 13% reduction in the losses due to this vortex. The well-defined blade wakes for the crenulated blades also have lower losses than those of the straight edge blades. The moving endwall boundary layer is also thinner for the crenulated blade case and has a maximum value of 0.575 which accounts for a 11.5% reduction in the highest measured loss in the boundary layer. Therefore, the contour plots of ϖ for the crenulated blades indicate a reduction in the total pressure losses within the cascade for the change in blade geometry.

Values of Mass Flow and Total Pressure Losses. The regional values for the mass flow rate and total pressure loss coefficient were determined at the tip, center and root of the testing window from the Equations (3) and (12), respectively. The mass flux distributions for the straight edge blades with 2%, 1% and 0.5% chord tip clearances and the crenulated blades with 1% chord tip clearance are presented in Table 5.1. These mass

flux distributions for each region were computed by dividing the regions average mass flow by the fraction of the span covered by that region. Since the mass flux distribution follows the inverse of the total pressure losses, the low losses associated with the center of the blade span make its mass flux greater than the other regions. The high total pressure losses associated with the tip and root regions limit or block the mass flow through that region. The mass flux distribution for each region decreased as the tip clearance was increased. Overall, the largest difference in mass flux distribution between the 2.0% and 0.5% chord tip clearance test cases varied by approximately 2.2%.

Table 5.1. Mass Flux Distribution by Region

	Tip Region	Center Region	Root Region
Fraction of Span in Region	0.378	0.225	0.378
Test Case	Mass Flux Distribution (Region Mass Flow / Region Fraction) (kg/s)		
Straight, t/c = 0.005	0.0922	0.1038	0.0992
Straight, t/c = 0.01	0.0908	0.1029	0.0981
Straight, t/c = 0.02	0.0889	0.1023	0.0975
Crenulated, t/c=0.01	0.0944	0.1006	0.0949

The regional and passage mass averaged total pressure loss coefficients for each test case are presented in Table 5.2. These coefficients included only the losses in the passage between the fourth and fifth cascade blades. Tip region values of ϖ are approximately 50% higher than the values measured by Peter (1995:5-19) at $\phi = 1.5$ and $Re_c = 3.0 \times 10^5$. These larger values of ϖ discovered in this experimental study were

Table 5.2. Regional and Passage Total Pressure Loss Coefficients

Test Case	Straight t/c = 0.5%	Straight t/c = 1.0%	Straight t/c = 2.0%	Crenulated t/c = 1.0%
ϖ_{tip}	0.0456	0.0460	0.0460	0.0371
ϖ_{center}	0.0084	0.0081	0.0087	0.0050
ϖ_{root}	0.0287	0.0289	0.0293	0.0281
$\varpi_{passage}$	0.0827	0.0830	0.0839	0.0701

expected since Horlock (1973) showed that Reynolds numbers less than 1×10^5 increase the total pressure loss coefficients. Therefore, the increase in magnitude of total pressure loss coefficient between this study and the one completed by Peter (1995) is caused by the change in flow conditions.

For all the test cases presented in Table 5.2, the largest mass averaged total pressure loss coefficient is located within the tip region. This tip region value of ϖ accounts for approximately 45% of the passage losses. The variation of the regional losses with changes in tip clearance is less than 2%. However, the use of crenulated blades in the cascade test section reduced the tip region pressure loss coefficient by 19.4%. Therefore, the wake mixing caused by the blade crenulations reduces the pressure losses associated with the tip clearance flows.

Summary

Three-dimensional velocity measurements were taken throughout the blade cascade to determine the effects of tip clearance on the velocity vectors of the flow. For the 90% of the blade span covered by the hot-wire/film probe, the flows at x/c = -0.0667

and 0.25 were essentially two-dimensional for all tip clearances at the flow coefficient of 0.5. The flowfields outside the tip region showed similar velocity vector profiles for all tip clearances investigated. The initial presence of the tip leakage vortex near the suction surface of the blade and the movement of the vortex across the blade pitch to the pressure surface of another blade was illustrated in the results. However, the tip leakage vortex moved closer to the pressure surface of the adjacent blade with decreasing tip clearance.

Total pressure rake data was collected in the wake region behind the blades to determine the effects of tip clearances on total pressures losses. The results for mass averaged total pressure loss coefficient showed small changes in ϖ for changes in tip clearance. However, losses do increase with increasing tip clearance.

The use of crenulated blades within the compressor cascade reduced the intensity of the vortices within the blade passage, as shown in the velocity vector profiles. The crenulated blades also reduced the magnitude of the losses in the blade passage investigated.

VI. Conclusions and Recommendations for Further Research

Conclusions

From the results found in this experimental study, the following conclusions were drawn on the flow features found within a linear compressor cascade with a moving endwall and the effects changes in tip clearance and blade geometry had on the features.

The analysis of the velocity vector plots in both the transverse and streamwise planes for the stationary endwall case show both a tip leakage vortex and a secondary flow vortex within the primary blade passage. The secondary flow vortex is not present in the test case for a moving endwall and t/c = 0.02 chord, but it is present for the other tip clearances. The increased tip leakage flow through the larger blade gaps tends to remove the secondary flow vortex in the passage.

Outside the region near the moving endwall, the velocity vector and the total pressure loss contour plots show no effect of tip clearance on the flowfield within the blade passage. Therefore, changes in tip clearance only affect the flow characteristics in the blade tip region. This conclusion was also found by Peter (1995) for a linear compressor cascade with a moving endwall.

The streamwise velocity vector plots near the moving endwall show that the tip leakage flow rolls up into a vortex along the suction surface of a blade upstream of the quarter chord streamwise location and is scraped across the blade pitch to the pressure surface of an adjacent blade with its downstream progression. This formation and movement of the tip leakage vortex was also seen by Kunz et al. (1993).

The turning of the flow by the cascade blades in the tip region is affected by the tip leakage and secondary flow vortices. The tip leakage vortex underturned the flow, and the secondary flow vortex overturned the flow. The location and size of the vortices affect the ability of the compressor blades to properly turn the flow.

For decreases in tip clearance, the location of the scraped tip leakage vortex moves towards the moving endwall in the spanwise direction and the pressure surface of the blade in the pitchwise direction. Therefore, smaller tip clearances confine the high losses associated with the tip region to a smaller area near the moving endwall and pressure side of the blade. The reductions in ϖ_{tip} found for decreasing tip clearances support this conclusion. This reduction in the tip region total pressure losses was also discovered by Peter (1995). However, the larger values of total pressure loss coefficient found in this study compared with those found by Peter show that changes in flow conditions such as the flow Reynolds number and the flow coefficient have a definite influence on the losses found within a blade passage of a compressor cascade with a moving endwall.

The crenulated blade design investigated in this study reduces the intensity of the scraped tip leakage vortex and the secondary flow corner vortex within a blade passage. This reduction in vortex intensity decreases the total pressure losses within the blade passage. Therefore, the crenulated blade geometry provides an excellent means of decreasing the aerodynamic losses found within an axial compressor.

Recommendations for Further Research

From the results and conclusions determined in this experimental study, recommendations for further research involving the use of the linear compressor cascade with moving endwall are made.

Although this research provided experimental data on the effects of tip clearance at the flow coefficient of 0.5, the investigation of other flow coefficients within the normal axial compressor operating range of 0.3 to 0.7 should be investigated. As documented by Peter (1995), variations in flow coefficient affect the total pressure losses. The results of the new experiments coupled with those from this research and the research by Peter would allow a conclusion to be made on the effect that moving endwall speed has on the tip region flowfield.

Typical axial compressor flow Reynolds numbers are 2.0×10^5 to 4.0×10^5 based on chord should be investigated to determine possible changes in the flowfield with increasing Reynolds number. The increase in Reynolds number would require the installation of sound suppressant material near the tunnel entrance to reduce the squealing sound.

The current experimental setup could be modified to investigate blade tip modifications such as endcaps and moving endwall treatments. Also, the effect of freestream turbulence intensity on the velocity and pressure flowfields of the linear cascade with moving endwall should be investigated.

Two experimental apparatus modifications are needed for the AFIT Wind Tunnel Cascade Facility. A traverse control system that is not connected to the test section would

allow hot-wire/film boundary layer probes to be used to gather data within the blade tip clearance gap. The software used for this research was written over five years ago and does not integrate well with the data acquisition system currently in use. A new "user friendly" software package needs to be developed for the cascade facility.

References

Allison, D.M., "Design and Evaluation of a Cascade Test Facility," MS Thesis GAE/AA/81D-2, Air Force Institute of Technology (AU), Wright-Patterson AFB, OH, June 1982.

Cohen, H., Rogers, G.F.C. and Saravanamutto, H.I.H., Gas Turbine Theory (Third Edition). John Wiley and Sons, New York, 1987.

Costello, M.J., "Off-Design Performance of Crenulated Blader in a Linear Compressor Cascade," MS Thesis GAE/ENY/93D-1, Air Force Institute of Technology (AU), Wright-Patterson AFB, OH, December 1993.

DeCook, S.J., "Experimental Investigation of Trailing Edge Crenulation Effects on Losses in a Compressor Cascade," MS Thesis GAE/ENY/91D-1, Air Force Institute of Technology (AU), Wright-Patterson AFB, OH, December 1991.

Dixon, S.J., Fluid Mechanics, Thermodynamics of Turbomachinery. Pergamon Press, Oxford, 1986.

Hah, C., "A Numerical Modeling of Endwall and Tip-Clearance Flow of an Isolated Compressor Rotor," Transactions of ASME, Journal of Engineering for Gas Turbines and Power, V108, pp. 15-21, January 1986.

Herzig, H.Z., Hansen, A.G. and Costello, G.R., "A Visualization Study of Secondary Flows in Cascades," NACA Rep 1163, 1954.

Horlock, J.H., Axial Flow Compressors. Robert E. Krieger Publishing Company, Huntington, New York, 1973.

Inoue, M., Kuromaru, M. and Fukuhara M., "Behavior of Tip Leakage Flow Behind an Axial Compressor Rotor," ASME Paper 85-GT-62, Houston, TX, March 1985.

Kang, S. and Hirsch, C., "Experimental Study on the Three-Dimensional Flow Within a Compressor Cascade With Tip Clearance: Part I - Velocity and Pressure Fields," Transactions of ASME, Journal of Turbomachinery, V115, pp. 435-443, July 1993.

Kang, S. and Hirsch, C., "Experimental Study on the Three-Dimensional Flow Within a Compressor Cascade With Tip Clearance: Part II - The Tip Leakage Vortex," Transactions of ASME, Journal of Turbomachinery, V115, pp. 444-450, July 1993.

Kunz, R.F., Lakshminarayana, B. and Basson, A.H., "Investigation of Tip Clearance Phenomena in an Axial Compressor Cascade Using Euler and Navier-Stokes Procedures," Transactions of ASME, Journal of Turbomachinery, V115, pp. 453-467, July 1993.

Lakshminarayana, B., "Experimental Investigation on the Effects of Tip Clearance in Turbomachinery," von Karman Institute for Fluid Dynamics Lecture Series 1985-05, April 1985.

Lakshminarayana, B., Sitaram, N. and Zhang, J., "End-Wall and Profile Losses in a Low-Speed Axial Flow Compressor Rotor," ASME Paper 85-GT-174, Houston, TX, March 1985.

Pandya, A., and Lakshminarayana, B., "Investigation of the Tip-Clearance Flow Inside and at the Exit of a Compressor Rotor Passage - Part I: Mean Velocity Field," Transactions of ASME, Journal of Engineering for Power, V105, pp. 1-12, January 1983.

Peter, L.J., "Influence of a Moving Wall on the Tip Clearance Vortex in an Axial Compressor Cascade," MS Thesis GAE/ENY/95D-19, Air Force Institute of Technology (AU), Wright-Patterson AFB, OH, December 1995.

PSI 8400 Pressure Scanner User's Manual, Hampton, VA: Pressure Systems, Incorporated, March 1993.

Spacy, W.L. II, "Effects of Crenulations on Three-Dimensional Losses in a Compressor Cascade," MS Thesis GAE/ENY/93D-1, Air Force Institute of Technology (AU), Wright-Patterson AFB, OH, December 1993.

Stauter, R.C., "Measurement of the Three-Dimensional Tip Region Flow Field in an Axial Compressor," Transactions of ASME, Journal of Turbomachinery, V115, pp. 468-476, July 1993.

Storer, J.A., "The Interaction Between Tip Clearance Flow and the Passage Flowfield in an Axial Compressor Cascade," ISABE Paper 89-7024.

Storer, J.A. and Cumpsty, N.A., "Tip Leakage Flow in Axial Compressors," Transactions of ASME, Journal of Turbomachinery, V113, pp. 252-259, April 1991.

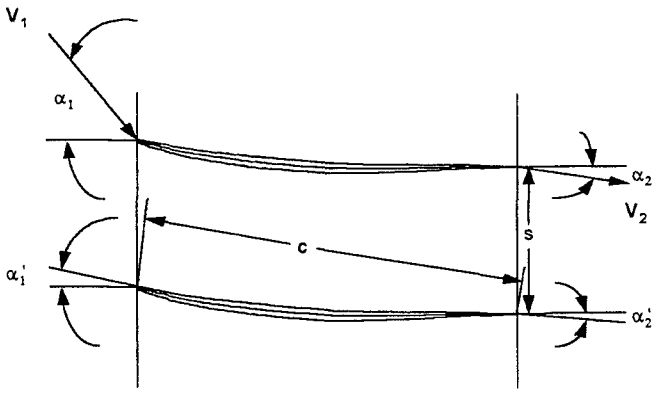

Figure 2.1. Cascade Nomenclature

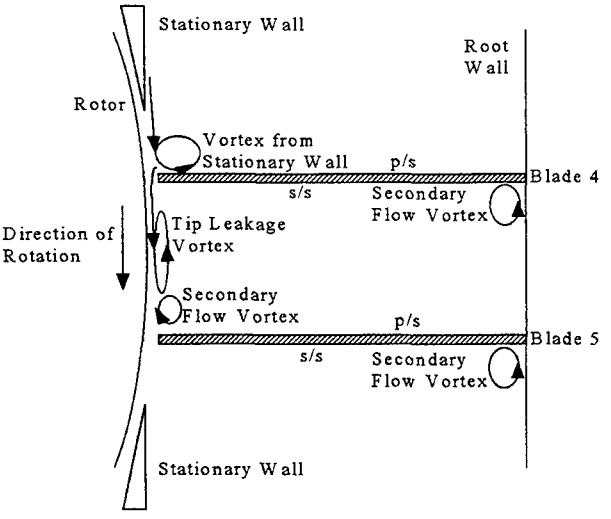

Figure 2.2. Linear Compressor Cascade with Moving Endwall Flowfield Description

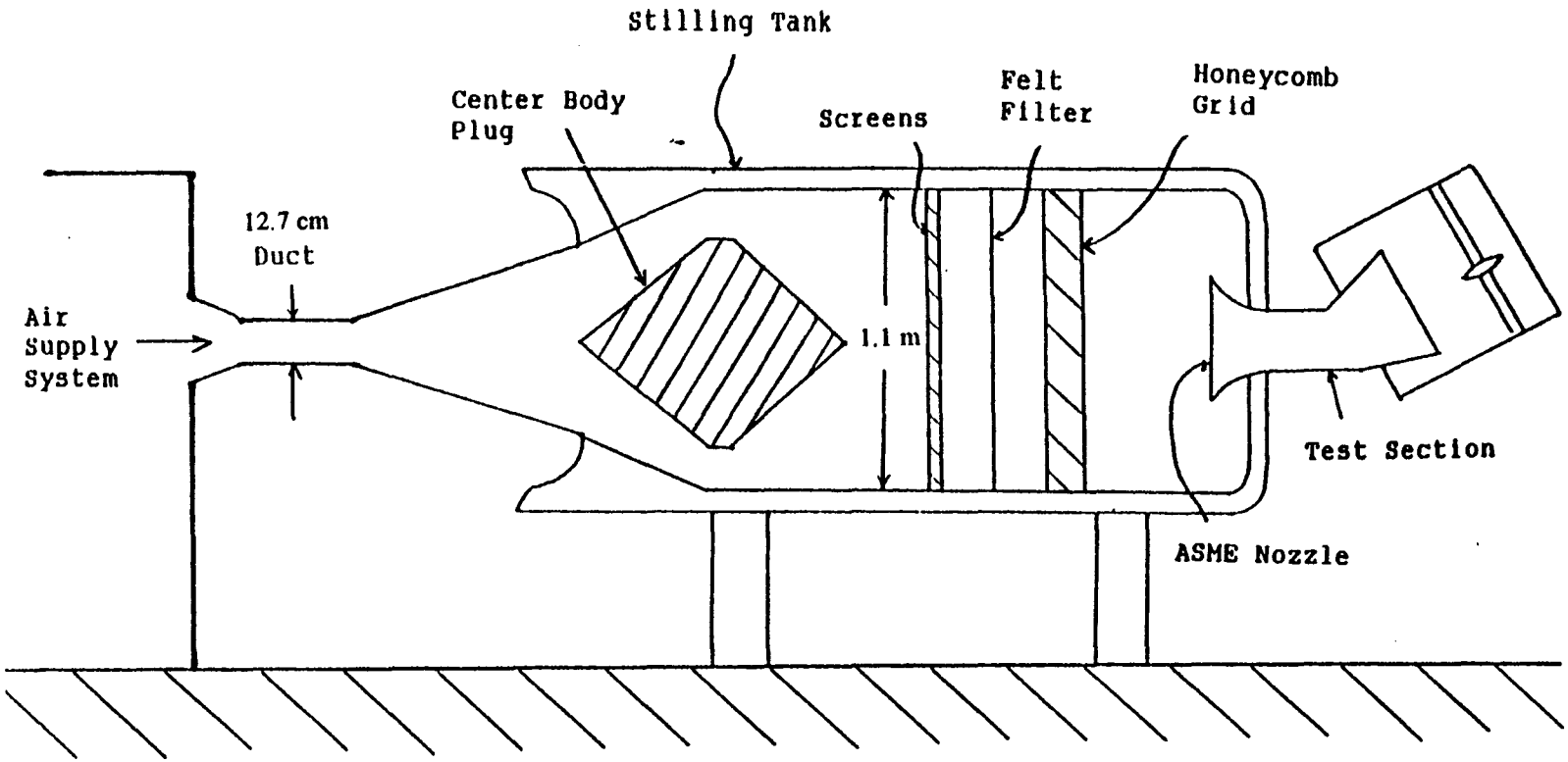

Figure 3.1. Air Supply System and Diffuser/Stilling Chamber (Costello, 1993:69)

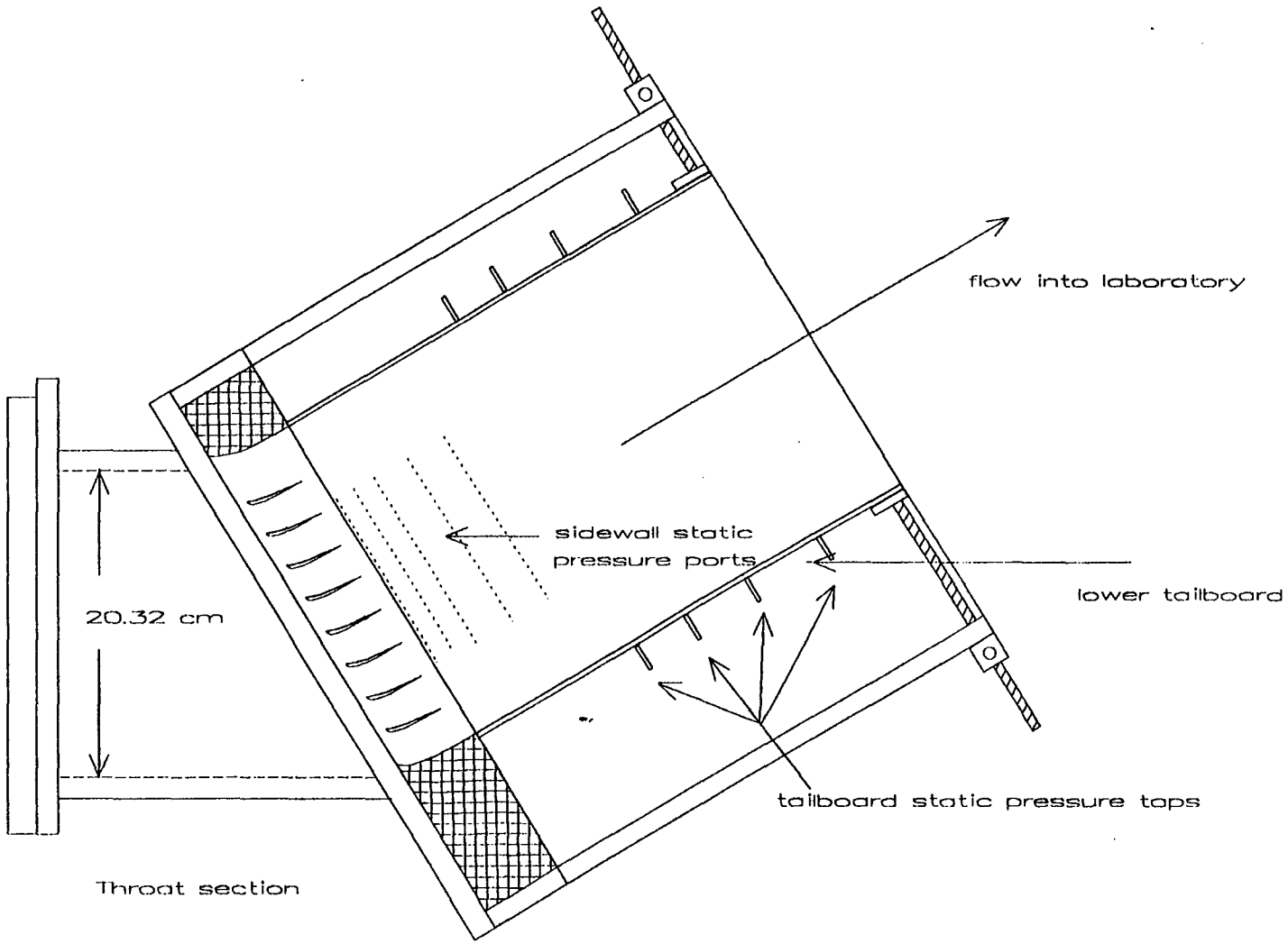

Figure 3.2. Cascade Test Section (Peter, 1995:7-6)

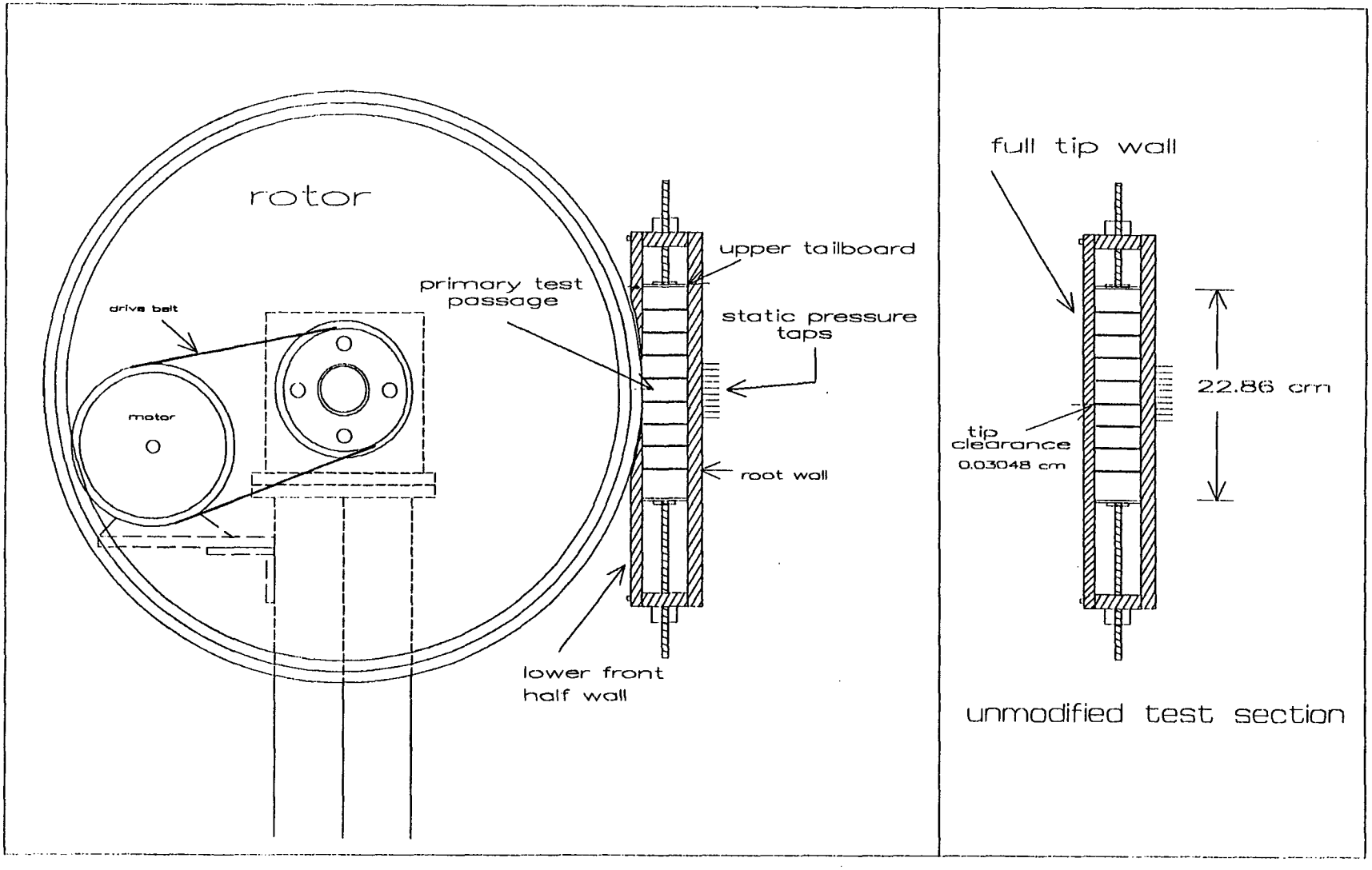

Figure 3.3. Rotor and Test Section Integration (Peter, 1995:7-4)

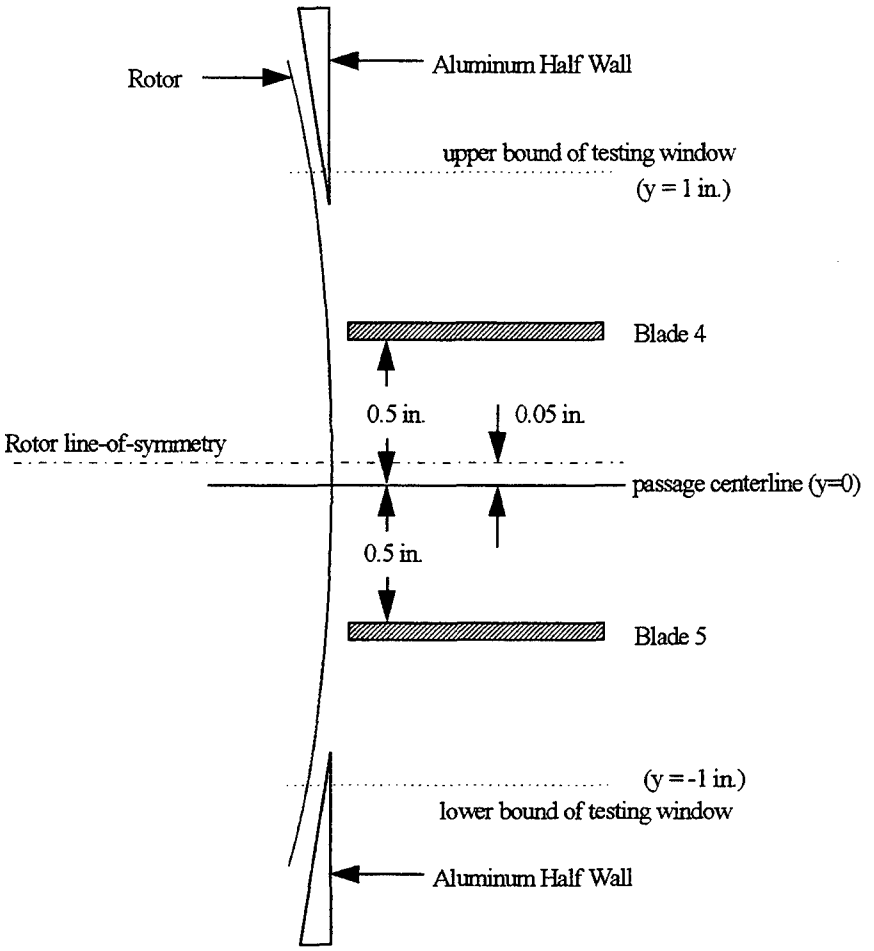

Figure 3.4. Cross-Sectional View of Rotor and Middle Blade Passage

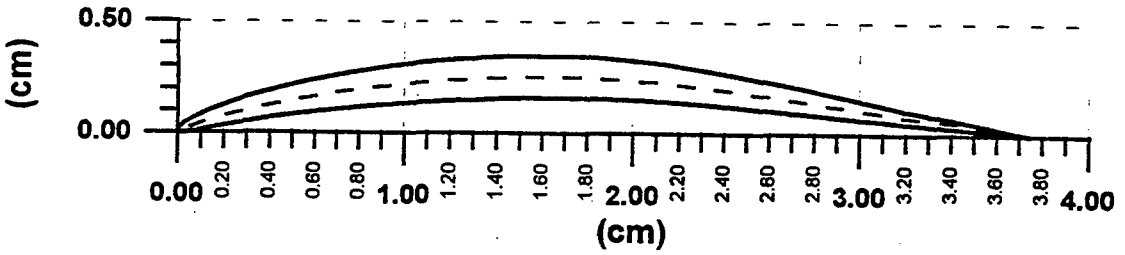

Figure 3.5. Blade Profile NACA 64-A905 (Peter, 1995:7-8)

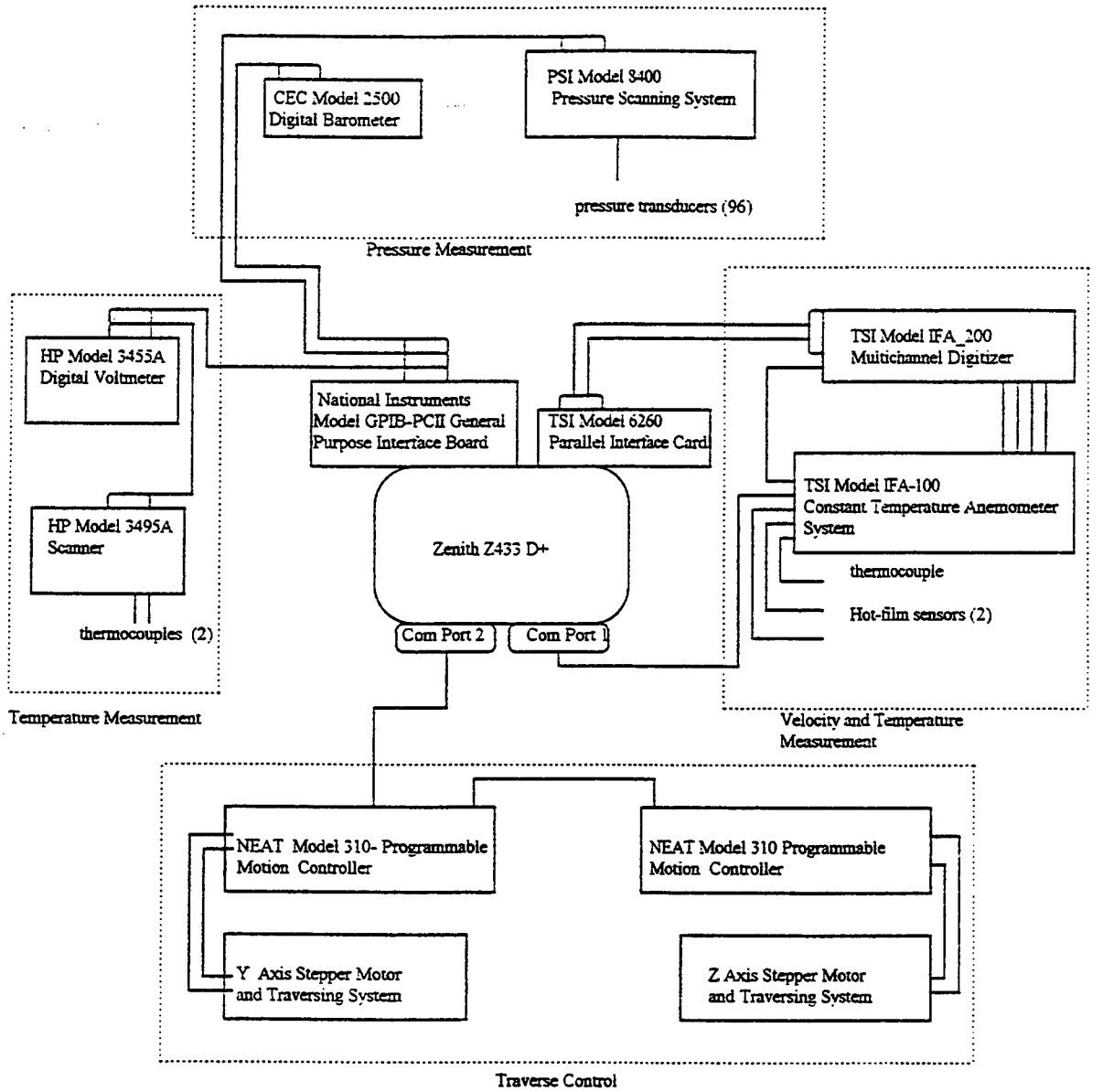

Figure 3.6. AFIT Cascade Wind Tunnel Facility Data Acquisition System (Peter, 1995:7-3)

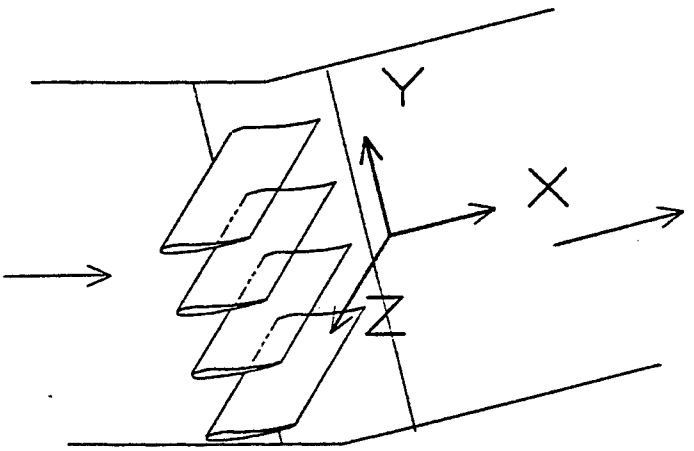

Figure 3.7. Cascade Coordinate System (Peter, 1995:7-5)

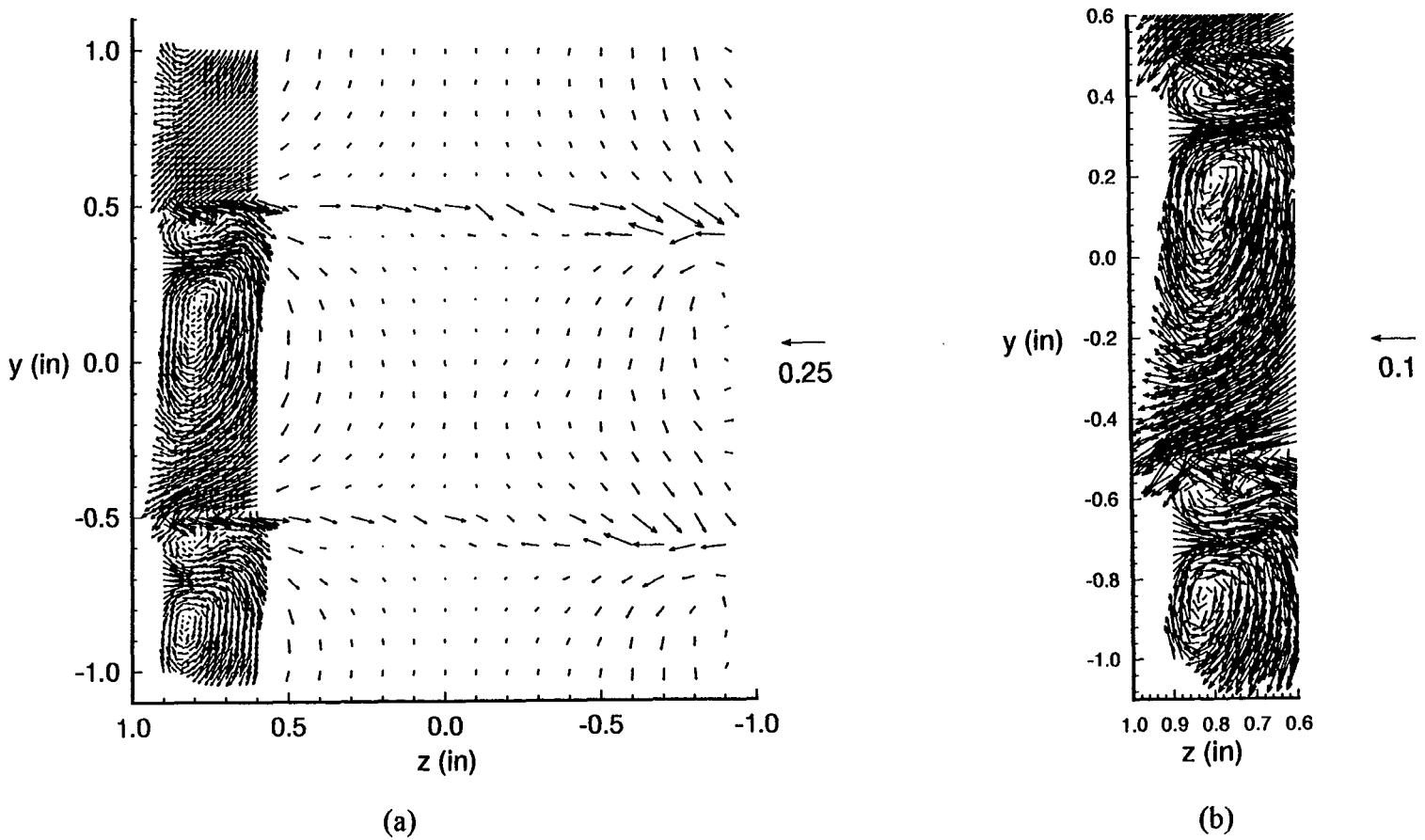

Figure 5.1. Transverse Velocity Vectors for Stationary Endwall
(a) Entire Testing Window and (b) Tip Region of Blades
t/c = 0.008, x/c = 1.0667

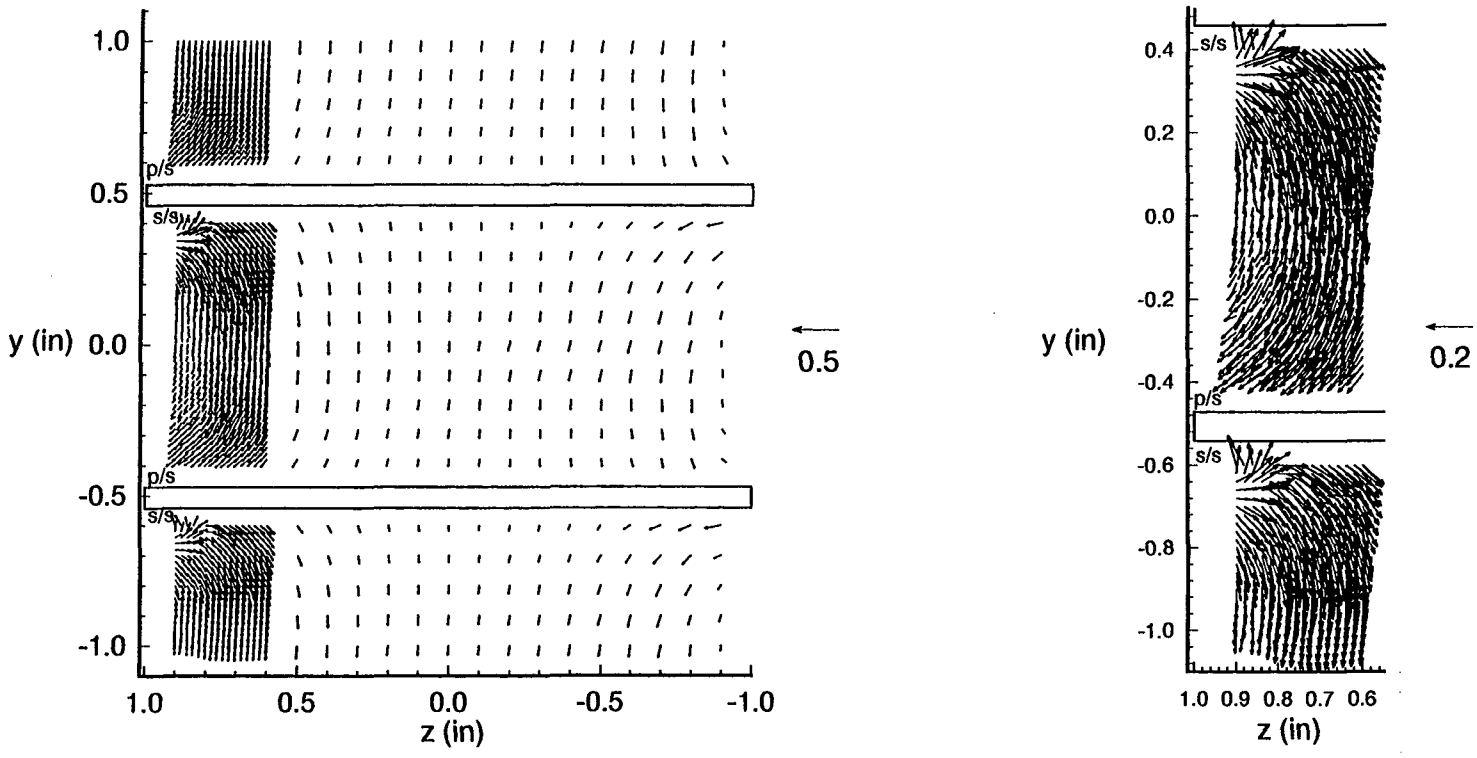

Figure 5.2. Transverse Velocity Vectors for Stationary Endwall
(a) Entire Testing Window and (b) Tip Region of Blades
t/c = 0.008, x/c = 0.5

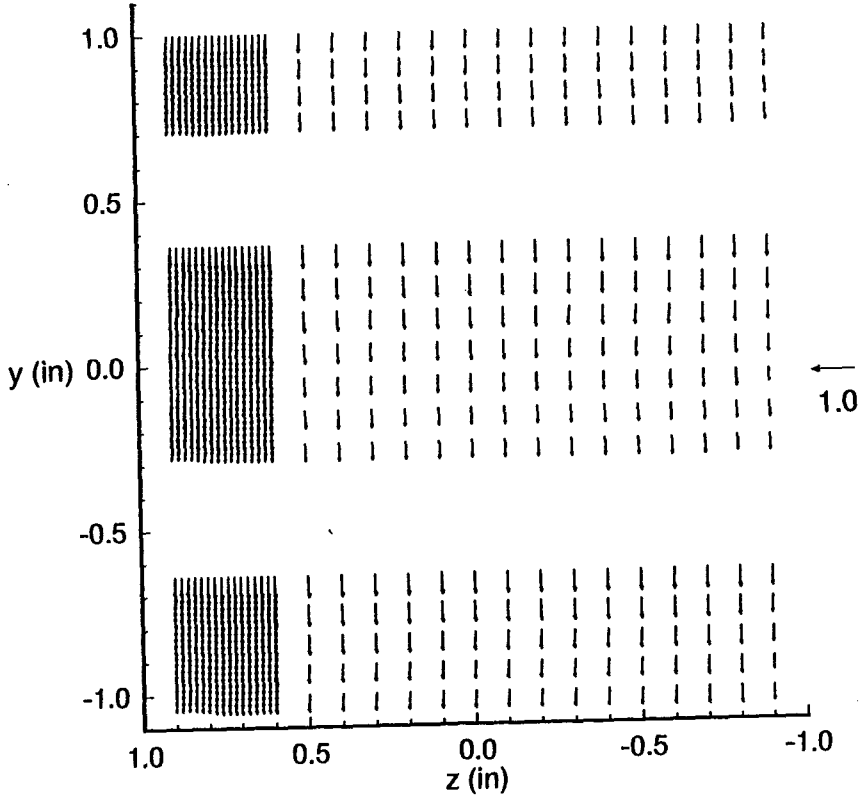

Figure 5.3. Transverse Velocity Vectors
for Stationary Endwall
t/c = 0.008, x/c = -0.0667

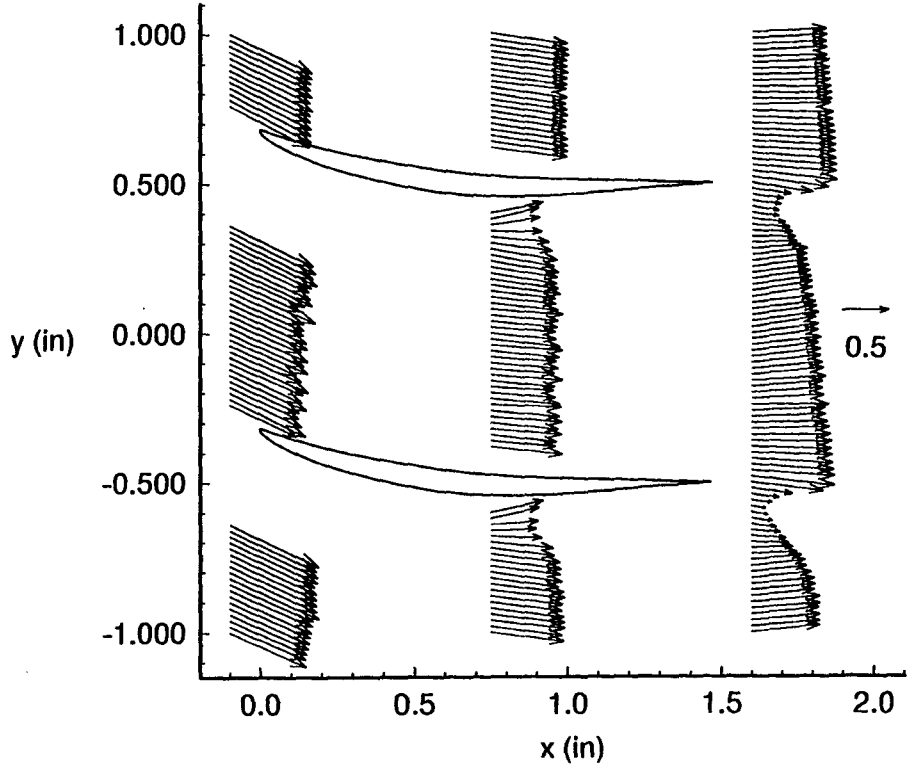

Figure 5.4. Streamwise Velocity Vectors
for Stationary Endwall
t/c = 0.008, z = 0.9 in.

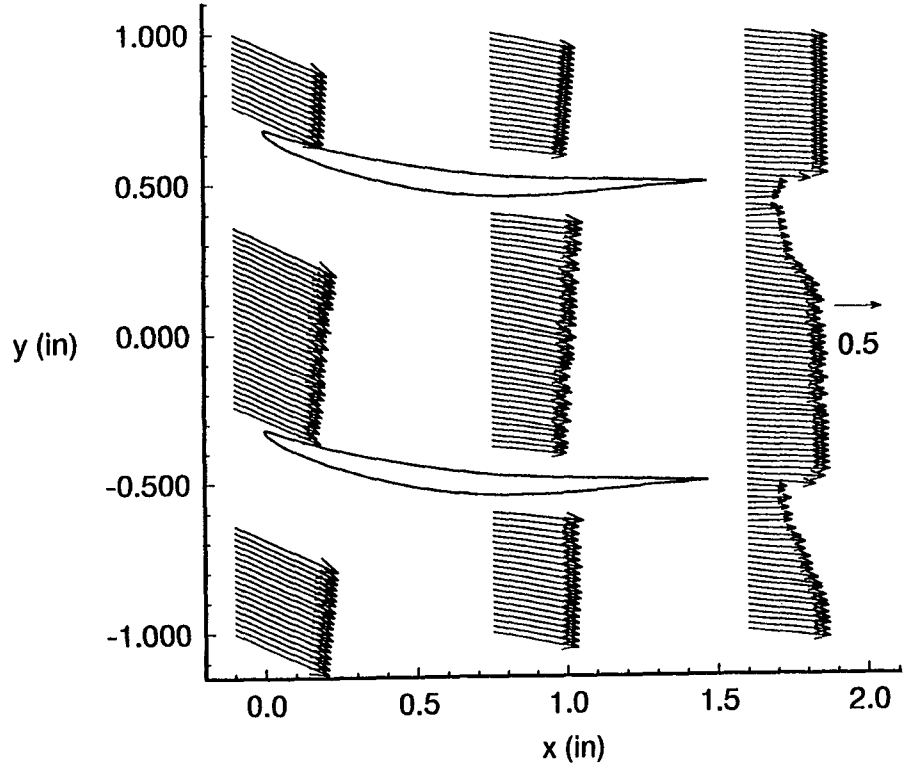

Figure 5.5. Streamwise Velocity Vectors
for Stationary Endwall
t/c = 0.008, z = 0.7 in.

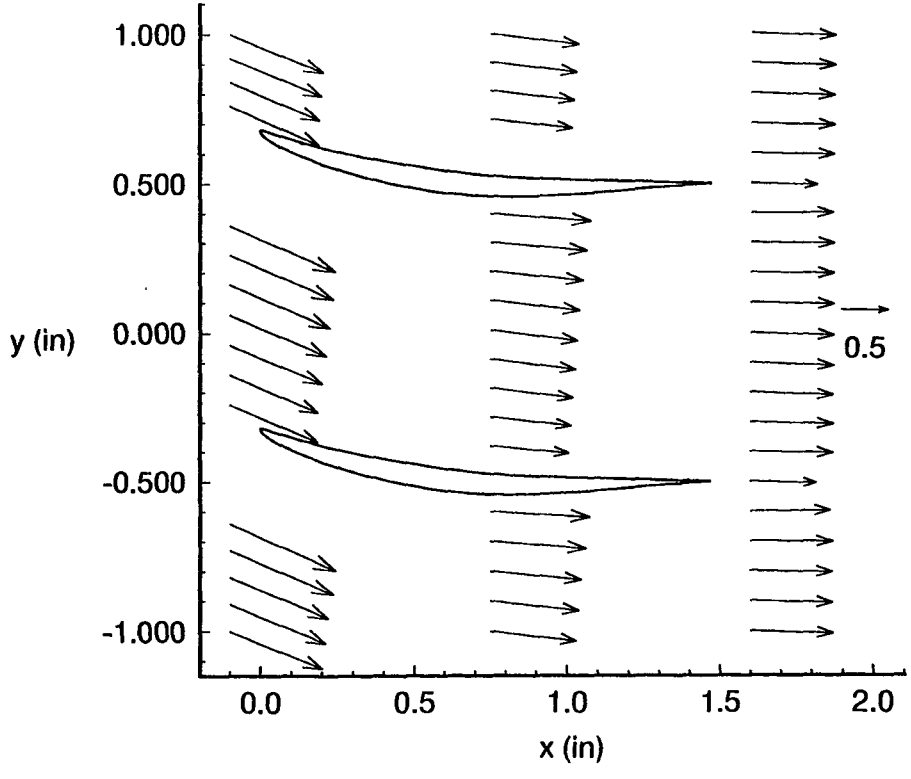

Figure 5.6. Streamwise Velocity Vectors
for Stationary Endwall
t/c = 0.008, z = 0.0

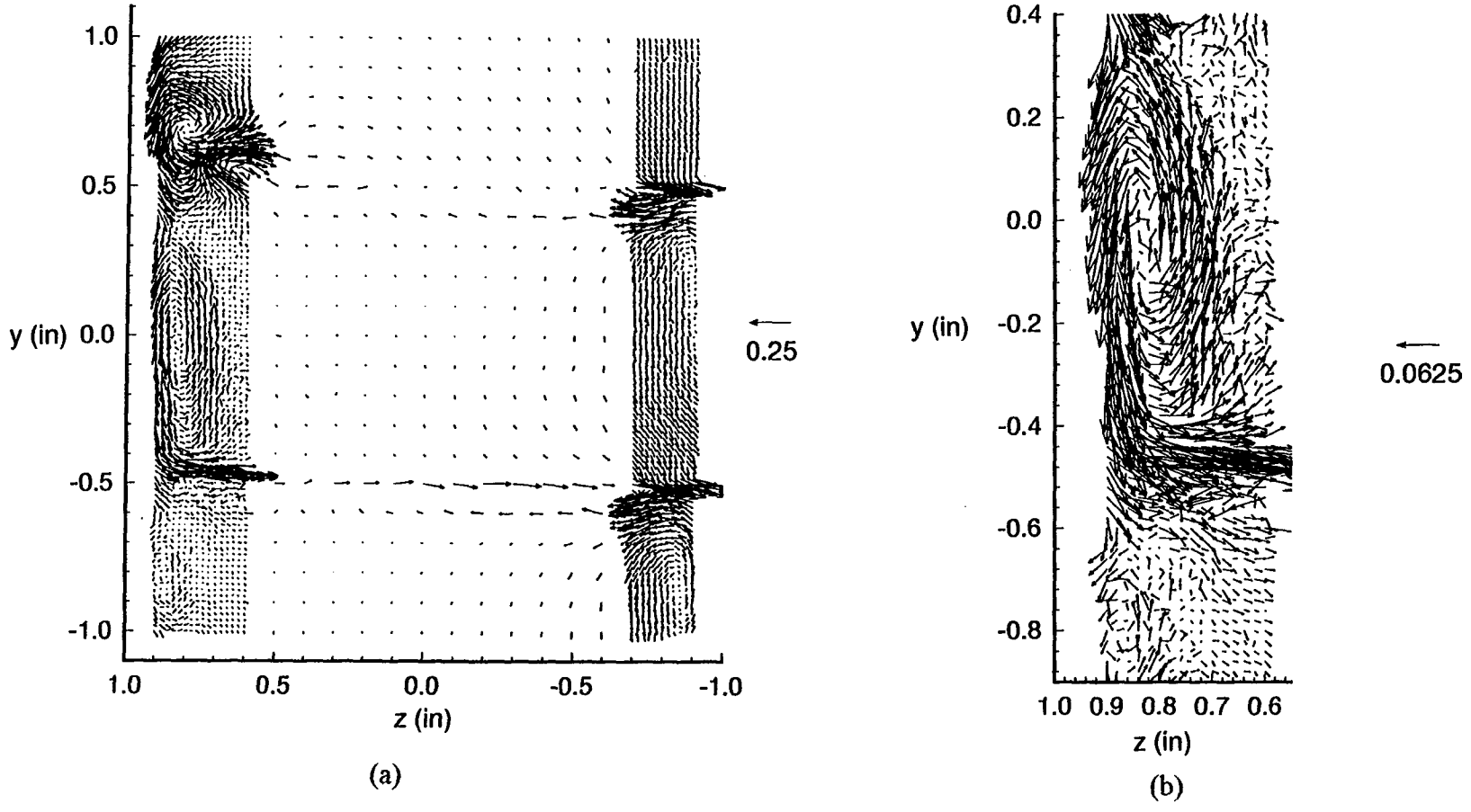

Figure 5.7. Transverse Velocity Vectors for Moving Endwall
(a) Entire Testing Window and (b) Tip Region of Blades
$t/c = 0.02$, $x/c = 1.0677$, $Re_c = 8.68 \times 10^4$

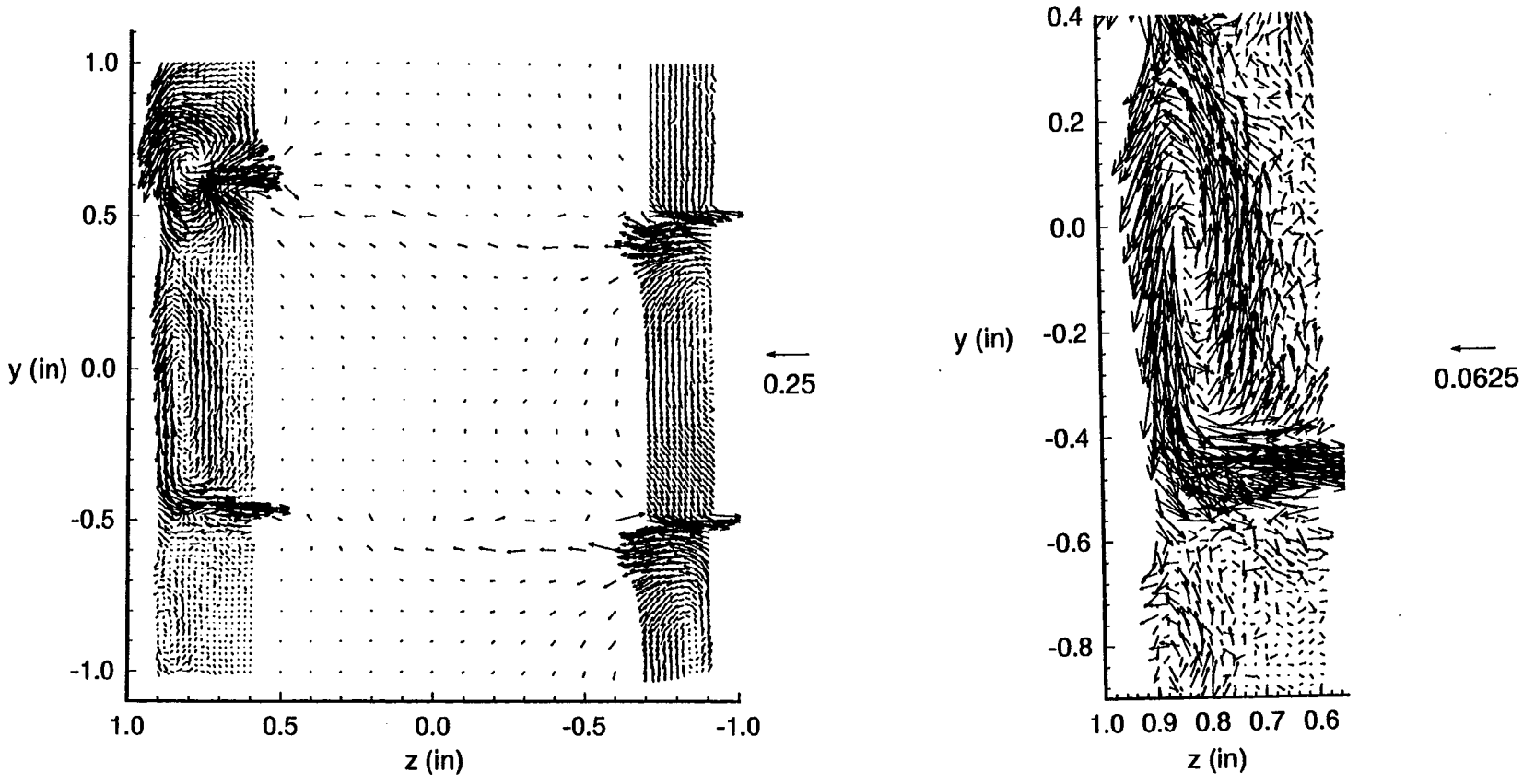

Figure 5.8. Transverse Velocity Vectors for Moving Endwall
(a) Entire Testing Window and (b) Tip Region of Blades
$t/c = 0.02$, $x/c = 1.0677$, $Re_c = 9.72 \times 10^4$

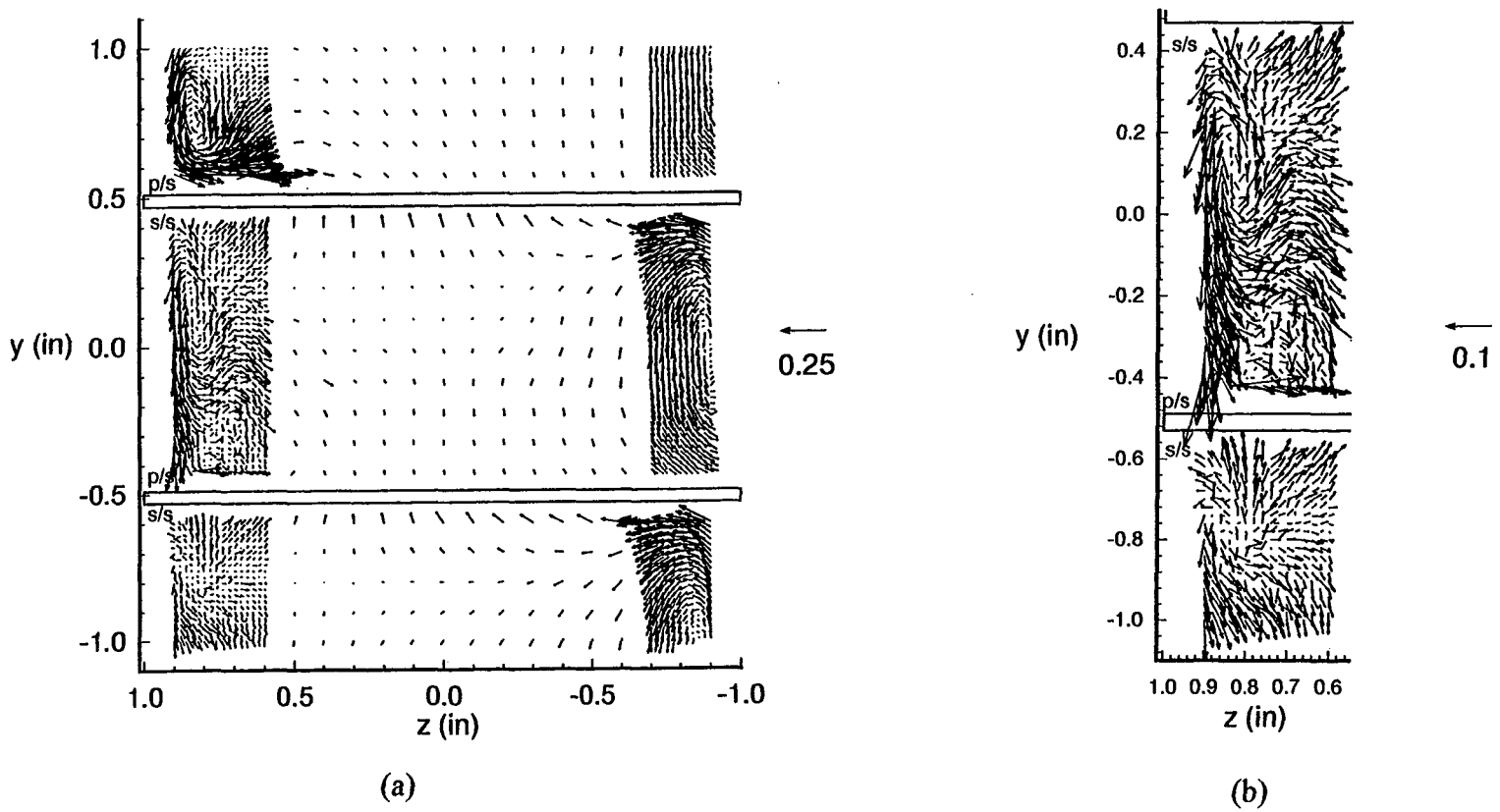

Figure 5.9. Transverse Velocity Vectors for Moving Endwall
(a) Entire Testing Window and (b) Tip Region of Blades
$t/c = 0.02$, $x/c = 0.75$, $Re_c = 9.72 \times 10^4$

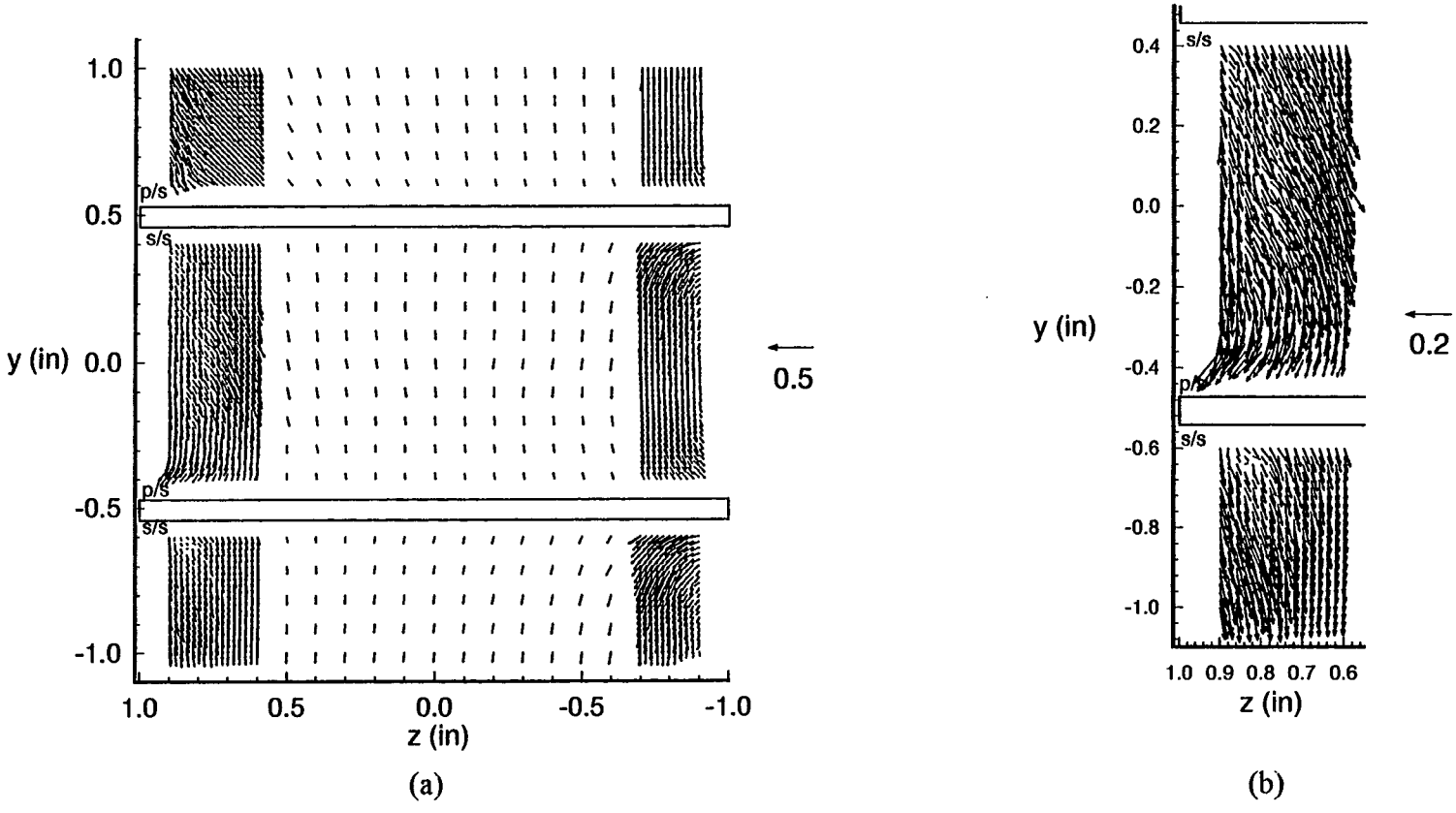

Figure 5.10. Transverse Velocity Vectors for Moving Endwall
(a) Entire Testing Window and (b) Tip Region of Blades
$t/c = 0.02$, $x/c = 0.5$, $Re_c = 9.72 \times 10^4$

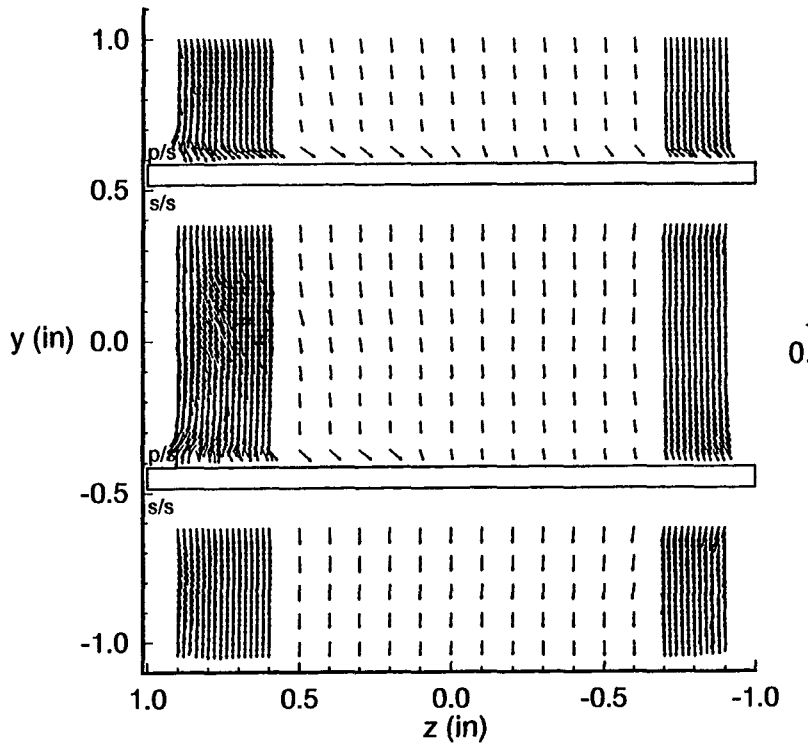

Figure 5.11. Transverse Velocity Vectors
for Moving Endwall
t/c = 0.02, x/c = 0.25, $Re_c = 9.72 \times 10^4$

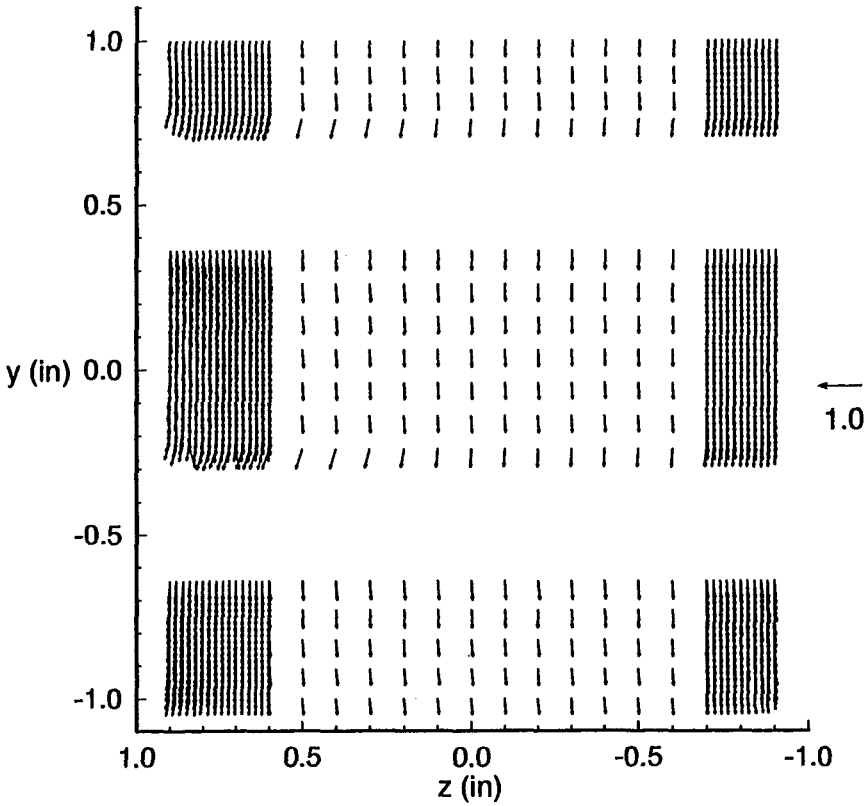

Figure 5.12. Transverse Velocity Vectors
for Moving Endwall
t/c = 0.02, x/c = -0.0667, $Re_c = 9.72 \times 10^4$

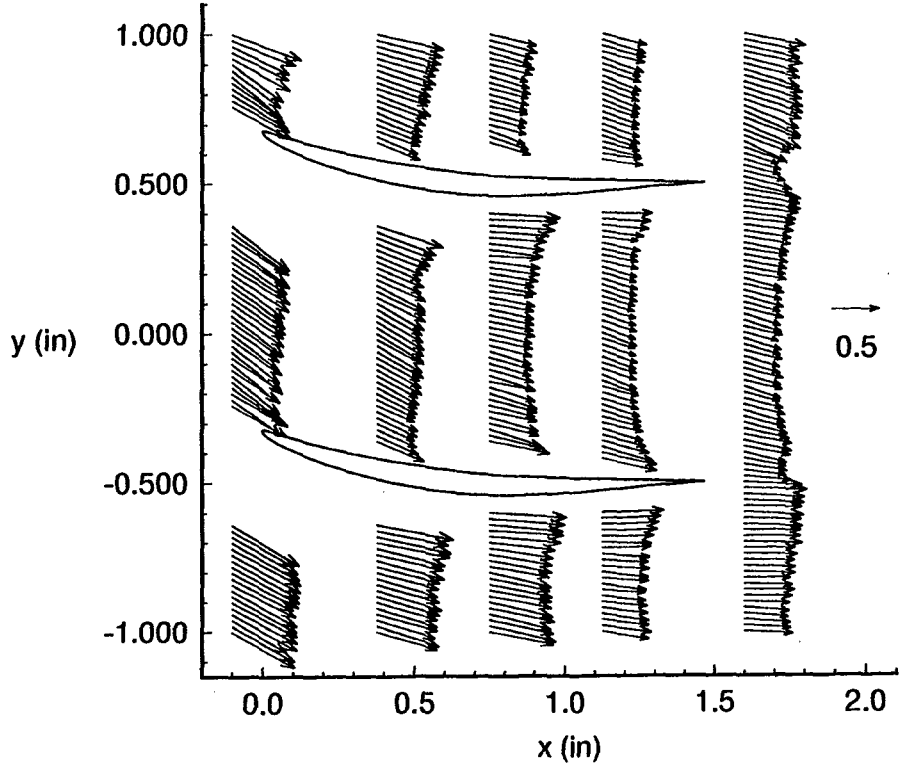

Figure 5.13. Streamwise Velocity Vectors
for Moving Endwall
t/c = 0.02, z = 0.9 in., $Re_c = 9.72 \times 10^4$

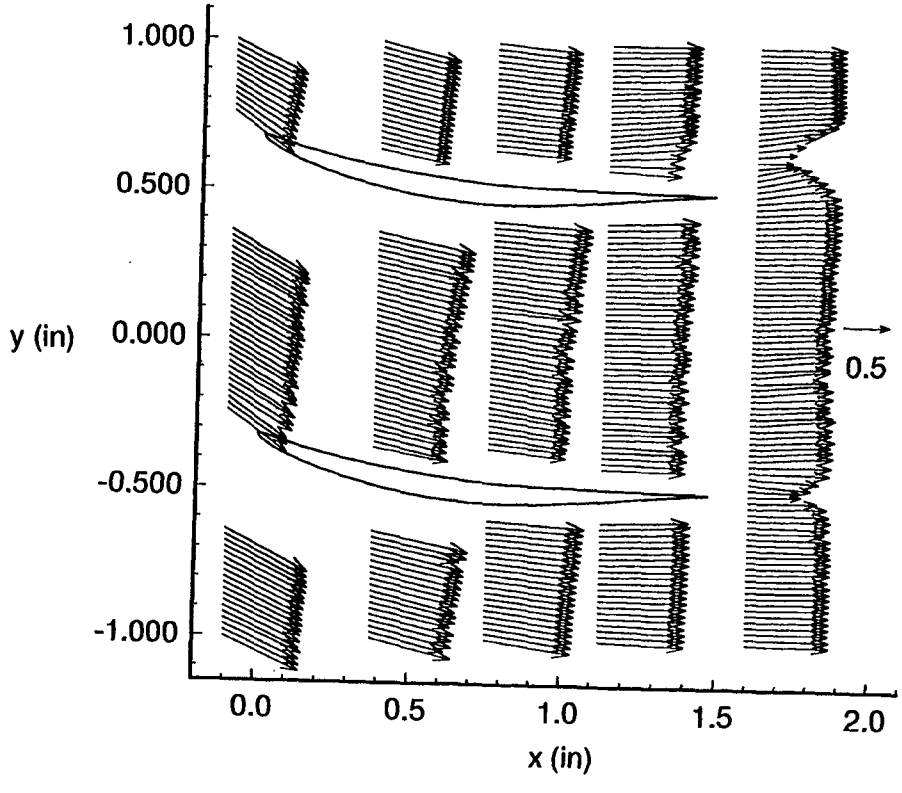

Figure 5.14. Streamwise Velocity Vectors
for Moving Endwall
t/c = 0.02, z = 0.7 in., $Re_c = 9.72 \times 10^4$

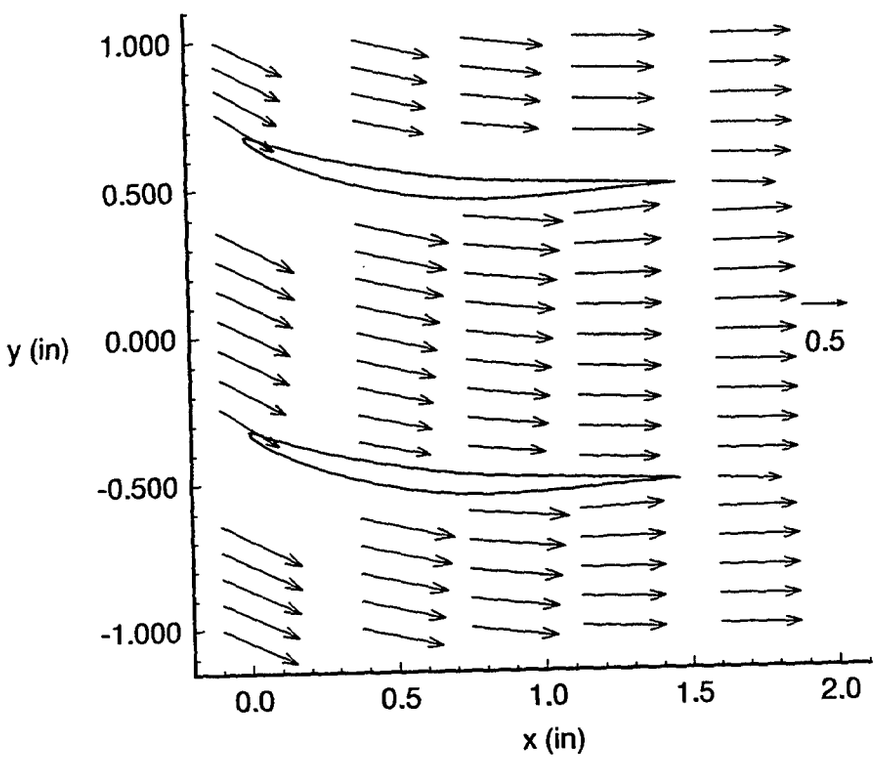

Figure 5.15. Streamwise Velocity Vectors for Moving Endwall
$t/c = 0.02$, $z = 0.0$, $Re_c = 9.72 \times 10^4$

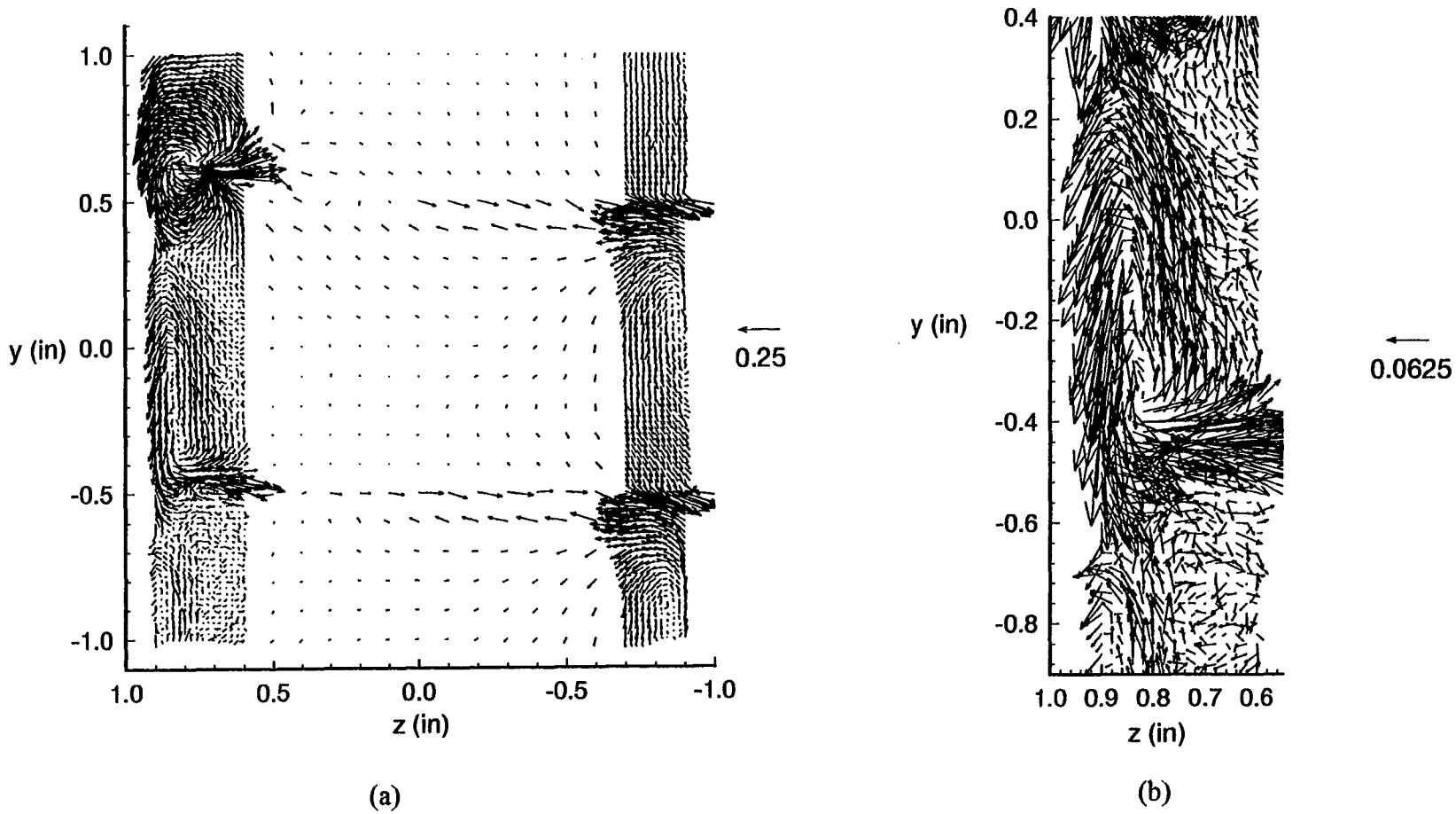

Figure 5.16. Transverse Velocity Vectors for Moving Endwall
(a) Entire Testing Window and (b) Tip Region of Blades
$t/c = 0.01$, $x/c = 1.0677$, $Re_c = 9.72 \times 10^4$

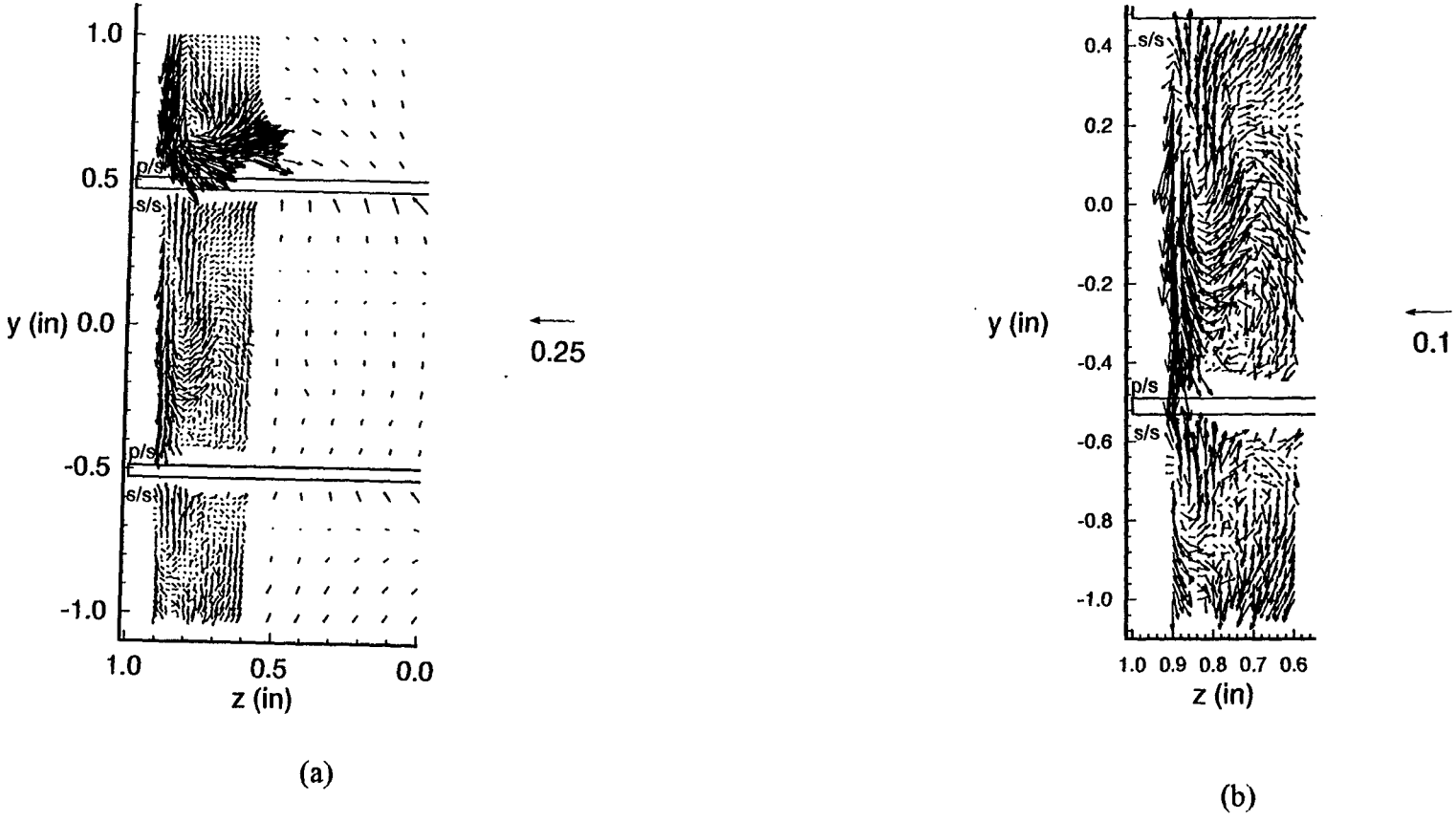

Figure 5.17. Transverse Velocity Vectors for Moving Endwall
(a) Left Half of Testing Window and (b) Tip Region of Blades
$t/c = 0.01$, $x/c = 0.75$, $Re_c = 9.72 \times 10^4$

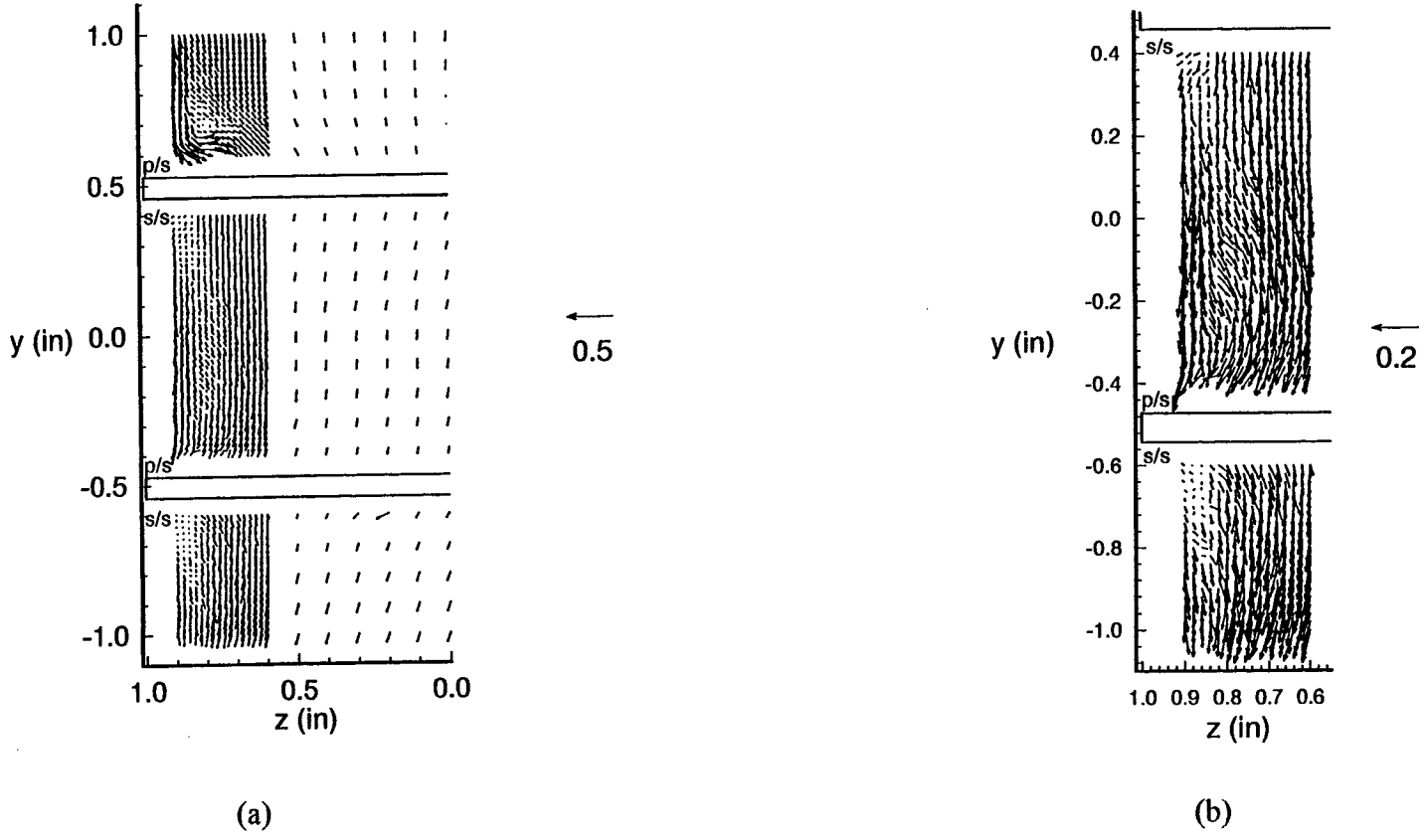

Figure 5.18. Transverse Velocity Vectors for Moving Endwall
(a) Left Half of Testing Window and (b) Tip Region of Blades
$t/c = 0.01$, $x/c = 0.5$, $Re_c = 9.72 \times 10^4$

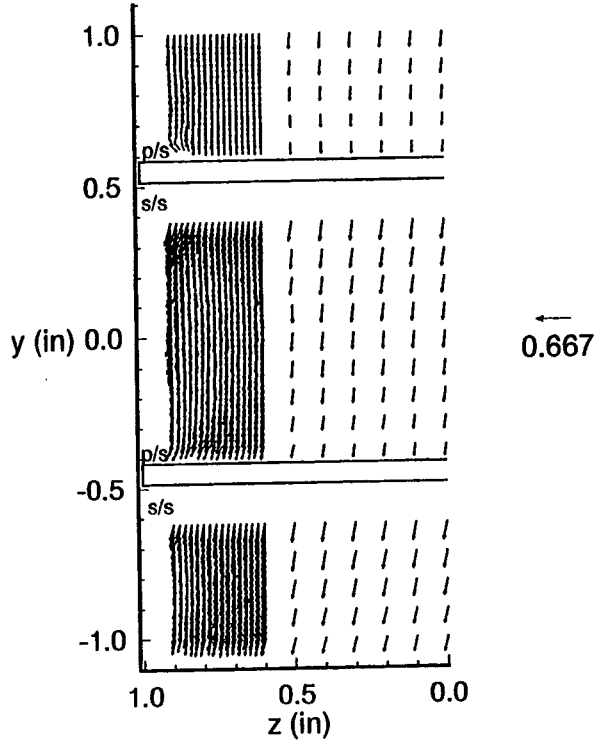

Figure 5.19. Transverse Velocity Vectors
for Moving Endwall
$t/c = 0.01$, $x/c = 0.25$, $Re_c = 9.72 \times 10^4$

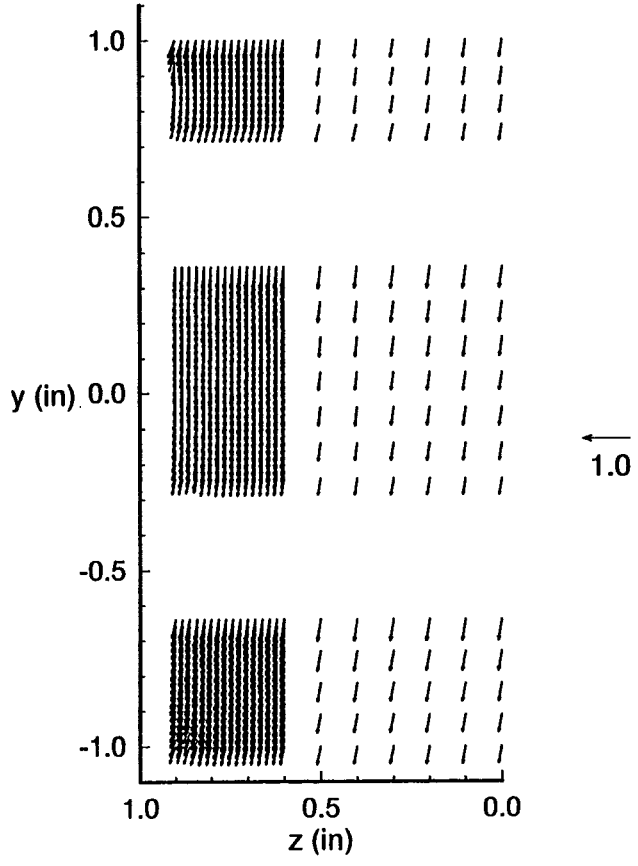

Figure 5.20. Transverse Velocity Vectors
for Moving Endwall
$t/c = 0.01$, $x/c = -0.0667$, $Re_c = 9.72 \times 10^4$

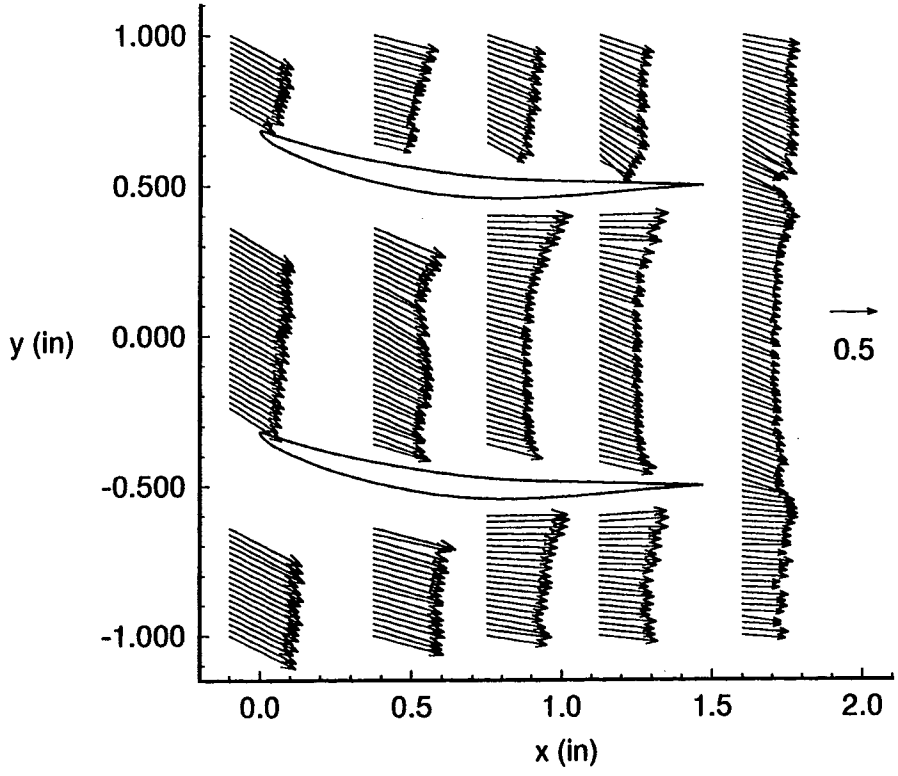

Figure 5.21. Streamwise Velocity Vectors
for Moving Endwall
t/c = 0.01, z = 0.9 in., $Re_c = 9.72 \times 10^4$

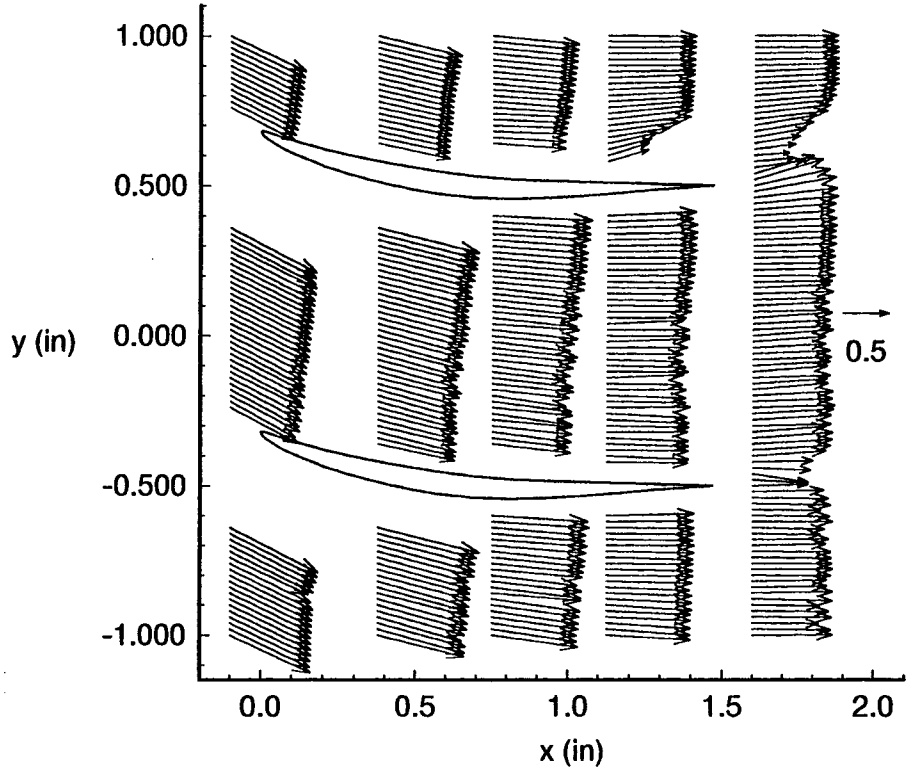

Figure 5.22. Streamwise Velocity Vectors
for Moving Endwall
t/c = 0.01, z = 0.7 in., $Re_c = 9.72 \times 10^4$

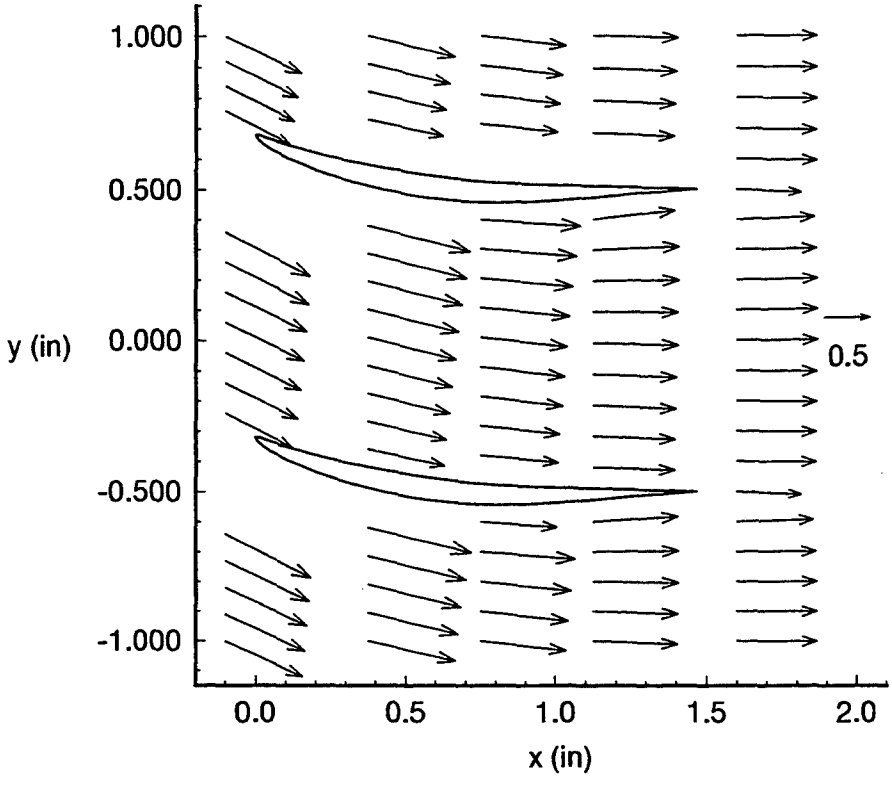

Figure 5.23. Streamwise Velocity Vectors for Moving Endwall
$t/c = 0.01$, $z = 0.0$, $Re_c = 9.72 \times 10^4$

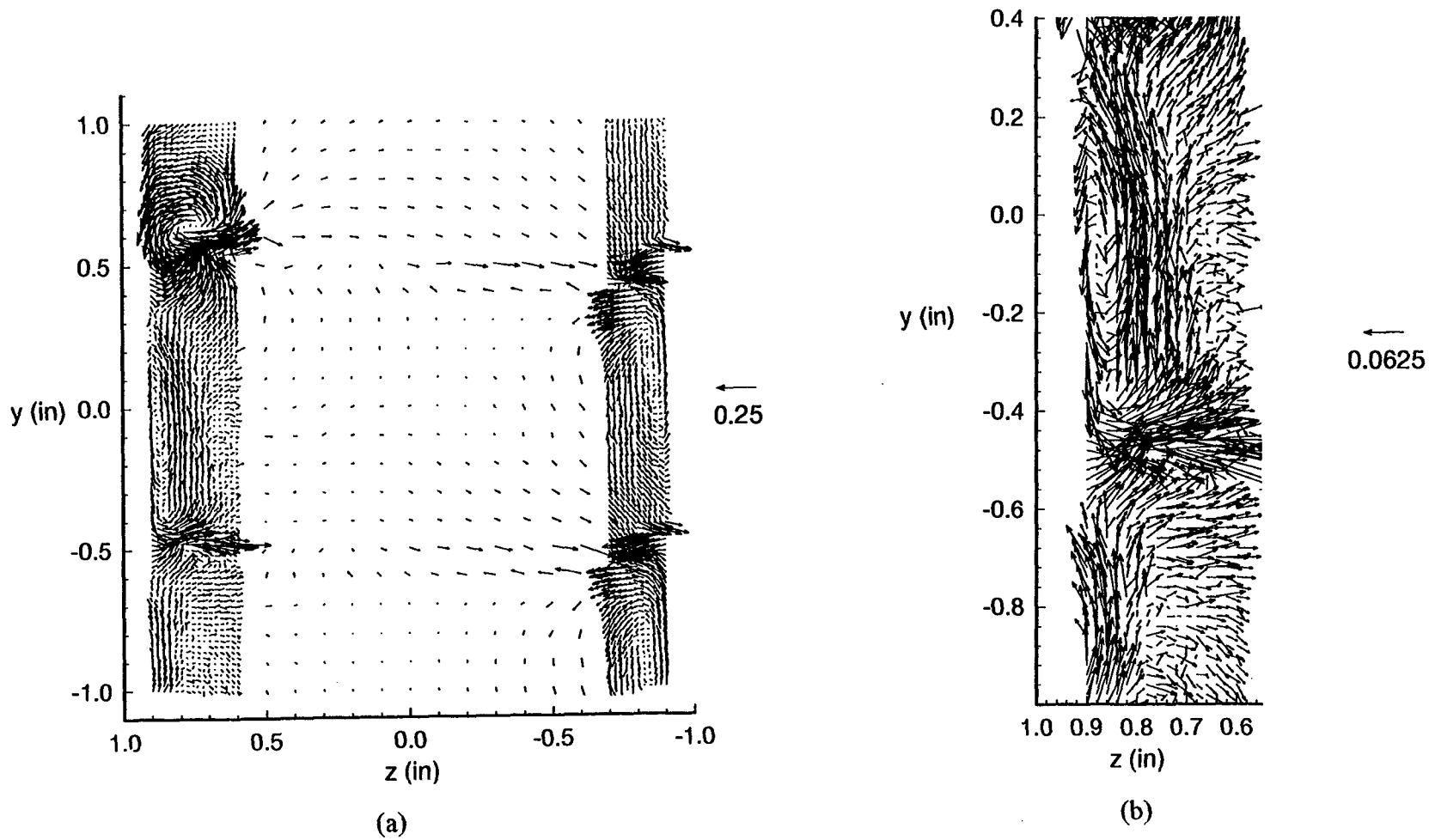

Figure 5.24. Transverse Velocity Vectors for Moving Endwall
(a) Entire Testing Window and (b) Tip Region of Blades
$t/c = 0.005$, $x/c = 1.0677$, $Re_c = 9.72 \times 10^4$

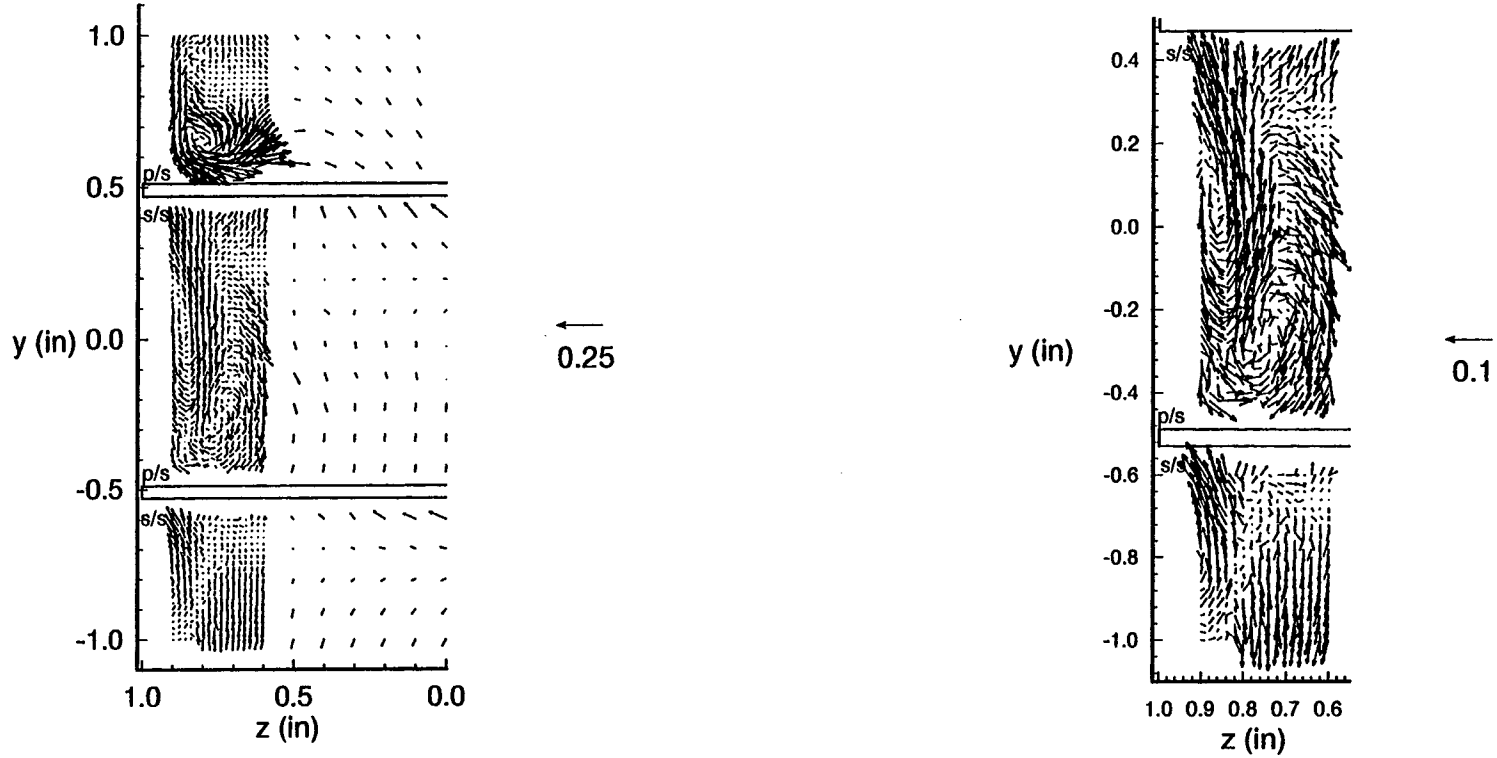

Figure 5.25. Transverse Velocity Vectors for Moving Endwall
(a) Left Half of Testing Window and (b) Tip Region of Blades
$t/c = 0.005$, $x/c = 0.75$, $Re_c = 9.72 \times 10^4$

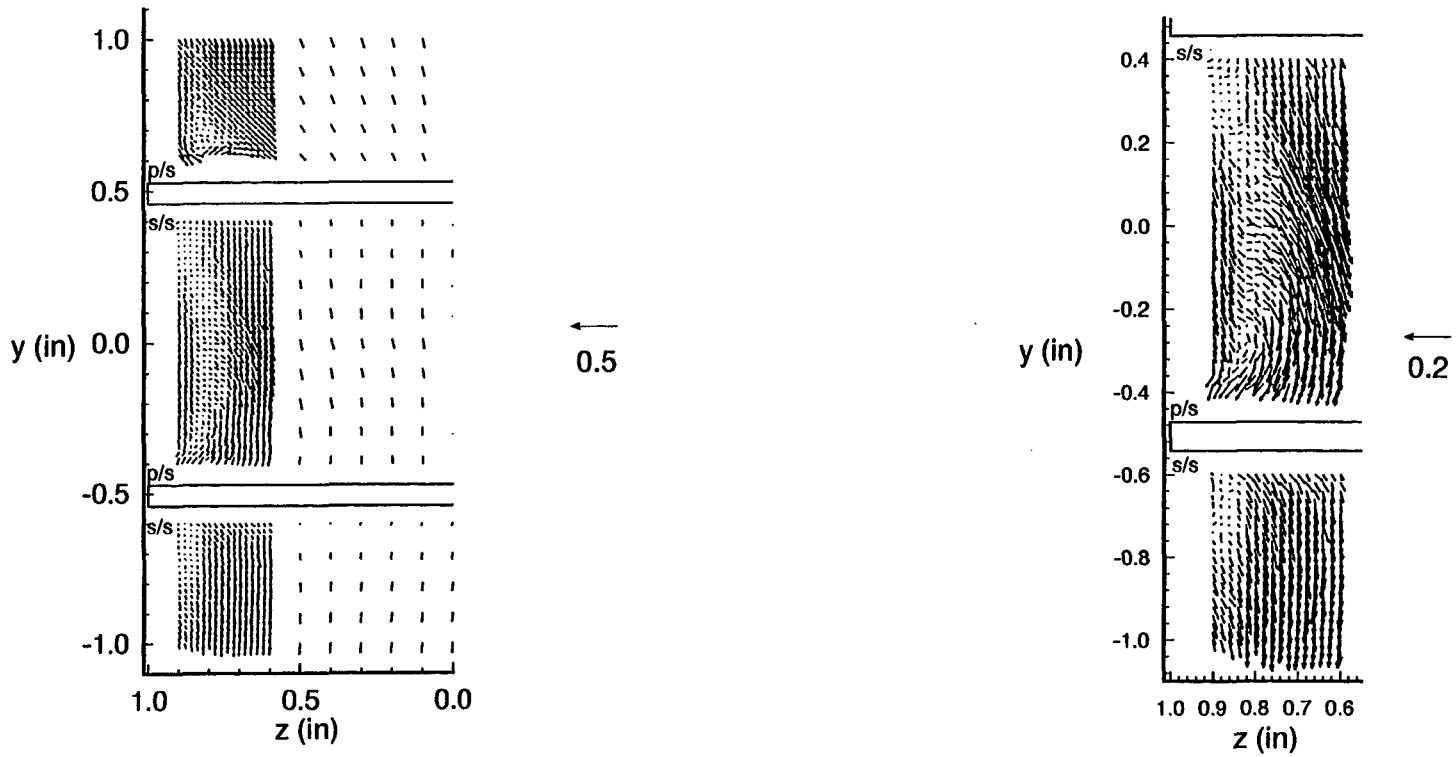

Figure 5.26. Transverse Velocity Vectors for Moving Endwall
(a) Left Half of Testing Window and (b) Tip Region of Blades
$t/c = 0.005$, $x/c = 0.5$, $Re_c = 9.72 \times 10^4$

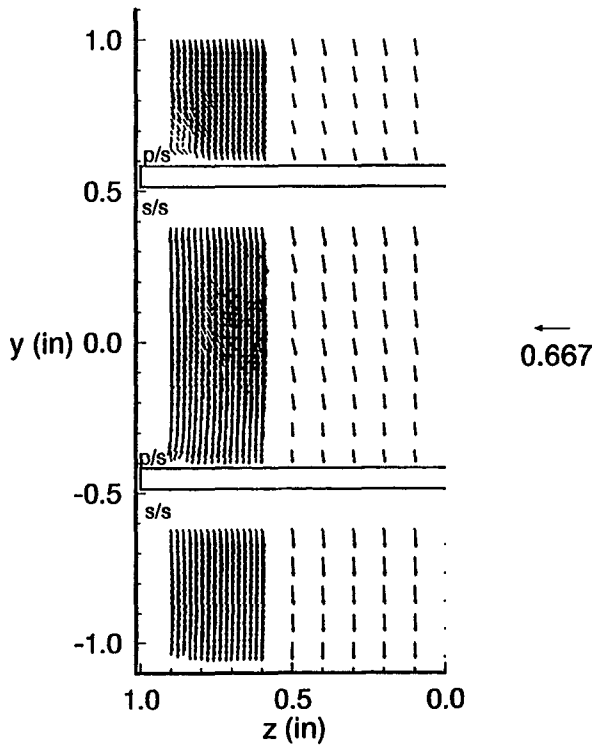

Figure 5.27. Transverse Velocity Vectors
for Moving Endwall
$t/c = 0.005$, $x/c = 0.25$, $Re_c = 9.72 \times 10^4$

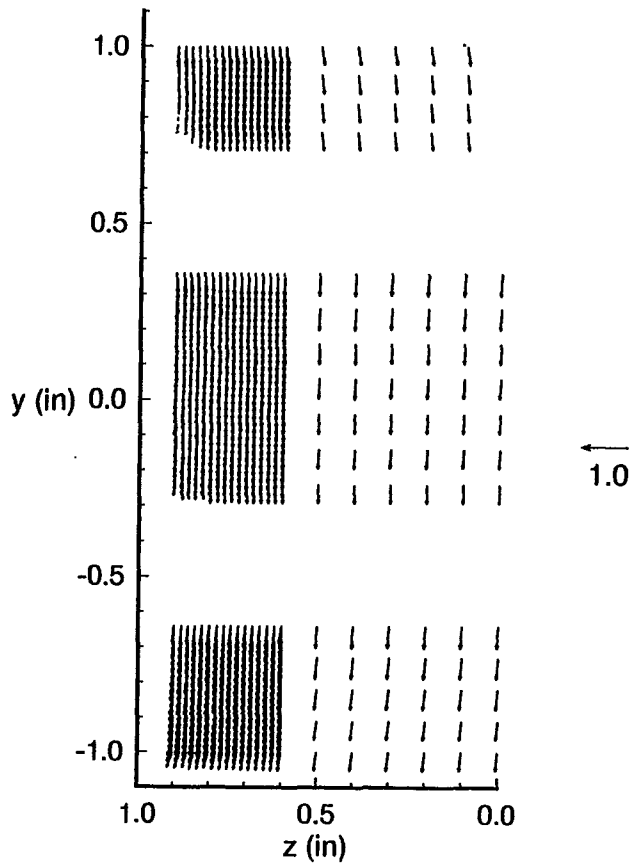

Figure 5.28. Transverse Velocity Vectors
for Moving Endwall
$t/c = 0.005$, $x/c = -0.0667$, $Re_c = 9.72 \times 10^4$

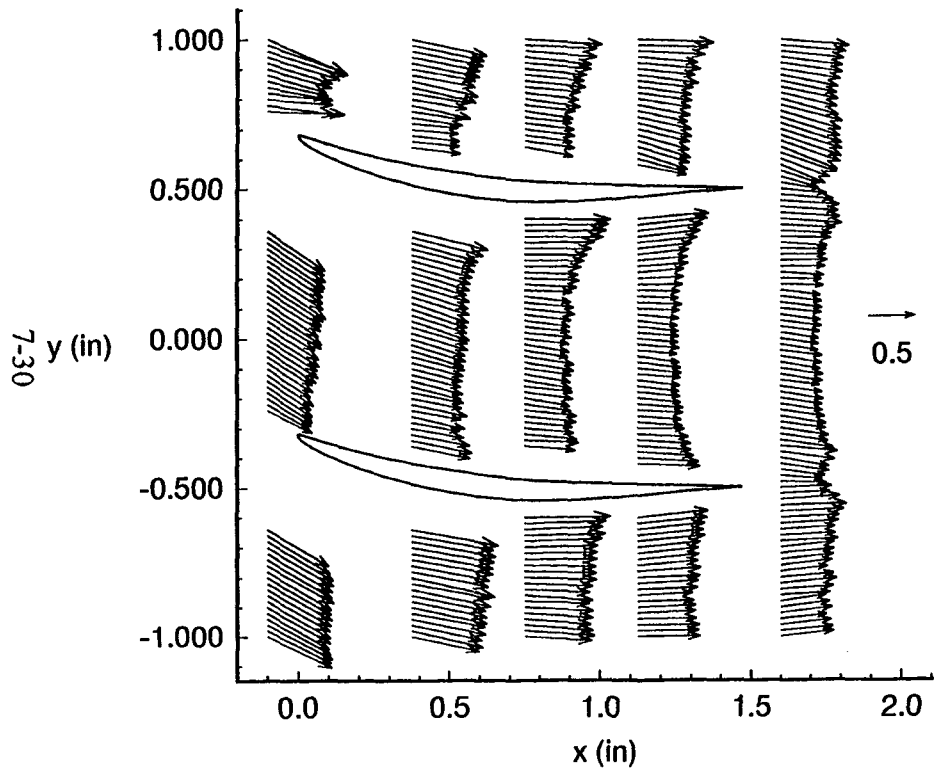

Figure 5.29. Streamwise Velocity Vectors
for Moving Endwall
t/c = 0.005, z = 0.9 in., $Re_c = 9.72 \times 10^4$

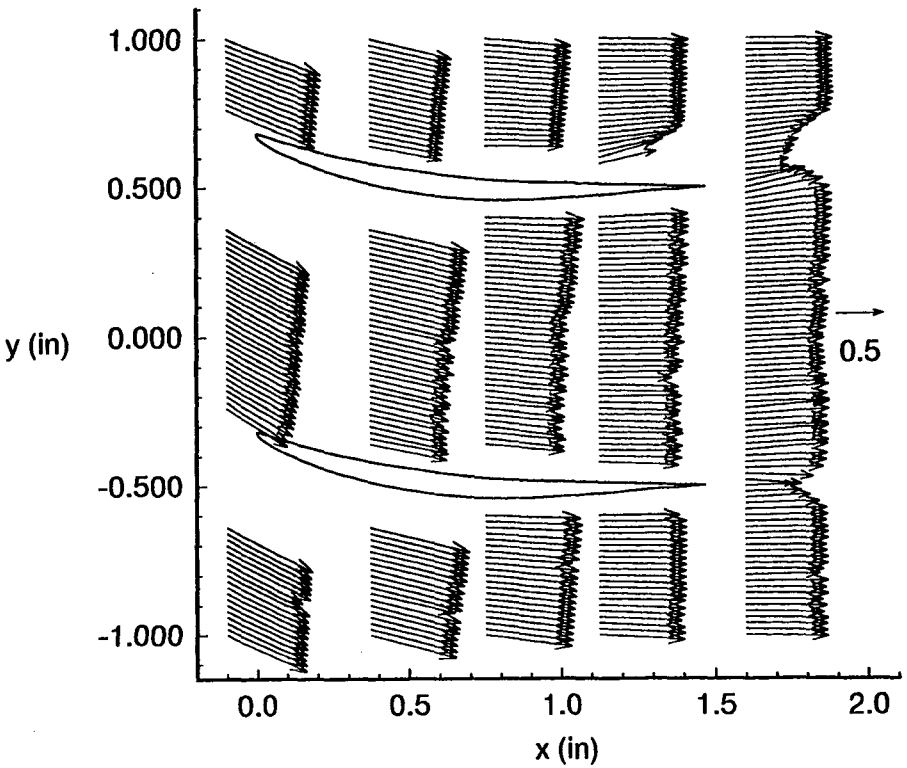

Figure 5.30. Streamwise Velocity Vectors
for Moving Endwall
t/c = 0.005, z = 0.7 in., $Re_c = 9.72 \times 10^4$

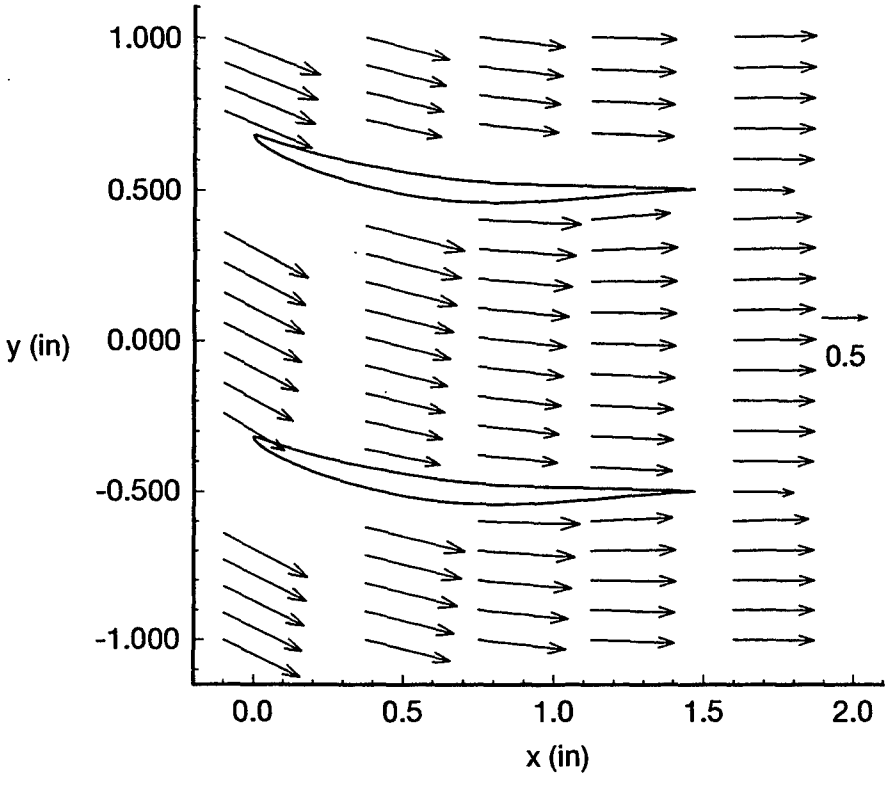

Figure 5.31. Streamwise Velocity Vectors for Moving Endwall
t/c = 0.005, z = 0.0, $Re_c = 9.72 \times 10^4$

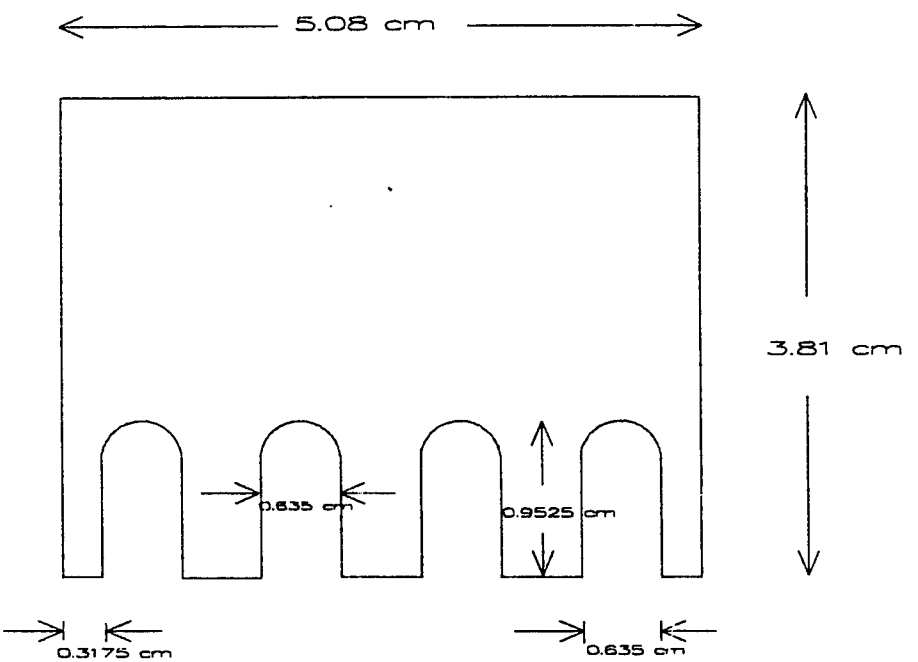

Figure 5.32. Crenulated Blade (Peter, 1995:7-35)

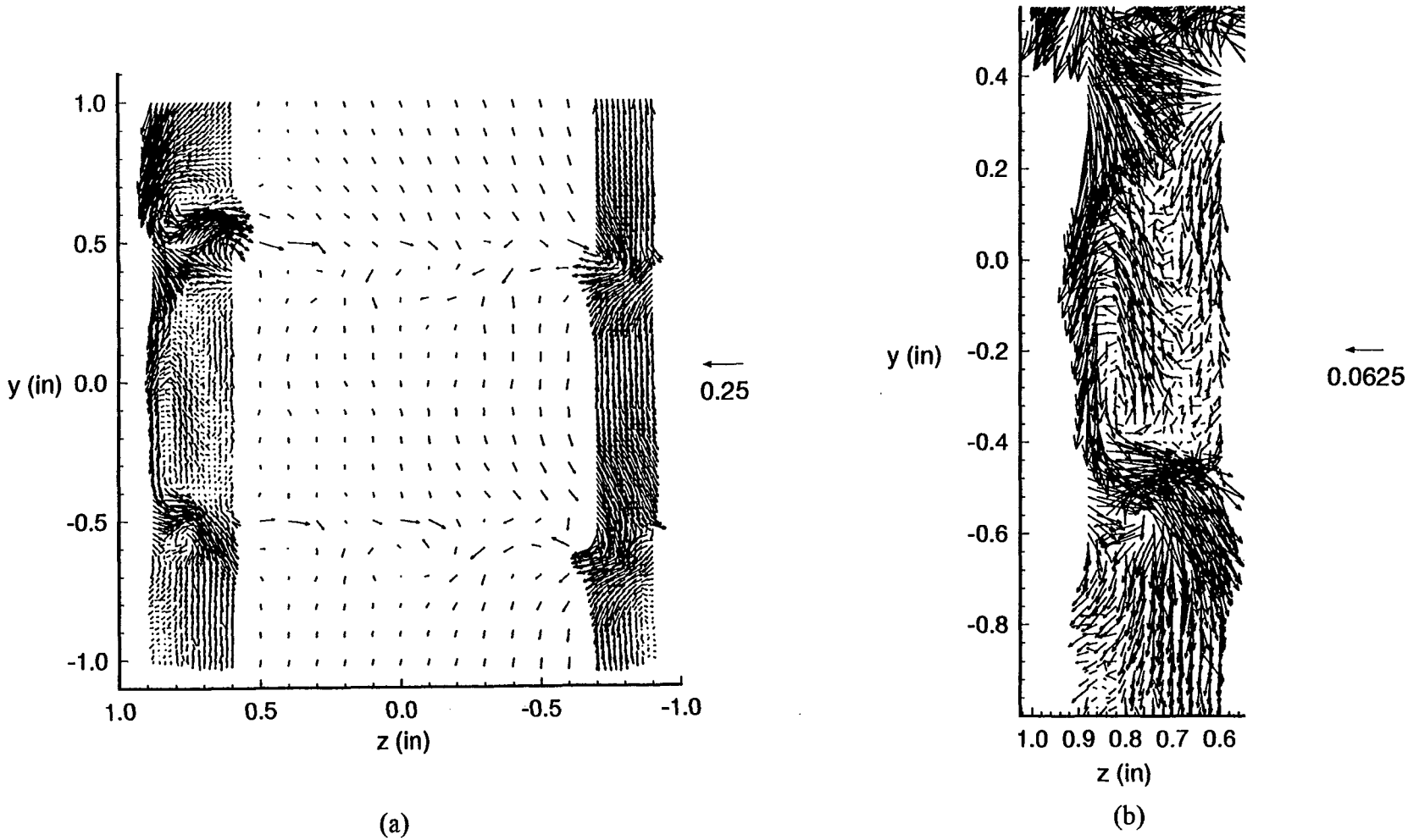

Figure 5.33. Transverse Velocity Vectors for Moving Endwall (Crenulated Blades)
(a) Entire Testing Window and (b) Tip Region of Blades
$t/c = 0.01$, $x/c = 1.0677$, $Re_c = 9.72 \times 10^4$

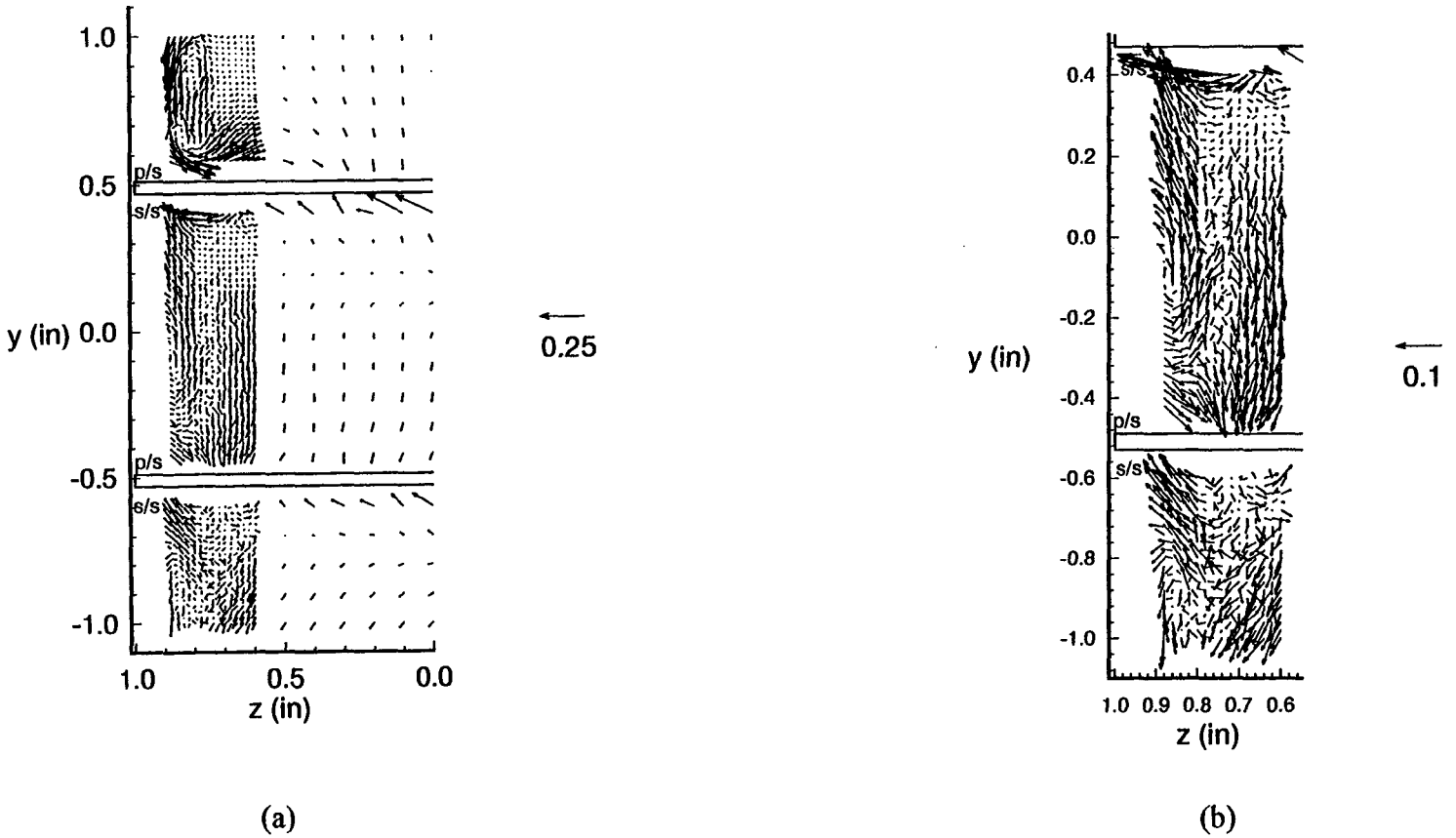

Figure 5.34. Transverse Velocity Vectors for Moving Endwall (Crenulated Blades)
(a) Left Half of Testing Window and (b) Tip Region of Blades
$t/c = 0.01$, $x/c = 0.75$, $Re_c = 9.72 \times 10^4$

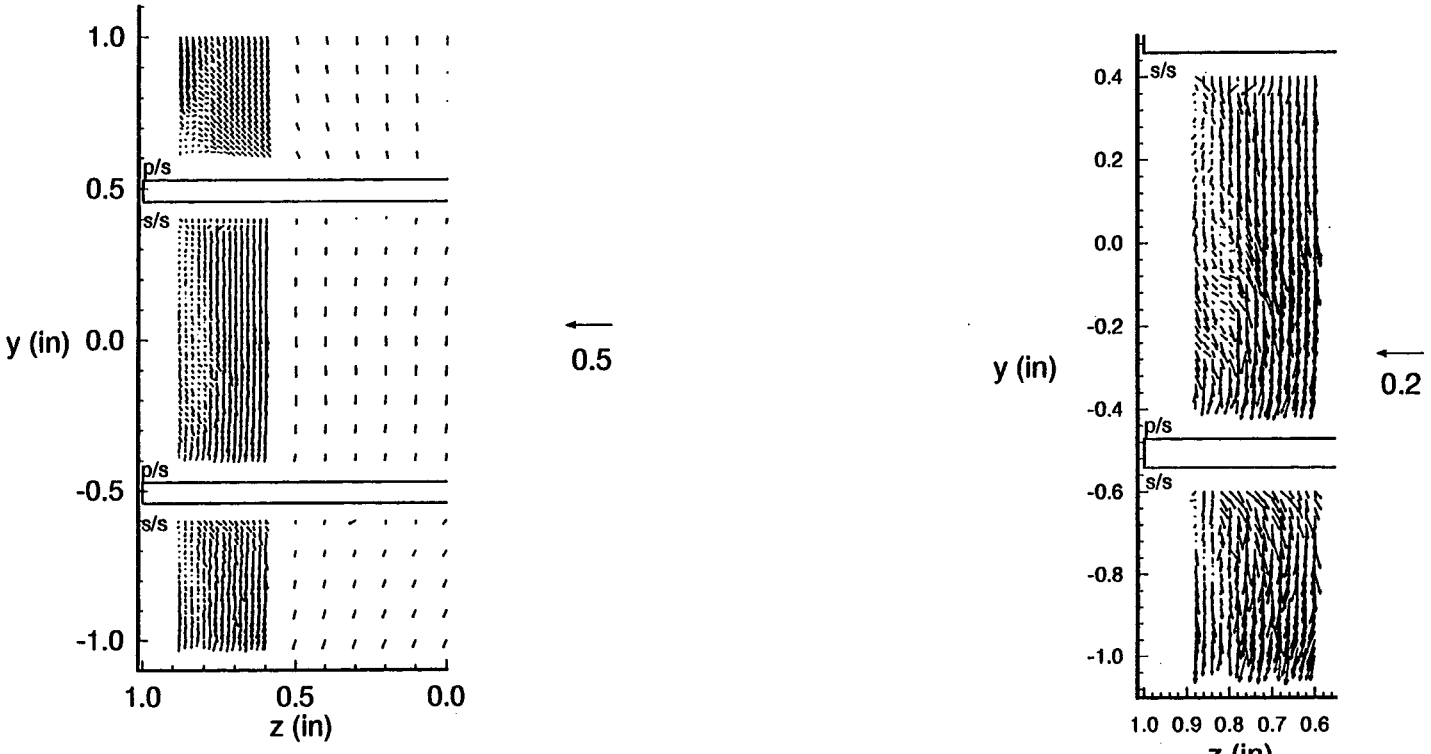

Figure 5.35. Transverse Velocity Vectors for Moving Endwall (Crenulated Blades)
(a) Left Half of Testing Window and (b) Tip Region of Blades
$t/c = 0.01$, $x/c = 0.5$, $Re_c = 9.72 \times 10^4$

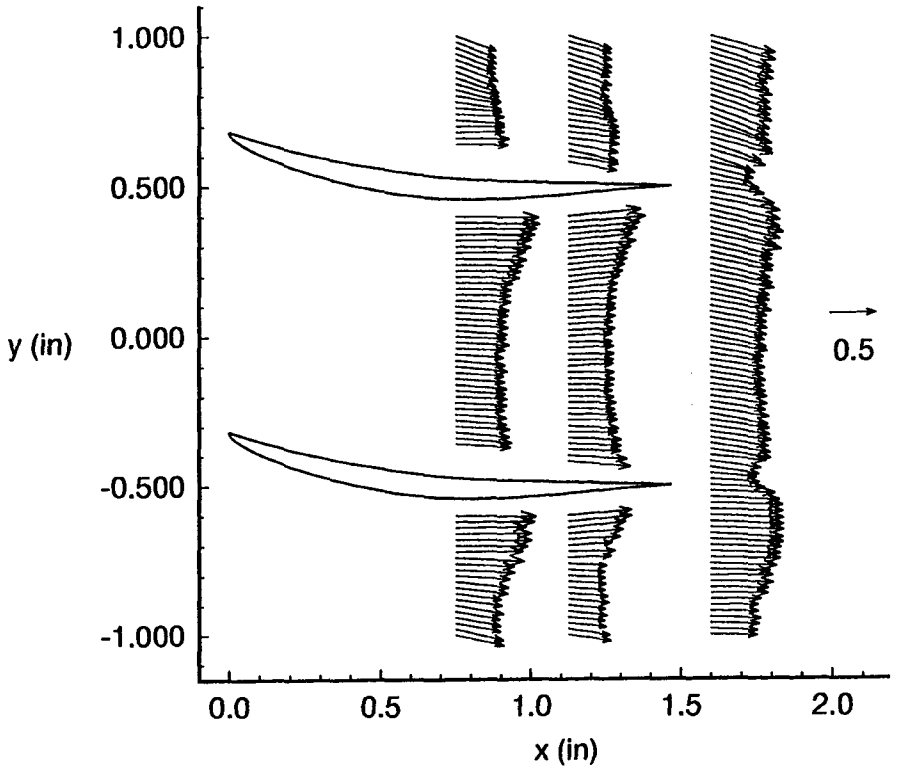

Figure 5.36. Streamwise Velocity Vectors
for Moving Endwall (Crenulated Blades)
t/c = 0.01, z = 0.9 in., $Re_c = 9.72 \times 10^4$

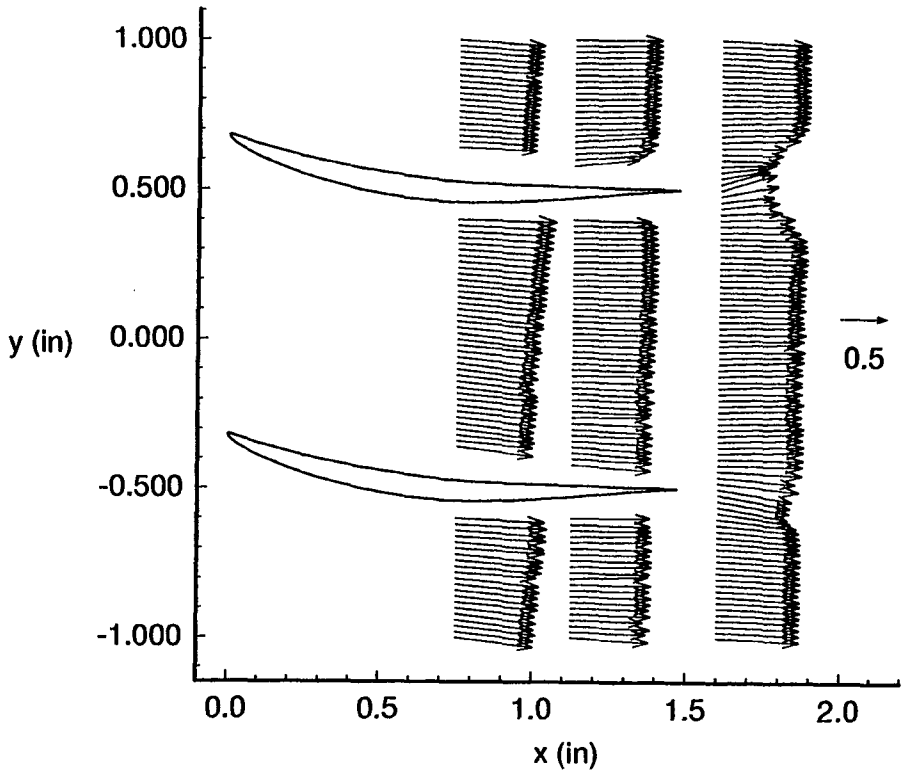

Figure 5.37. Streamwise Velocity Vectors
for Moving Endwall (Crenulated Blades)
t/c = 0.01, z = 0.7 in., $Re_c = 9.72 \times 10^4$

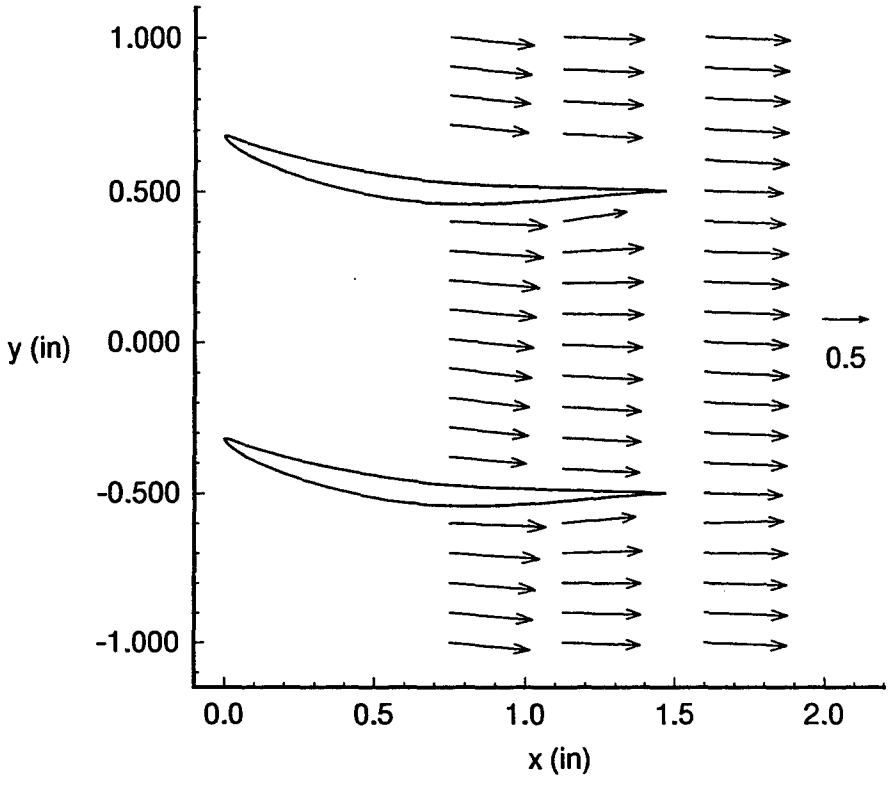

Figure 5.38. Streamwise Velocity Vectors for Moving Endwall
(Crenulated Blades)
$t/c = 0.01$, $z = 0.0$, $Re_c = 9.72 \times 10^4$

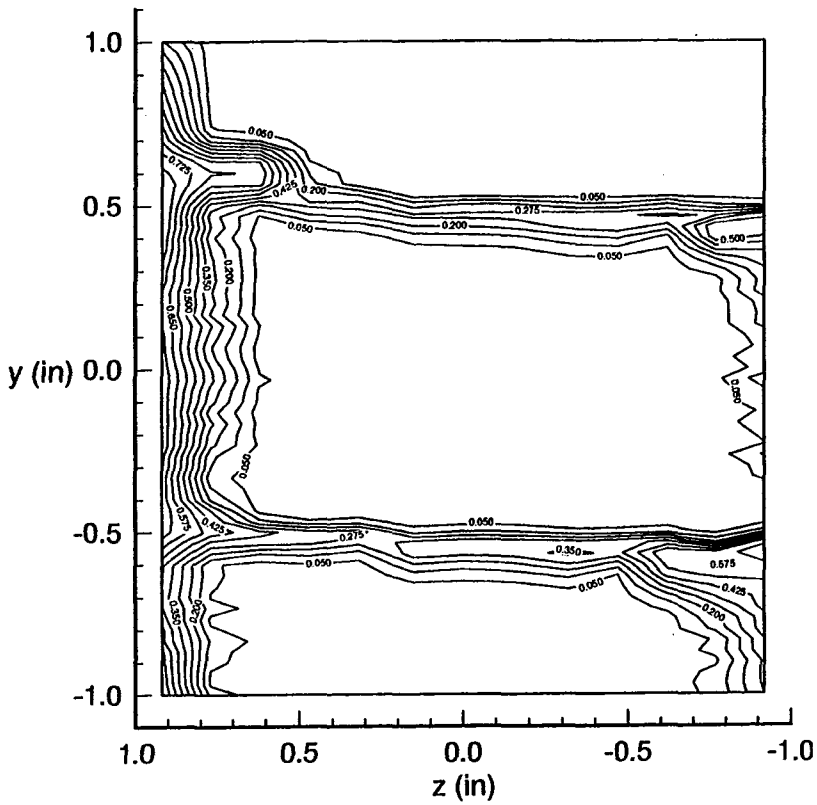

Figure 5.39. Total Pressure Loss Contours
for Moving Endwall
t/c = 0.02, ϖ contour interval 0.075

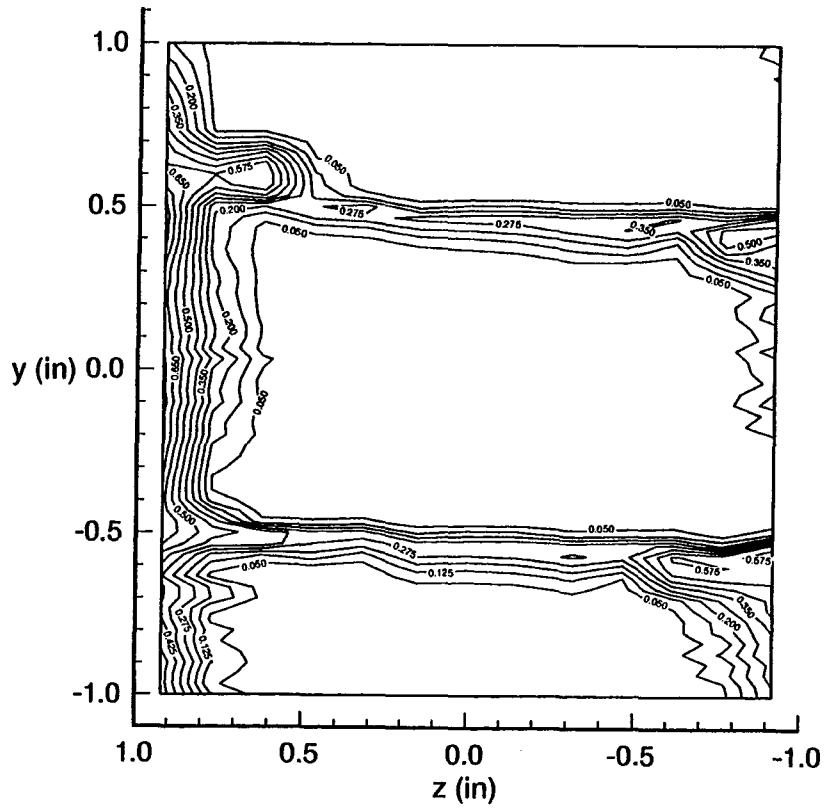

Figure 5.40. Total Pressure Loss Contours
for Moving Endwall
t/c = 0.01, ϖ contour interval 0.075

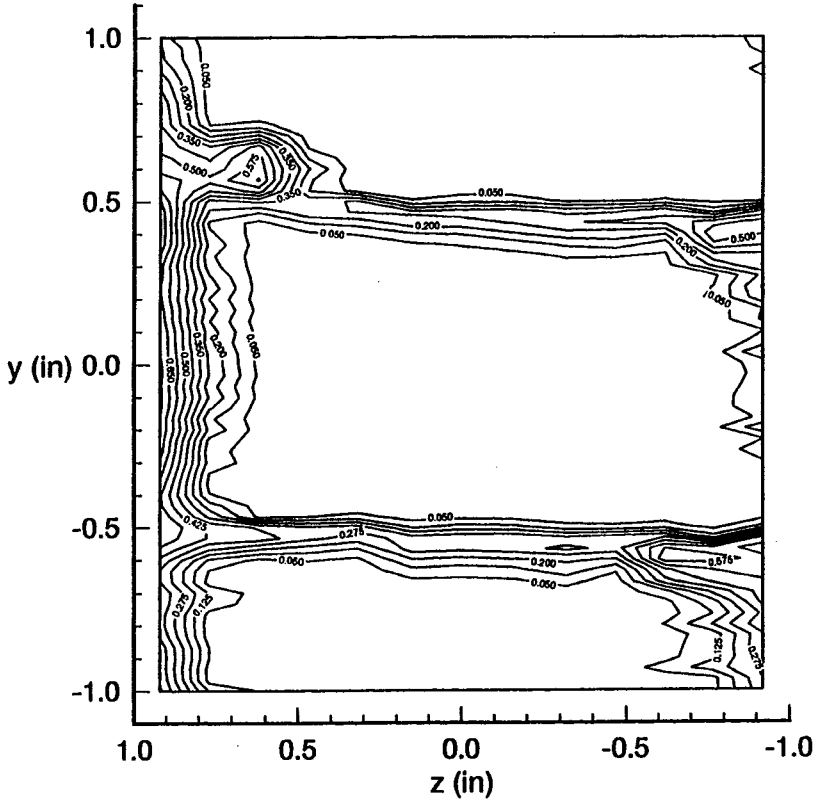

Figure 5.41. Total Pressure Loss Contours
for Moving Endwall
t/c = 0.005, ϖ contour interval 0.075

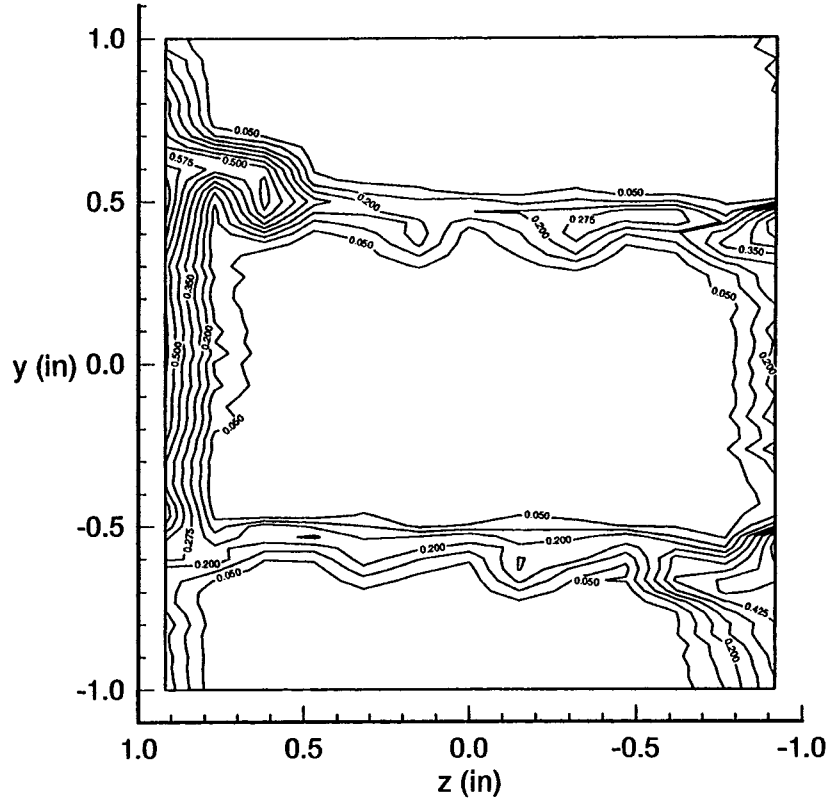

Figure 5.42. Total Pressure Loss Contours
for Moving Endwall (Crenulated Blades)
t/c = 0.01, ϖ contour interval 0.075

Appendix A. Software Listing

The AFIT Wind Tunnel Cascade Facility data acquisition software is written in MS QuickBasic 4.5 and consists of multimodule programs. The software is found on the Zenith Data systems Z433 D+ computer inside the laboratory instrumentation room in the directory C:\SHARK\CODE\SOURCE\MODS. The executable programs found in this directory are used by the computer to acquire or reduce the experimental data needed for a set of test runs. A brief description of each program is presented.

HHOTIRE.EXE: The program is used to calibrate hot-wire/film probes. This program contains subprograms for defining the hot-wire/film probe parameters, calibrating the PSI 8400, setting the variables for the IFA 100 and IFA 200, calibrating the cooling ratio, calibrating the temperature loading factor and checking the calibration of the probe.

WWKACQ.EXE: The program is used to take hot-wire/film probe measurements in the cascade flowfield. This program contains subprograms for calibrating the PSI 8400, setting the variables of the IFA 100 and IFA 200, operating the transverse control stepper motors, defining the sample area for data acquisition and acquiring velocity and flow angle data in the cascade. The subprogram "Get Sample" does not work.

WWKRED.EXE: The program is used to reduce the raw data acquired from hot-wire/film probes, thermocouples and static pressure wall taps. First, this program reduces the data acquired by WWKACQ.EXE. Then, it provides subprograms for calculating wake parameters and graphing different flow variables calculated in the reduction process of the program.

PPRKACQ.EXE: The program is used to take measurements with the total pressure rake. This program contains subprograms for calibrating the PSI 8400, operating the transverse control stepper motors, defining the sample area for data acquisition and acquiring the total pressure rake data. The subprogram "Get Sample" does not work.

PPRKRED.EXE: The program is used to reduce the raw data acquired from the total pressure rake, thermocouples and static pressure wall taps. First, the program reduces the raw data acquired by PPRKACQ.EXE. Then, it provides subprograms for calculating pressure loss parameters and graphing these loss parameters.

PPSCAN.EXE: The program is used to determine the freestream inlet total pressure and the static pressures at the inlet and exit to the blade cascade. From these values, the inlet velocity to the cascade is determined.

Appendix B. Hot-Wire/Film Calibration Procedures

The procedure used to calibrate a x-configuration hot-wire/film probe is presented in step by step form to provide an easy method for calibrations needed in the future.

- Select an x-configuration hot-wire or hot-film sensor to be calibrated.
- Measure the bisector and skew angles for the sensor. The following items are required for this process: straight edge, tape, overhead projector, engineering paper, pencil and protractor.
    - Turn the projector on and shine it on the wall.
    - Tape a piece of engineering paper to the wall in the center of the projection.
    - Tape the sensor to the projector such that the outline of the probe is projected onto the paper on the wall. The side of the probe that reads TSI should be facing up. Only two prongs should appear in the image on the paper.
    - Trace the sensor wires onto the paper with the use of the straight edge and pencil. The image of the sensor body should also be traced onto the paper.
    - Measure the angle between the wires within 0.5 degrees with the protractor. Half of this angle is the bisector angle (needed for the calibration).
    - Draw a line representing the bisector angle and a line representing the longitudinal axis of the sensor. The angle measured between these two lines is the skew angle (needed for the calibration). A positive skew angle is a counter-clockwise rotation from the probe axis line to the bisector line.

- Turn on the data acquisition equipment with the master switch on the cabinet.
- Setup the IFA 100 for acquisition of hot-wire/film voltages.
    - Connect the coaxial cables to the probe support on the TSI 1125 Probe Calibrator and the Probe Standard connector on the rear of the IFA 100. (Connect Channel 1 - Channel 1 and Channel 2 - Channel 2)
    - Set the BRIDGE SEL switch to STD 1.
    - Set the SENSOR switch to either wire or film.
    - Connect the short coaxial cable from the input to the IFA 200 to the output of the signal conditioner for each channel. The switches on the signal conditioner should be set to Int and DC.
- Find the resistance of the cables and probe support for each channel. Same procedure for both channels.
    - Put the shorting probe into the probe support on the calibrator.
    - Press the RES MEAS button on the front of the IFA 100. NULL DSPL will light up.
    - Null the digital reading on the front screen to equal zero by turning the OPERATE RES knob counter-clockwise.
    - Press the RES MEAS button again. The resistance displayed on the screen is the cable resistance for that channel. Press enter to record this cable resistance.
- Insert the hot-wire/film sensor into the probe support of the calibrator and set the operating resistance for each wire. The same procedure is used for each wire.

- Press the OPERATE RES button.
- Turn the OPERATE RES knob clockwise until the operating resistance on the screen represents the value given on the top of the sensor probe box.
- Set the BRIDGE COMP for each sensor channel.

- Calibrate the PSI 8400 unit.
  - Open up the air tank to provide at least 100 psig air.
  - Plug in the vacuum pump.
  - Enter "mcp84" from the keyboard in the directory C:\8400.
  - Type 1 and then the name of the file "shark.mac".
  - Press F1 to setup the printer.
  - Press F2 to initialize the PSI 8400 unit.
  - Press F3 to calibrate the PSI 8400 unit.
  - Press F9, 4, then y to exit.
- Start hot-wire/film calibration program by typing HHOTIRE.EXE in the directory C:\SHARK\CODE\SOURCE\MODS.
- Enter the data for the hot-wire/film found on its box. The cable resistance for each wire, bisector angle and skew angle have already been determined.
  - Enter 10 for RBupper.
  - Enter 0.843 for the RecovFac.
  - Calculate RTRatio by dividing R100 - R0 listed on the box by 100.
- Set the variables for the IFA 100 and IFA 200.

- Set the filter to 5 kHz.
- Set the gain to 3.0 and the offset to 2 by specifying the lowest expected voltage is 1 and the highest is 4.
- Accept the cable resistance.

- Turn the air on and adjust the cable compensation.
- Determine the cooling ratio in the "Calibrate Cooling Ratio" subprogram.
    - Get new velocity data. The velocity calibration will be an eleven point unidirectional calibration from 20 to 70 m/s.
        - Lower the probe to within 0.05 in. of the nozzle of the calibrator and center the probe over the nozzle. The angle of the probe to the horizon should be set at zero. A digital protractor provided by the technicians will help determine an accurate angle measurement.
        - Turn the knob on the pressure calibrator to set the velocity.
        - Type "d" and enter to acquire the hot-wire/film voltages for each point.
        - Save the file in a separate directory as a backup.
    - Get new angle data. The angle calibration will be an eleven point straight calibration from -10 to 10 degrees.
        - Set the velocity as a constant and vary the angle of the probe stand. The digital protractor will help determine the angle.
        - Type "d" again to acquire hot-wire/film voltages.
        - Save the file in a separate directory as a backup.

- Calculate the value of the cooling ratio manually.
    - Start with 0.1 for each channel and increment by .1 until the cooling ratio that provides the smallest sum squared error is bracketed within a range of 0.2.
    - Continue to bisect the range of possible values of k until the cooling ratio is found (0.XXX).
    - Save both channels.
- Determine the constants A, B and C and the temperature loading factor in "Calibrate Hot-wire" subprogram.
    - Turn the heater unit on and set to 7.5 Amps.
    - Get new hot-wire data. The temperature calibration will be an eleven point unidirectional calibration from 20 to 70 m/s.
        - Take the first 6 measurements, then increase the velocity through the calibrator to 120 m/s. Allow the flow to run at this velocity until the bottom total temperature of the calibrator has risen approximately 2°C.
        - Take the last 5 measurements.
        - Save the file in a separate directory as a backup.
        - Turn heater off.
    - Calculate the temperature loading factor and constants of calibration.
        - Use the range calculator to determine the temperature loading factor ($\pm$0.XXX).

    - Save the values of both channels.

- Check the calibration for the hot-wire/film in the subprogram "Check Calibration".
    - Set the angle and velocity of the flow and compare the value measured by the probe to the known value.

Appendix C. Procedure for Acquisition of Velocities and Flow Angles

Hot-wire/film probe sensors were used in this experimental study to measure the velocities and flow angles of the cascade flowfield. In order to represent the flowfield of the cascade accurately, data collection grids for each y-z data plane had to be specified. After the data collection grids were established, the hot-wire/film data acquisition procedure was used to determine the flowfield characteristics of the cascade with varying tip clearances.

Grids for Data Acquisition. The fine grid spacing in the tip region for the stationary wall cases was chosen as 0.02 in. (0.0508 cm), and the coarse grid spacing was chosen as 0.1 in. (0.254 cm). Figure C.1 shows the data acquisition grid in the wake region (x/c = 1.0667) for the stationary flat wall case; Figure C.2 shows the data collection grid at the midchord of the cascade; and C.3 shows the data grid points for the upstream plane at x/c = -0.0667. For each of these grids, the fine grid spacing accounts for 82.8% of the number of points but only 16.7% of the area.

The fine and coarse grid spacings for the moving endwall test cases remained the same as those for the stationary cases. Figures C.4 to C.8 show the data collection grids for the moving endwall y-z test planes at x/c = 1.0667, 0.75, 0.5, 0.25 and -0.0667, respectively. Each one of these grids has a fine spacing near the root wall and moving endwall to accurately determine the flow structure at these locations with changing tip clearances.

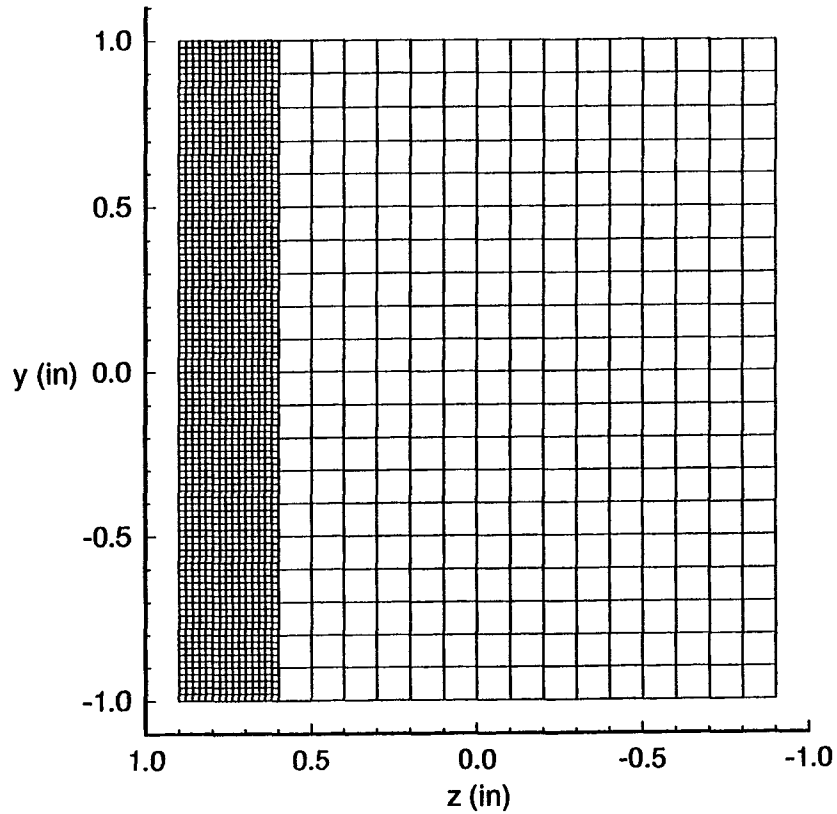

Figure C.1. Transverse Velocity Vector Grid
for Stationary Endwall
x/c = 1.0667

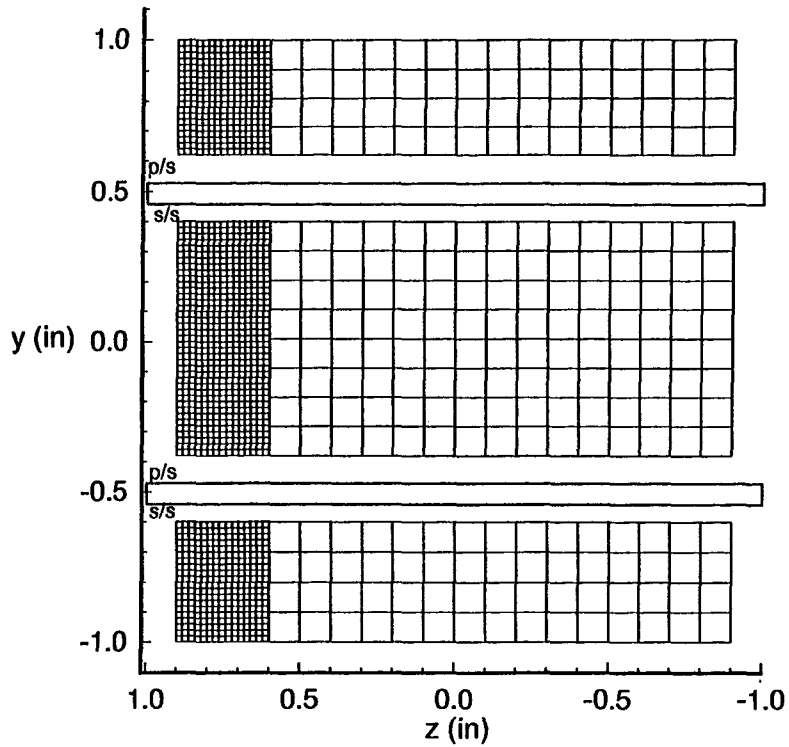

Figure C.2. Transverse Velocity Vector Grid
for Stationary Endwall
x/c = 0.5

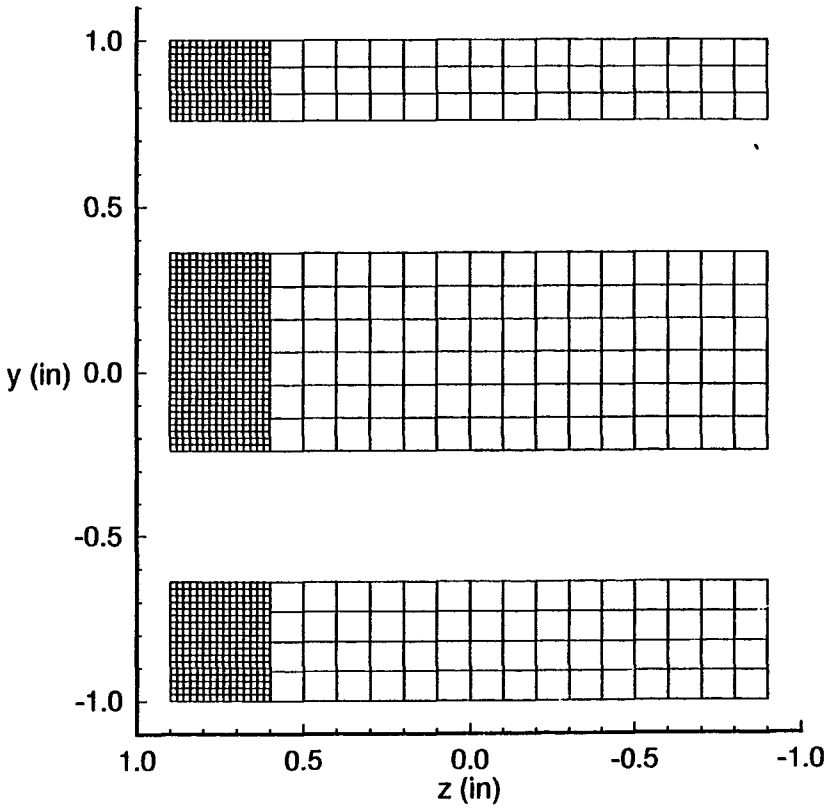

Figure C.3. Transverse Velocity Vector Grid
for Stationary Endwall
x/c = -0.0667

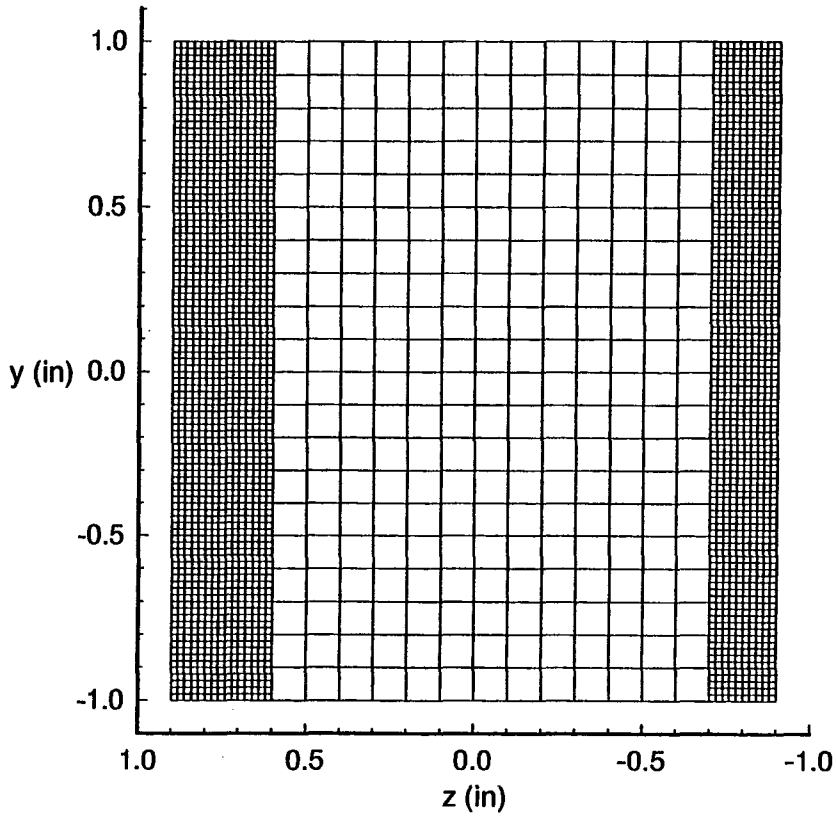

Figure C.4. Transverse Velocity Vector Grid
for Moving Endwall
x/c = 1.0667

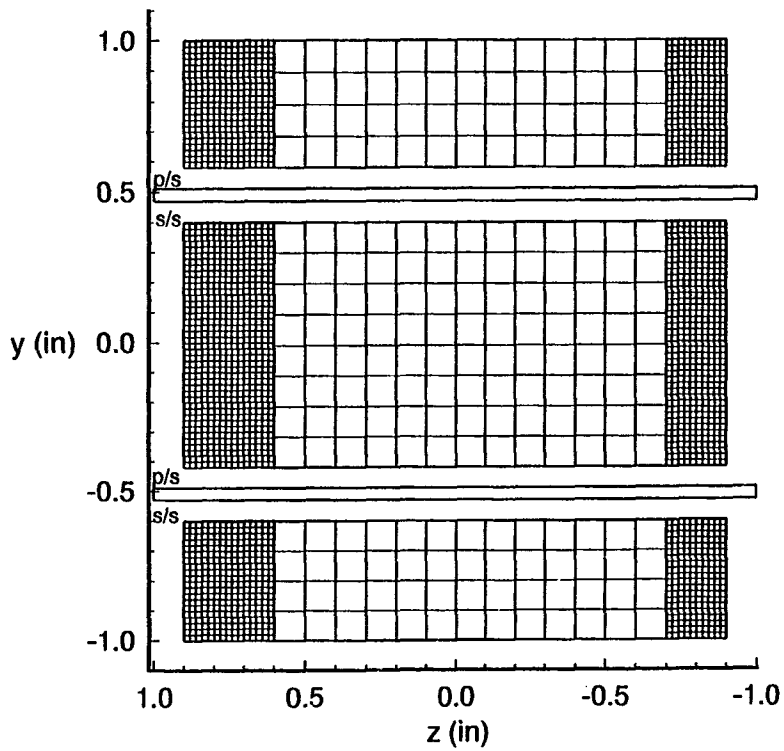

Figure C.5. Transverse Velocity Vector Grid
for Moving Endwall
x/c = 0.75

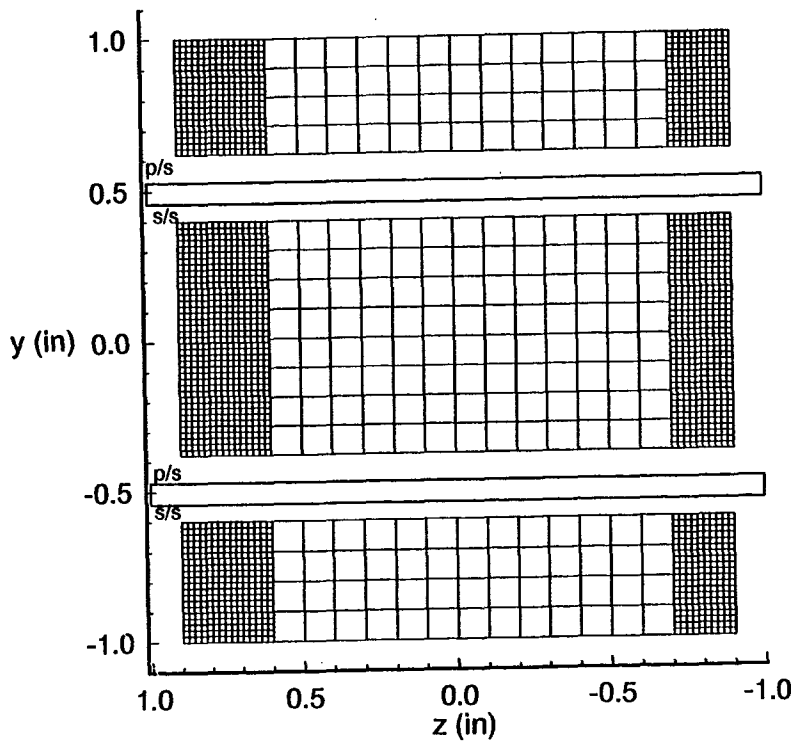

Figure C.6. Transverse Velocity Vector Grid
for Moving Endwall
x/c = 0.5

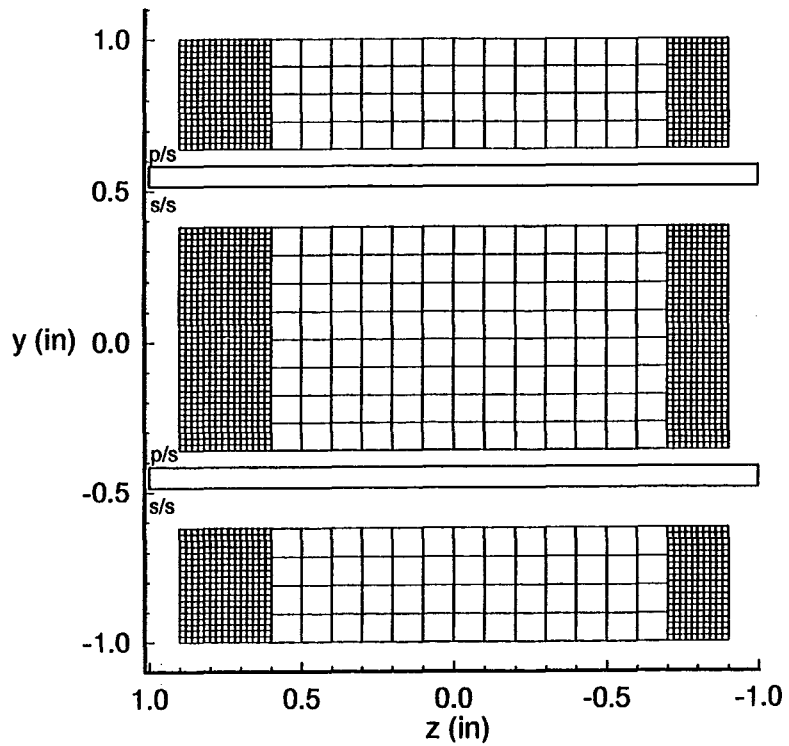

Figure C.7. Transverse Velocity Vector Grid
for Moving Endwall
x/c = 0.25

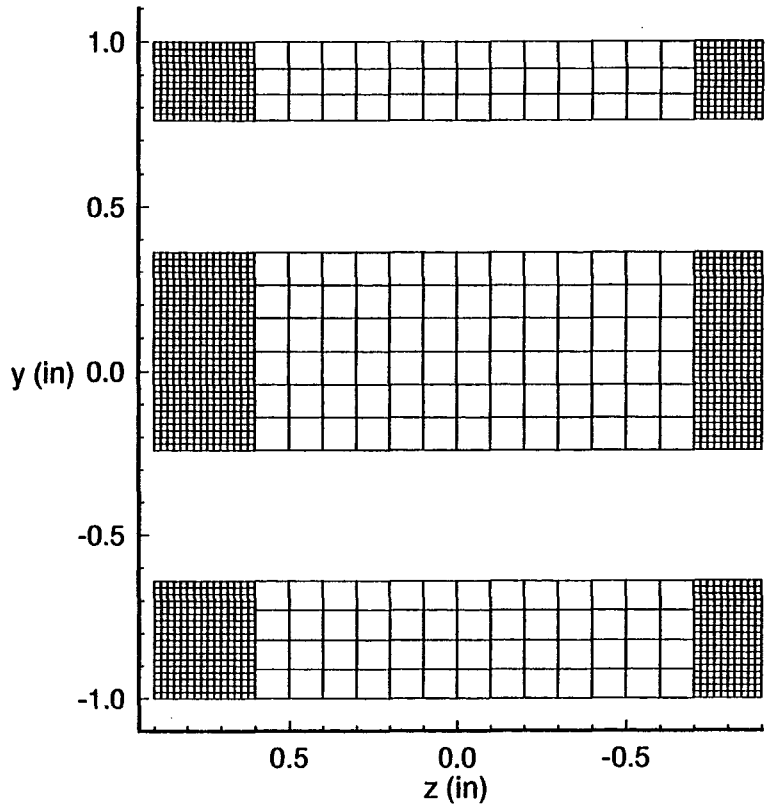

Figure C.8. Transverse Velocity Vector Grid
for Moving Endwall
x/c = -0.0667

Hot-Wire/Film Data Acquisition. A detailed procedure for the acquisition of velocities and flow angles using hot-wire anemometry is presented in step by step form.

- Warm up the tunnel and the rotor for approximately 1-1/2 hours to allow temperatures to steady.
- Find the resistance of the cables and probe support for each channel. Same procedure for both channels.
    - Put the shorting probe into the tunnel probe support.
    - Press the RES MEAS button on the front of the IFA 100. NULL DSPL will light up.
    - Null the digital reading on the front screen to equal zero by turning the OPERATE RES knob counter-clockwise.
    - Press the RES MEAS button again. The resistance displayed on the screen is the cable resistance for that channel. Press enter to record this cable resistance.
- Insert the hot-wire/film sensor into the tunnel probe support and set the operating resistance for each wire. The same procedure is used for each wire.
    - Press the OPERATE RES button.
    - Turn the OPERATE RES knob clockwise until the operating resistance on the screen represents the value given on the top of the sensor probe box.
    - Set the BRIDGE COMP for each sensor channel.

    - Set the cable compensation for each channel.

- Calibrate the PSI 8400 unit.
    - Open up the air tank to provide at least 100 psig air.
    - Plug in the vacuum pump.
    - Enter "mcp84" from the keyboard in the directory C:\8400.
    - Type 1 and then the name of the file "shark.mac".
    - Press F1 to setup the printer.
    - Press F2 to initialize the PSI 8400 unit.
    - Press F3 to calibrate the PSI 8400 unit.
    - Press F9, 4, then y to exit.
- Start hot-wire/film data acquisition program by typing WWKACQ.EXE in the directory C:\SHARK\CODE\SOURCE\MODS.
- Set the variables for the IFA 100 and IFA 200.
    - Set the filter to 5 kHz.
    - Set the gain to 3.0 and the offset to 2 by specifying the lowest expected voltage is 1 and the highest is 4.
    - Accept the cable resistance.
- Check the warm up temperatures of the tank and the rotor and allow each to reach a steady state value before preceding.
- Turn off the tunnel and the rotor to check the blade tip clearance.
    - Use feeler gauges to set the gap size.

    - Move the rotor headstock with the transverse mechanism on the rotor support stand.
- Turn the tunnel and rotor back on.
- Enter the "Get Data" subprogram.
    - Type -1.56 for the incidence angle.
    - Type 0.1 for the x location.
    - Enter a test run description.
    - Accept or change the file numbering system.
- Define the limits and spacing of the data points for a particular test.
- Position the probe in all three directions for the test location.
- Acquire the data.

Appendix D. Equipment Listing

Subsystem	Model Number/Description
Pressure Measurement	Pressure Systems Inc. Model 8400 Pressure Scanner (20 kHz maximum sample rate) Model 8415 Scanner Interface Unit Model 8420 Scanner Digitizer Unit Model 8440 Analog Input Unit Model 8433 Pressure Calibration Unit (1 psid) Model 8433 Pressure Calibration Unit (5 psid) Certified Standard Transducer (0.2-18 psi range, 0.00001 psi accuracy)
	Transducer block P/N 32RG-0301 (1 psid range, 0.0005 psi accuracy)
	Transducer block P/N 3201B (1 psid range, 0.0005 psi accuracy)
	Transducer block P/N 3205B (5 psid range, 0.0005 psi accuracy)
	Pressure Rake (5 ports spaced 0.381 cm) (0.158 cm OD, 0.1016 cm ID)
	CEC Model 2500 Digital Barometer (13.00 - 15.51 psia range, 0.005 psi accuracy)
Velocity and Temperature Measurement	TSI Model IFA 100 System Intelligent Flow Analyzer Model 140 Temperature Module Model 150 Anemometer Modules (2) Model 157 Signal Conditioner Modules (3)
	TSI Model IFA 200 System Multichannel Digitizer Model 252 Digitizers (3) (50 kHz maximum sample rate, 5 V range, 0.002 V accuracy)

	TSI Model 1241-10 X-Film Sensor
	TSI Model 1241-20 X-Film Sensor
	TSI Model 1241-T1.5 X-Wire Sensor
	TSI Model 1155-36 Probe Support
	TSI Model 1125 Probe Calibrator
	Omega T-type Thermocouple (copper-constantan, 0.3°C accuracy)
Temperature Measurement	Hewlett-Packard Model 3455A Digital Voltmeter (0.00002 V accuracy, 24 Hz maximum sample rate)
	Hewlett-Packard Model 3495A Scanner
	Omega T-type Thermocouples (2) (copper-constantan, 0.3°C accuracy)
Transverse Control	New England Affiliated Technologies Model 310 Programmable Motion Controllers (2)
	Oriental Motor Company Stepper Motors (2) (400 steps/revolution resolution)
Central Computer	Zenith Model Z433 D+ (80486 DX 33 processor) National Instruments Model GPIB-PCII General Purpose Interface Board TSI Model 6260 Parallel Interface Board
	Software (developed by AFIT/ENY, written in MS QuickBasic 4.5)
Rotor System	Baldor CDP-3450 Motor (1 HP DC permanent magnet, 2500 rpm)
	KB Electronics DC Controller KBPC-240D

Vita

Captain Richard Jeffrey McMullan [redacted], [redacted]. He graduated from Habersham Central High School, Cornelia, Georgia in 1987. In 1991, he earned a Bachelor of Science in Mechanical Engineering from Clemson University and was commissioned a Second Lieutenant in the United States Air Force.

His initial active duty assignment was at the Armament Directorate of Wright Laboratory, Eglin AFB, FL where he managed the day-to-day operations of a unique $15 million Air Force facility tasked with development of new explosive formulations. Captain McMullan was assigned to the Air Force Institute of Technology, Wright-Patterson AFB, OH in 1995 to pursue a Master of Science in Aeronautical Engineering.

[redacted]

REPORT DOCUMENTATION PAGE

Form Approved
OMB No. 0704-0188

1. AGENCY USE ONLY *(Leave blank)*	2. REPORT DATE	3. REPORT TYPE AND DATES COVERED
	December 1996	Final Master's Thesis

4. TITLE AND SUBTITLE
Influence of Tip Clearance on the Flowfield in a Compressor Cascade with a Moving Endwall

5. FUNDING NUMBERS

6. AUTHOR(S)
Richard J. McMullan

7. PERFORMING ORGANIZATION NAME(S) AND ADDRESS(ES)
Air Force Institute of Technology
WPAFB, OH 45433-6583

8. PERFORMING ORGANIZATION REPORT NUMBER
AFIT/GAE/ENY/96D-5

9. SPONSORING/MONITORING AGENCY NAME(S) AND ADDRESS(ES)
Dr. W. Copenhaver WL/POTF

10. SPONSORING/MONITORING AGENCY REPORT NUMBER

11. SUPPLEMENTARY NOTES

12a. DISTRIBUTION/AVAILABILITY STATEMENT
Approved for public release; distribution unlimited

12b. DISTRIBUTION CODE
A

13. ABSTRACT *(Maximum 200 words)*

The effects of changing the blade tip clearances on the velocity and pressure flowfields within a compressor cascade were investigated in this experimental thesis. All moving endwall measurements were taken at a constant flow coefficient of 0.5 and tip clearances of 0.5, 1.0 and 2.0 percent chord. Hot-wire/film probes were used to determine the three-dimensional velocity vector components in various transverse planes - one upstream of the leading edges of the blades, three within the blade cascade and one downstream of the trailing edges of the blades. The transverse velocity vector plots showed a scraping of the tip leakage vortex from the suction surface of one blade across the blade pitch to the pressure surface of the adjacent blade. A total pressure rake placed downstream of the trailing edges of the blades measured the pressure flowfield at the exit of the cascade. The mass-averaged values of total pressure loss coefficient decreased for reduced gaps. Finally, the tests performed on a crenulated blade geometry at a tip clearance of 0.01 chord showed a 15.5% reduction in the total pressure losses as compared to the straight blade geometry.

14. SUBJECT TERMS
axial flow compressor blades, cascades, compressor losses, tip clearance, tip leakage vortex, velocity vectors, vortices

15. NUMBER OF PAGES
137

16. PRICE CODE

17. SECURITY CLASSIFICATION OF REPORT	18. SECURITY CLASSIFICATION OF THIS PAGE	19. SECURITY CLASSIFICATION OF ABSTRACT	20. LIMITATION OF ABSTRACT
Unclassified	Unclassified	Unclassified	UL